University of Alberta

LEGACY SEISMIC INVESTIGATIONS OF KARST SURFACES: IMPLICATIONS FOR HEAVY OIL EXTRACTION FROM THE DEVONIAN GROSMONT FORMATION, NORTHEASTERN ALBERTA, CANADA

by

TODD DYLAN BOWN

A thesis submitted to the Faculty of Graduate Studies and Research in partial fulfillment of the requirements for the degree of

MASTER OF SCIENCE

DEPARTMENT OF PHYSICS

Summer 2011
Edmonton, Alberta

Examining Committee

Dr. Douglas R. Schmitt, Department of Physics

Dr. Richard D. Sydora, Department of Physics

Dr. Clayton V. Deutsch, Department of Civil & Environmental Engineering

Dr. Nicholas B. Harris, Department of Earth & Atmospheric Sciences

Abstract

The Devonian Grosmont Formation in northeastern Alberta, Canada is the world's largest accumulation of heavy oil in carbonate rock with estimated bitumen in place of 64.5×10^9 m^3. At the studies location the eroded and buried surface of the Grosmont, referred here as the SubMannville uncoformity (SMU), was analyzed and interpret for a karsted surface. Results from legacy seismic data and available well log information were able to define the SMU as a mature karst surface within observable features such as dolines, karst valleys, karst plain and poljie and a ridge. The large scale topography of the ridge and poljie were geologically controlled by the underlying the Paleozoic rocks. Furthermore, the poljie was observed to contain the majority of the dolines in the area, noted to occur elsewhere. That said, dolines and karst valleys and other such dissolution features have the potential to erode the bitumen reservoir of the upper Grosmont members C and D. It is important for future oil prospectors to map and avoid areas such as the poljie, dolines and karst valley to increase certainty of reservoir presence.

A preliminary rock-physics model was developed for the Grosmont reservoir of a bitumen-saturated dolomite. Results suggest that elastic properties of the Grosmont reservoir are temperature-frequency dispersive. This implies that there is a potential to use time-lapse seismic to map and monitor heating of the reservoir.

ACKNOWLEDGEMENTS

This thesis was financially supported by funds from Carbonate Research Program of Alberta Innovates - Technology Futures (AITF) and Dr. Doug R. Schmitt had been supplemented by NSERC funding.

This project synthesizes the work and advice of many individuals. Many thanks goes out to supervisor Dr. Doug Schmitt for his on-going advice, guidance, wisdom, collaboration, and editorial work that greatly improved the final version of this thesis. Postdoctoral research Dr. Ali Oncel assisted in the organizing the raw regional data and the processing of the regional seismic lines. Postdoctoral researcher Dr. Gautier Njiekak who assisted in the collection of well log information and graciously facilitated other members of the group. Ph.D. student Elahe Poureslami, summer student Mr. Gordon. Course Based M.Sc. student Mr. Mohamed Fatmed for his work of interpreting formation tops from well logs over the region of the project and placing them into a Petrel project. M.Sc. graduate Mr. Femi Ogunsuyi for his exceptional help with Petrel software and the interpretation of the regional dataset. The work over the project site would have not been possible without the help Stephen Kotkas (Sigma Exploration) and Cathal Tunney (AIFT) for their dedicated assistance in overcoming proprietary hurdles associated with obtaining the legacy seismic data. I would also like to personally thank the members of the Carbonate Research Program, Alberta Innovates - Technology Futures of Dr. Ron Sawatzky, Dr. Jose Alvarez and their team, and the subsidiary members of the program here at the University of Alberta of Dr. Brian Jones, and Dr. Clayton Deutsch for their on going feedback and comments throughout this project. Special thanks to Dr. Ron Sawatzky and Cathal Tunney for their reviews and discussion on the working confidentiality agreement between AIFT and this thesis. I am also grateful for the occasional discussions with David Bonar, Grey Riddle, Helen Yam, Sean Contenti, Len Tober, Jamie Ostrikoff and many more for providing helpful insights and ideas.

My sincere gratitude goes out to my parents Barry and Diana for their upmost moral as well as monetary support and dinner visits to the city. My brothers Chad and Travis, to them I owe my courage, honour and virtue. Last but not least, I give my warmest thanks to my girlfriend Danielle for her love, compassion, great food, fresh

change of clothes and many rides home from the university this past summer when the clouds poured rain.

Geographic base maps over Alberta are provided free of charge via a collaboration of the Geological Survey of Alberta and AltaLIS Ltd (see http://www.altalis.com/prod_base_small.html). These data were provided in the Alberta based 10TM system and were converted to geographical latitude-longitude (WGS 84) using Didger™ (Golden Software, Colorado). The seismic data processing software VISTA™ was donated for our use by GEDCO Ltd, Calgary. The seismic interpretation package PETREL™ was donated for use by Schlumberger, Canada. The forward seismic modeling software package Tesseral2D™ was donated for use by Tesseral Technologies Inc, Calgary.

Table of Contents

Chapter 1 Introduction 1
1.1. Introduction 1
Chapter 2 Literature Review 4
2.1. Overview 4
2.2. Geological Background 5
2.3. Karst Geomorphology 15
2.4. Carbonate and Karst Geophysical Studies 22
2.5. Summary 28
Chapter 3 The Vintage Seismic Surveys and Well Log Data 29
3.1. Overview 29
3.2. Regional Seismic Surveys 31
3.2.1. Survey Series A - January 1984 31
3.3. High-Resolution Seismic Surveys 31
3.3.1. Survey Series B - March 1981 33
3.3.2. Survey Series C - February 1984 34
3.3.3. Survey Series D - March 1985 37
3.3.4. Survey Series E - February 1986 40
3.4. Well Log Data 41
3.5. Summary 43
Chapter 4 Seismic Processing 44
4.1. Overview 44
4.2. Pre-Processing 45
4.2.1. Demultiplexing and Reformatting 45
4.2.2. File Edits 46
4.2.3. Merging of Field Geometry 47
4.2.4. Trace Edits 49
4.3. Initial Harmonic Analysis 52
4.3.1. Frequency Bandwidth Analysis 52
4.3.2. Signal to Noise Ratio Analysis 57
4.3.3. Amplitude Spectrum Analysis 58
4.4. Amplitude Recovery 59
4.4.1. Exponential Gain 59
4.4.2. Surface-Consistent Scaling 61
4.5. Static Corrections 62
4.5.1. Elevation Statics 62
4.5.2. Refraction Statics 63
4.6. Ground Roll Suppression 65
4.7. Frequency Filter and Top Mute 68
4.8. Deconvolution 69
4.9. Spectral Whitening 71
4.10. CMP Sorting 71
4.11. Velocity Analysis 72
4.12. Residual Statics 74

4.13. Trim statics 76
4.14. NMO Correction 76
4.15. CMP Stacking 79
4.16. Migration 80
4.16.1. Finite Difference Migration - Post-Stack 80
4.16.2. Kirchhoff Migration - Pre-Stack 81
4.17. Post-Stack Clean-up 82
4.17.1. White Noise Suppression 82
4.17.2. Frequency Filter and Scale 84
4.18. Summary 84
Chapter 5 Forward Seismic Modelling of Karst Features 86
5.1. Overview 86
5.2. Two-Layer Model 86
5.3. Forward Seismic Modelling 88
5.4. Results 90
5.5. Fresnel Zone and Implication of Migration 93
5.6. Discussion 94
5.7. Summary 97
Chapter 6 Rock-physics Modelling of the Grosmont Reservoir 98
6.1. Overview 98
6.2. Previous Work 98
6.3. Method 100
6.4. Results 102
6.5. Discussion 104
6.6. Summary 105
Chapter 7 Interpretation 106
7.1. Overview 106
7.2. Regional Interpretation 106
7.3. Local Interpretation 111
7.4. Discussion of Grosmont 122
7.5. Summary 123
Chapter 8 Conclusion 125
8.1. Conclusion 125
8.2. Future Work 126

List of Tables

TABLE 2.1: GEOPHYSICAL METHODS. 23
TABLE 2.2: PHYSICAL PROPERTIES OF CARBONATE AND ASSOCIATED MINERALS. 24
TABLE 3.1: ACQUISITION PARAMETERS DEPLOYED BY THE VINTAGE SEISMIC SURVEYS. 30
TABLE 4.1: A SERIES OF NARROW BAND-PASS FILTERS. 53
TABLE 4.2: ESTIMATED FREQUENCY RANGE OF LATERALLY CONTINUOUS REFLECTION EVENTS ACROSS THE ZONE OF INTEREST IN SHOT RECORDS FOR EACH OF THE SEISMIC SURVEYS. 56
TABLE 4.3: SUMMARY OF GROUND ROLL CONTAMINATION IN SHOT RECORDS. 56
TABLE 4.4: ESTIMATED DOMINANT FREQUENCY AND BANDWIDTH OF RECORDED SEISMIC ENERGY. 58
TABLE 4.5: LIST OF INITIAL BAND-PASS FILTERS APPLIED TO THE SEISMIC DATA. 68
TABLE 7.1: SUMMARY OF THE VELOCITY MODEL USED TO CONVERT TWO-WAY TIMES TO ELEVATIONS. 113

List of Figures

FIGURE 1.1: ALBERTA MAP SHOWING THE EXTENT OF THE GROSMONT PLATFORM [MODIFIED FROM *BUSCHKUEHLE ET AL.*, 2007] AND CARBONATE BITUMEN DEPOSITS OF THE NISKU AND GROSMONT [*ERCB*, 2009A]. 2
FIGURE 1.2: SATELLITE IMAGE OF THE BAHAMA BANKS ILLUSTRATING THE SIZE OF A MODERN DAY SHALLOW WATER CARBONATE PLATFORM. CONCEPT AFTER HARRISON [1984]. 2
FIGURE 2.1: PALEOGEOGRAPHIC RECONSTRUCTION MAP OF NORTH AMERICA DURING THE LATE DEVONIAN ERA (360 MA) COURTESY OF DR. RON BLAKEY [2011] WITH PRESENT-DAY GROSMONT PLATFORM OUTLINED IN RED. 5
FIGURE 2.2: GENERALIZED STRATIGRAPHY FOR THE STUDY AREA CONSTRUCTED AND MODIFIED FROM ERCB [2009B]. HIGHLIGHTED IS THE SUBMANNVILLE UNCONFORMITY (SMU) AND PRECAMBRAIN UNCONFORMITY (PCU)..... 7
FIGURE 2.3: BEDROCK MAP OF ALBERTA MODIFIED FROM MOSSOP AND SHETSEN [1994] WITH GROSMONT PLATFROM OUTLINED IN WHITE. LINE A-A' SHOW THE LOCATION OF THE CROSS-SECTION FOR FIGURE 2.4(A). 8
FIGURE 2.4: (A) A SYNOPTIC CROSS-SECTION OF A-A' FROM FIGURE 2.3 SHOWING THE GENERAL GEOLOGY STRUCTURE THROUGH THE AREA. DEVELOPED FROM MOSSOP AND SHETSEN [1994]. (B) CROSS-SECTION OF THE GROSS GEOLOGICAL STRUCTURE IN THE STUDY AREA [MODIFIED FORM *BORRERO-GOMEZ*, 2010]..... 9
FIGURE 2.5: REPRESENTATIVE NATURAL GAMMA RAY LOG DELINIATION OF THE GROSMONT [MODIFIED FROM *R S HARRISON*, 1986]. 11
FIGURE 2.6: AREAL EXTENT OF THE TOPMOST HONDO EVAPORITE BASIN [MODIFIED FROM *SWITZER ET AL.*, 1994]. 11
FIGURE 2.7: PROPOSED DEVELOPMENT OF THE GROSMONT PLATFROM (A) AREAL VIEW AND (B) PROFILE VIEW OF Q-Q' [MODIFIED FROM *SWITZER ET AL.*, 1994]..... 13
FIGURE 2.8: SCHEMATIC CROSS-SECTION SHOWING FEATURES AND FLUID FLOWS WITHIN AN ACTIVE KARST SYSTEM [REPRODUCED FROM *FORD AND WILLIAMS*, 2007]. 15
FIGURE 2.9: AIR PHOTOS OF DOLINES IN (A) KARST TERRAIN NEAR LEWISBURG, WEST VIRGINIA, U.S. (COURTESY OF WILLIAM K. JONES AND VIRGINIA SPELEOLOGICAL SURVEY) AND (B) PERMIAN LIMESTONE NEAR THE LITTLE COLORADO RIVER SOUTHEAST OF WINSLOW, ARIZONA, U.S. (COURTESY OF LOUIS J. MAHER, JR.)..... 17
FIGURE 2.10: TYPES OF DOLINES (A) COLLAPSE, (B) SOLUTION, (C) SUBSIDENCE, (D) SUBJACENT AND (E) ALLUVIAL STREAM SINK [REPRODUCED FROM *JENNINGS*, 1985].. 17
FIGURE 2.11: PHOTOGRAPH OF MEDICINE LAKE IN JASPER NATIONAL PARK..... 18
FIGURE 2.12: TWO AIR PHOTOS OF A DRY VALLEY NEAR NAHANNI NATIONAL PARK, NWT (COURTESY OF DR. PAUL SANBORN). DOLINES ARE ALSO VISIBLE IN (B)..... 19
FIGURE 2.13: CUTAWAY LIMESTONE FACE IN A CONSTRUCTION AREA IN SICILY EXHIBITING A BURIED SINKHOLE ON THE LEFT AND DISSOLUTION FISSURES ON THE RIGHT [REPRODUCED FROM *WALTHAM AND FOOKES*, 2003]. PERSON IS SHOWN ON BOTTOM LEFT CORNER FOR SCALE..... 19
FIGURE 2.14: CLASSIFICATION OF KARST SURFACES (ROCKHEADS) FOR CIVIL ENGINEERING PURPOSES OF (A) JUVENILE KARST, (B) YOUTHFUL KARST, (C) MATURE KARST, (D)

COMPLEX KARST AND (E) EXTREME KARST [MODIFIED FROM *WALTHAM AND FOOKES*, 2003]. 21
FIGURE 2.15: MAPPING OF SUBSIDENCE ZONE AT A DEPTH OF 300 METERS NEAR INTERSTATE I-70 [MODIFIED FROM *STEEPLES ET AL.*, 1986]. 25
FIGURE 2.16: TIME STRUCTURE MAP AT THE TOP EVAPORITES HORIZON DISPLAYING CICULAR DEPRESSIONS INTERPRETED AS SINKHOLES [REPRODUCED FROM *RAFAELSEN ET AL.*, 2008]. 26
FIGURE 2.17: RESULT OF AN ANALYSIS OF A 3D SEISMIC DATA OVER LATE PALEOZOIC CARBONATES IN THE EASTERN FINNMARK PLATFORM IN THE BARNET SEA. THE CUTAWAY VIEWS OF THE 3D SEISMIC DATA VOLUME AT THE TOP OF THE FIGURE DISPLAY THE DATA USING DIFFERENT ATTRIBUTES OF SEISMIC AMPLITUDE, DIP ATTRIBUTE, AND SPECTRAL DECOMPOSITION OF THE BASE OF THE ARTINSKIAN HORIZON. THE LARGER IMAGE IS THE RESULT OF A NEURAL NETWORK ANALYSIS THAT COMBINED THE ABOVE ATTRIBUTES TO ARRIVE AT A MAP ON NON KARSTED (WHITE-YELLOW) AND KARSTED (RED) ZONES [REPRODUCED FROM *COLPAERT ET AL.*, 2007]. 27
FIGURE 3.1: MAP SHOWING THE LOCATIONS OF THE SEISMIC DATA OBTAINED FOR THIS PROJECT WHERE (A) IS THE REGIONAL MAP OF ALL THE SEISMIC DATA AND (B) THE LOCAL AREA MAP HIGHLIGHTING SERIES B, C, D AND E DATA SETS. THE YELLOW DOT IN (B) DENOTES THE LOCATION OF A WELL WITH VSP DATA. 32
FIGURE 3.2: A PORTION OF SEISMIC SECTION FROM SURVEY B WHERE THE HIGHLIGHTED MAGENTA AREA WAS INTERPRETED AS THE WAVEFORM ARRIVAL OF THE SMU WITH A NOTED DIFFRACTION BENEATH THE UNCONFORMITY [MODIFIED FROM *G. CARRINGTON*, 1986B]. 34
FIGURE 3.3: A PORTION OF SEISMIC SECTION FROM SURVEY B WHERE THE HIGLIGHTED AREA IN MAGENTA IS THE INTERPRETED WAVEFORM ARRIVAL OF THE SUM [MODIFIED FROM *G. CARRINGTON*, 1986B]. 35
FIGURE 3.4: 'LOCATION EVALUTAION MAP' CREATED BY TESANOVIC [1984] AND A PORTION OF THE ORIGINALLY PROCESSED SEISMIC DATA WHERE YELLOW AND RED REGIONS HIGHLIGHT THE SMU AND MATCH THE COLOR CODING ON THE LOCATION EVALUATION MAP. 36
FIGURE 3.5: MAP OF TWO-WAY SEISMIC REFLECTION TIME TO THE SMU [MODIFIED FROM *TESANOVIC*, 1984]. 37
FIGURE 3.6: A PORTION OF AN ARBITRARY SEISMIC SECTION WITHIN THE 3D SURVEY OF SURVEY SERIES D WHERE THE HIGHLIGHTED AREA IN MAGENTA WAS THE INTERPRETED WAVEFORM ARRIVAL OF THE SMU [MODIFIED FROM *MCGILLIVRAY ET AL.*, 1987]. 38
FIGURE 3.7: MAP OF SMU PALEOSTRUCTURE SUPERIMPOSED ON THE TIME STRUCTURE OF THE UNCONFORMITY [MODIFIED FROM *HOWELL*, 1987]. THE BLACK DOT AND CIRCLE INDICATE THE LOCATION OF A PRE-EXISTING PILOT WELL AND PREDICTED DRAINAGE. 39
FIGURE 3.8: A PORTION OF SEISMIC SECTION FROM SURVEY SERIES E DATA WHERE THE HIGHLIGHTED AREA IN MAGENTA WAS THE INTERPRETED WAVEFORM ARRIVAL OF THE SMU [MODIFIED FROM *G. CARRINGTON*, 1986B]. 40
FIGURE 3.9: MAP VIEW OF THE SEISMIC DATA WITH THE 117 WELLS INVESTIGATED IN THE AREA. THE BLUE RECTANGLE INDICATES THE AREA WHERE THE GEOLOGICAL MODEL OF FIGURE 3.10 WAS CONSTRUCTED. 42

FIGURE 3.10: PERSPECTIVE VIEW FROM THE SOUTH INTO THE GEOLOGICAL MODEL CONSTRUCTED FROM AVAILABLE WELL DATA (COURTESY OF MR. MOHAMED FATMED) IN AREA INDICATED BY THE BLUE SQUARE IN FIGURE 3.9. NOTE THE MODEL SHOW THAT THE BULK OF WELLS (VERTICAL PIPES) ONLY PENETRATE TO THE SMU.....42
FIGURE 4.1: ILLUSTRATION OF THE APPLIED SEISMIC PROCESSING WORKFLOW USED FOR THIS STUDY. 45
FIGURE 4.2: AN EXAMPLE OF THREE SHOT RECORDS FROM SEISMIC LINE B-04 ILLUSTRATING (A) GOOD SHOT RECORD, (B) CAP ONLY DETONATION AND (C) OPEN LEADS. 46
FIGURE 4.3: (A) MAP OF SURFACE GEOMETRY AND (B) VERTICAL PROFILE FOR SEISMIC LINE B-01 RED LINES EXTENDING BELOW THE SOURCES IN (B) INDICATE DEPTH OF SHOT FROM SURFACE.....48
FIGURE 4.4: FOLD CHART FOR SEISMIC LINE B-01.....49
FIGURE 4.5: SHOT RECORD FROM SEISMIC LINE B-06 DISPLAYING DEAD TRACES FROM CHANNELS 1 TO 44.....49
FIGURE 4.6: (A) CROSS PLOT OF MAXIMUM FREQUENCY VERSUS SOURCE-RECEIVER OFFSET FOR SEISMIC LINE C-11 AND (B) A DISPLAY OF SOME OF THOSE TRACES THAT LIE WITHIN THE REJECTION ZONE. 50
FIGURE 4.7: (A) CROSS PLOT OF RMS AMPLITUDE VERSUS SOURCE-RECEIVER OFFSET FOR SEISMIC LINE C-11 AND (B) A DISPLAY OF SOME OF THOSE TRACES THAT LIE WITHIN THE REJECTION ZONE. 51
FIGURE 4.8: A SHOT RECORD FROM SEISMIC LINE C-03 RECORDED WITH A POLARITY REVERSAL OF CHANNEL 6 HIGHLIGHTED IN RED. 52
FIGURE 4.9: FREQUENCY BANDWIDTH ANALYSIS FOR A GOOD QUALITY SHOT RECORD FROM SEISMIC LINE C-10.....54
FIGURE 4.10: FREQUENCY BANDWIDTH ANALYSIS FOR A POOR QUALITY SHOT RECORD FROM SEISMIC LINE C-10. 55
FIGURE 4.11: SIGNAL TO NOISE RATIO ESTIMATES SUPERIMPOSED TOGETHER WITH A SHOT GATHER FROM SURVEY SERIES C. 57
FIGURE 4.12: AMPLITUDE SPECTRUM IN (A) LINEAR AND (B) DECIBEL FORMAT FOR A SHOT RECORD FROM SURVEY SERIES C. 59
FIGURE 4.13: NATURAL LOGARITHMIC AMPLITUDE DECAY ANALYSIS FOR A SHOT RECORD FROM SURVEY SERIES B. FINE LINE REPRESENTS THE ABSOLUTE PEAK AMPLITUDE AND HEAVIER LINE IS THE GEOMETRIC MEAN AMPLITUDE. 60
FIGURE 4.14: AMPLITUDE RECOVERY OF SEISMIC TRACES FOR (A) RAW SHOT RECORD, (B) SHOT RECORD WITH AN EXPONENTIAL GAIN OF N = 1.5 AND (C) SHOT RECORD WITH GAIN AND SURFACE CONSISTENT SCALING. 61
FIGURE 4.15: ELEVATION AND REFRACTION STATICS FOR SOURCES AND RECEIVERS OF SEISMIC LINE B-05.....62
FIGURE 4.16: (A) SHOT RECORD WITH FIRST BREAK PICKS. IN (B) THE LEFT PANEL IS THE SURFACE MAP SEISMIC LINE B-05 WITH A HIGHLIGHTED CONTROL POINT AND RIGHT PANEL IS THE FIRST BREAK PICKS (BLACK DOTS) WITH THAT CONTROL POINT. THE LINE OF BEST FIT IS RED WHILE THE TOLERANCE RANGE FOR OUTLIERS IS INDICATED BY THE BLUE MESH.....64
FIGURE 4.17: DERIVED MODEL OF THE NEAR SURFACE FOR SEISMIC LINE B-05.....65

FIGURE 4.18: (A) AN ILLUSTRATION OF THE TRANSLATION OF ENERGY FROM A SHOT GATHER ONTO AN F-K PLOT AND (B) F-K PLOT CREATED FROM A SHOT GATHER OF SEISMIC LINE E-01. WARM AND COLD COLORS DEPICT HIGH AND LOW AMPLITUDE OF ENERGY RESPECTIVELY. 66
FIGURE 4.19: GROUND ROLL SUPPRESSION VIA F-K FILTERING METHOD WHERE (A) IS THE ORIGINAL AND (B) THE F-K FILTERED SHOT GATHER FROM SEISMIC LINE E-01. 67
FIGURE 4.20: GROUND ROLL SUPPRESSION VIA BAND-PASS FILTERING METHOD WHERE (A) IS THE ORIGINAL AND (B) THE BAND-PASS FILTERED SHOT GATHER FROM THE 3D SEISMIC SURVEY OF SERIES D. 67
FIGURE 4.21: MUTING OF THE DIRECT WAVE IN A SHOT GATHER (A) BEFORE AND (B) AFTER. 68
FIGURE 4.22: SHOT GATHER AND AMPLITUDE SPECTRUM FROM SEISMIC LINE E-01 (A) ORIGINAL (B) DECONVOLVED AND (C) SPECTRAL WHITENED 70
FIGURE 4.23: AMPLITUDE SPECTRUM ILLUSTRATION FOR THE REFLECTIVITY RESPONSE OF THE EARTH WHERE THE SOLID LINE IS THE RECORDED RESPONSE, DOTTED LINE THE IDEAL CASE AND DASHED LINE SENSIBLE BALANCE VIA SPECTRAL WHITENING OF THE RECORDED RESPONSE 71
FIGURE 4.24: ILLUSTRATION OF REFLECTED RAY PATHS FOR (A) A COMMON SHOT GATHER AND (B) COMMON MID-POINT GATHER WHERE SQUARES AND TRIANGLES ARE REPRESENTATIVE LOCATIONS OF SOURCES AND RECEIVERS RESPECTIVELY. 72
FIGURE 4.25: CROOKED-LINE BINNING OF TRACE MIDPOINTS FOR A PORTION OF SEISMIC LINE A-01. 72
FIGURE 4.26: VELOCITY ANALYSIS FOR CMP #80 OF SEISMIC LINE E-01 WHERE (A) SEMBLANCE PLOT WITH VELOCITY PICKS (WHITE DOTS), (B) CMP GATHER AND (C) CVS PLOTS WITH THE CORRESPONDING VELOCITY PICKS FROM THE SEMBLANCE PLOT (BLUE DOTS). THE RED CROSS, GREEN NMO CURVE AND CYAN CROSS INDICATE AN INITIAL TWO-WAY TRAVEL TIME OF 240 MS AND V_{RMS} VELOCITY OF 2150 M/S. 73
FIGURE 4.27: ESTIMATED FINAL VELOCITY MODEL OF THE EARTH FOR LINE E-01. 74
FIGURE 4.28: ILLUSTRATING THE IMPROVEMENT EFFECTS RESIDUAL STATIC CORRECTION ON A PORTION OF SEISMIC LINE E-01 WHERE (A) IS THE ORIGINAL STACKED SECTION AND (B) THE STACKED SECTION AFTER APPLICATION OF RESIDUAL STATICS AND UPDATED VELOCITY. 75
FIGURE 4.29: STACKING OF A CMP GATHER WHERE (A) IS THE ORIGINAL GATHER, (B) NMO CORRECTED, CMP GATHER, (C) WITH STRETCH MUTE APPLIED AND (D) THE FINAL STACKED TRACE BY SUMMING OF TRACES IN (C). 77
FIGURE 4.30: A SIGNAL OF PERIOD T (A) IS STRETCHED TO A SIGNAL OF PERIOD $T_0 > T$ (B) AFTER NMO CORRECTION. 79
FIGURE 4.31: STACKED SECTION FOR SEISMIC LINE E-01. 80
FIGURE 4.32: FD MIGRATION FOR SEISMIC LINE E-01 81
FIGURE 4.33: PSTM IMAGE FOR SEISMIC LINE E-01. 82
FIGURE 4.34: WHITE NOISE SUPPRESSION FOR SEISMIC LINE B-02 WHERE (A) IS THE FINAL STACKED SECTION, (B) CLEANED STACKED SECTION AND (C) THE DIFFERENCE BETWEEN (A) AND (B). 83
FIGURE 5.1: TWO LAYER GEOLOGICAL MODEL ABOUT THE SMU WITH (A) A SINGLE KARST FEATURE AND (B) MULTIPLE KARST FEATURES VARYING IN WIDTH AT THE SMU 87

FIGURE 5.2: SOURCE SIGNATURE OF A MINIMUM PHASE RICKER WAVELET WITH DOMINANT FREQUENCY 40 HZ DISPLAYED IN (A) TIME AND (B) FREQUENCY DOMAIN. 89
FIGURE 5.3: SNAP SHOT AT 210 MS AFTER SOURCE IMPULSE OF SIMULATE, PROPAGATING SEISMIC WAVE THROUGH THE TWO-LAYER MODEL. 90
FIGURE 5.4: SYNTHETIC CMP STACKED SECTIONS AND PSTM SECTIONS FOR THE TWO LAYER GEOLOGICAL OF A SINGLE SIMULATED KARST FEATURE PLACED ALONG THE SMU. THE DEPTH OF THE KARST FEATURE WAS HELD AT 20 M WHILE THE WIDTH WERE VARIED AT (A) 10M, (B) 40 M, (C) 80 M, (D) 120 M, AND (E) 160M. 91
FIGURE 5.5: SYNTHETIC CMP STACKED SECTIONS AND PSTM SECTIONS FOR THE TWO LAYER GEOLOGICAL OF MULTIPLE KARST FEATURES PLACE ALONG THE SMU. (A) CMP STACKED AND (B) PSTM SECTIONS OF MULTIPLE KARST FEATURES AT A COMMON DEPTH OF 20 M WITH WIDTHS (DENOTE ON THE SECTIONS) VARYING FROM 10 TO 200 M. (C) CMP STACKED AND (D) PSTM SECTIONS OF MULTIPLE KARST FEATURES AT A COMMON DEPTH OF 40 M WITH WIDTHS (DENOTE ON THE SECTIONS) VARYING FROM 10 TO 200 M. 92
FIGURE 5.6: ILLUSTRATED MAP VIEW OF THE PRE-MIGRATED FRESNEL ZONE WITH RADIUS *R* AND POST-MIGRATED FRESNEL ZONE WITH MINOR AND MAJOR AXIS *A* AND *B* WITH RESPECTS TO PROFILE DIRECTION. 93
FIGURE 5.7: ILLUSTRATED MAP VIEW OF THREE SEISMIC LINES PROFILING A NARROW KARST VALLEY PRESENT AT THE SMU SURFACE. 95
FIGURE 5.8: ILLUSTRATED MAP VIEW OF A SEISMIC LINE PROFILING A SMALL DOLINE PRESENT AT THE SMU SURFACE. 96
FIGURE 6.1: SCHEMATIC DIAGRAM OF THE ROCK-PHYSICS MODEL USED FOR THIS STUDY .. 99
FIGURE 6.2: MODELED VISCOSITY-TEMPERATURE PROFILE OF GROSMONT BITUMEN. THE ERROR BAR REFLECTS THE VISCOSITY MEASUREMENTS AT 20°C BY ZHAO AND MACHEL [2009]. 100
FIGURE 6.3: STORAGE MODULUS TEMPERATURE-FREQUENCY DISPERSION OF THE MODELED GROSMONT BITUMEN. 101
FIGURE 6.4: ACOUSTIC VELOCITY OF P-WAVE (SOLID LINES) AND S-WAVE (DASHED LINES) AGAINST POROSITY FOR THE MODELLED GROSMONT RESERVOIR AT 11 °C WITH A 50 HZ SIGNAL. CPA MODELLED RESULTS ARE THE THICK LINES AND THE RIGOURS UPPER AND LOWER HAHIN-STRIKMAN BOUNDS ARE THE THIN LINES. 103
FIGURE 6.5: MODELLED TEMPERATURE-FREQUENCY DISPERSION OF P AND S WAVE VELOCITY AT 22% POROSITY 103
FIGURE 6.6: MODELLED TEMPERATURE-FREQUENCY DISPERSION OF P AND S WAVE VELOCITY AT 40% POROSITY 103
FIGURE 7.1: ATTENUATION RESPONSE OF THE RECEIVER ARRAY IMPLEMENTED BY SURVEY SERIES A (BLUE LINE). THE CALCULATED ATTENUATION RESPONSE FOR A REFLECTED WAVE FROM A SHALLOW MESOZOIC HORIZON AND THE SMU HORIZON ARE SHOWN BY THE MAGENTA AND GREEN LINE, RESPECTIVELY. THE RED LINE INDICATES THE ATTENUATION RESPONSE FOR GROUND ROLL. 107
FIGURE 7.2: FINAL PROCESSED SECTION OF THE NORTH REGIONAL LINE (A-01) WITH INTERPRETED LITHOLOGIES SUPERIMPOSED. 109
FIGURE 7.3: FINAL PROCESSED SECTION OF THE SOUTH REGIONAL LINE (A-02) WITH THE INTERPRETED LITHOLOGIES SUPERIMPOSED. 110

FIGURE 7.4: MAP OF LOCAL AREA DEFINED BY DASH-DOTED BOX FOR THE INTERPRETATION AT LOCAL SCALE. 112
FIGURE 7.5: (A) LEFT PANEL SHOWS THE IMAGE OF VSP FROM SCHACTER [1985] FOR WELL LOCATION W-01. THE RIGHT SIDE SHOWS THE ONE WAY TRAVEL TIME OF THE VSP DATA (BLUE DOTS) SUPERIMPOSED ON THE GAMMA LOG. (B) SYNTHETIC TRACE GENERATED FROM THE SONIC AND DENSITY LOG. 113
FIGURE 7.6: DISPLAYING INLINE AND CROSSLINE PROFILES OF THE GENERATED VELOCITY MODEL. 114
FIGURE 7.7: PORTION OF SEISMIC LINE E-01 SHOWING THE SIX CHOSEN HORIZONS FOR MAPPING AND FURTHER ANALYSIS 115
FIGURE 7.8: COMPARISION OF SURFACE MAPS FOR THE SMU OF GENERATED FROM (A) WELL ELEVATION DATA, (B) SEISMIC DATA IN TIME AND (C) SEISMIC DATA IN ELEVATION. 116
FIGURE 7.9: SEISMIC TIME SURFACE OF THE SMU WITH INTERPRETED STRUCTURES OF A, B, AND C. BLACK LINES INDICATE THE HIGH-RESOLUTION SEISMIC SURVEYS. 117
FIGURE 7.10: FEATURE C, AN IMAGED KARST VALLEY IN THE SEISMIC DATA OF (A) TIME MAP OF THE SMU, (B) PORTION OF SESIMIC LINE E-01 PROFILING A-A' AND (C) GEOMETRY OF APPARENT WIDTH AND TRUE WIDTH OF KARST VALLEY AND SUB-CHANNEL. 118
FIGURE 7.11: COMPARISION OF THE SURFACE MAPS IN TIME DOMAIN FOR THE (A) MESOZOIC SEISMIC HORIZON 1, (B) MESOZOIC WABISKAW, (C) SMU, (D) PALEOZOIC LOWER IRETON, (E) PALEOZOIC SEISMIC HORIZON 7 AND (F) PCU. ARROWS DENOTE THE PROGRESSION OF THE PANELS WITH SUBSECENTLY INCREASING DEPTH. 119
FIGURE 7.12: MAXIMUM RMS AMPLITUDE MAP OF THE SMU HORIZON. 120
FIGURE 7.13: INTERPRETATION OF A COLLAPSED DOLINE IN SEISMIC LINE B-04. ORANGE LINES INDICATE POSSIBLE FAULTING. 121
FIGURE 7.14: SEISMIC TIME MAP OF THE SMU WITH INTERPRETED KARST FEATURES 123

Chapter 1 Introduction

1.1. Introduction

The Devonian Grosmont and Nisku Formations (Figure 1.1) of the northeastern Alberta plains are projected to hold upwards of 64.5×10^9 m^3, and 10.3×10^9 m^3, respectively, of bitumen according to the recently updated reserves estimates of the Energy Resources Conservation Board [*ERCB*, 2010]. The Grosmont Formation is a Devonian carbonate platform that encompasses an area of about 85000 km^2 or 13% of Alberta. This has often been compared in size to the current day Bahama Banks (Figure 1.2). Of the Grosmont Formation region, about 20800 km^2 (300 townships) are believed to be prospective for bitumen. This is believed to be the single, largest carbonate hosted heavy oil deposit in the world. The Grosmont reserve was revised upwards nearly 28% in [*ERCB*, 2010] reflecting contributions from additional drilling data that has become available. This 74.8×10^9 m^3 is a sizeable fraction of the total ~287×10^9 m^3 of all the anticipated bitumen resources in Alberta. As such, the Grosmont Formation in particular has garnered a great deal of attention over the last half-decade; and a number of companies have purchased rights to the resource with pilot plants with further plans for expansion of recovery programs now being developed. Evidence of rising interest is reflected in paper presentations on the topic of the Grosmont formation and bitumen appraisal at the 2010 International Conference of the American Association of Petroleum Geologists held in Calgary, Alberta [*K R Barrett and Hopkins*, 2010; *Borrero-Gomez*, 2010; *Wagner et al.*, 2010; *Wo et al.*, 2010].

This is the second wave of interest in the region the first took place in the early 1980's. At that time, the Government of Alberta through the Alberta Oil Sands Technology and Research Authority (AOSTRA) invested with Union Oil and Canadian Superior in a number of pilot project tests. This earlier work is hereafter referred to as the AOSTRA Project, and in addition to a number of different injection tests included extensive geological and geophysical studies

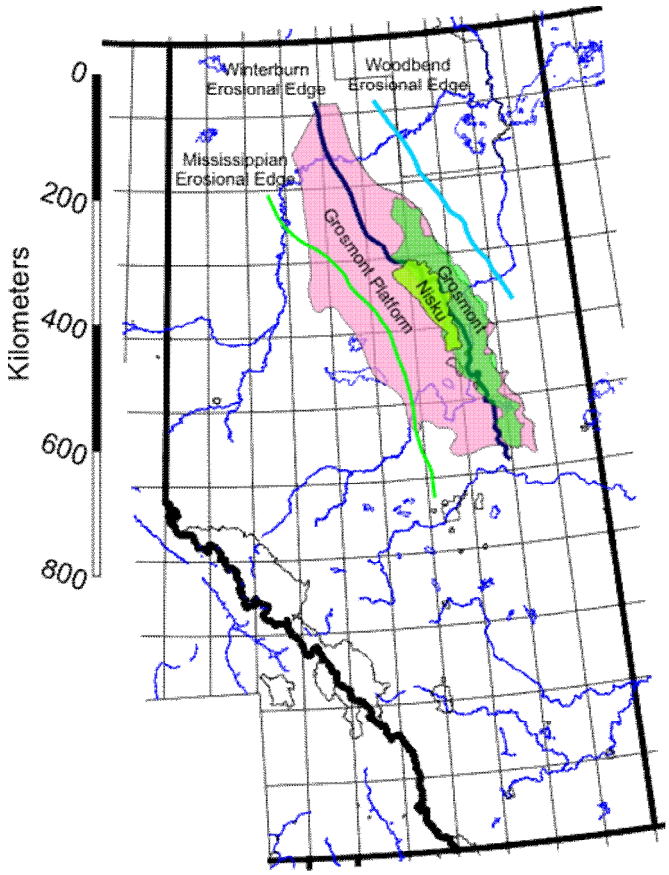

Figure 1.1: Alberta map showing the extent of the Grosmont Platform [modified from *Buschkuehle et al.*, 2007] and carbonate bitumen deposits of the Nisku and Grosmont [*ERCB*, 2009a].

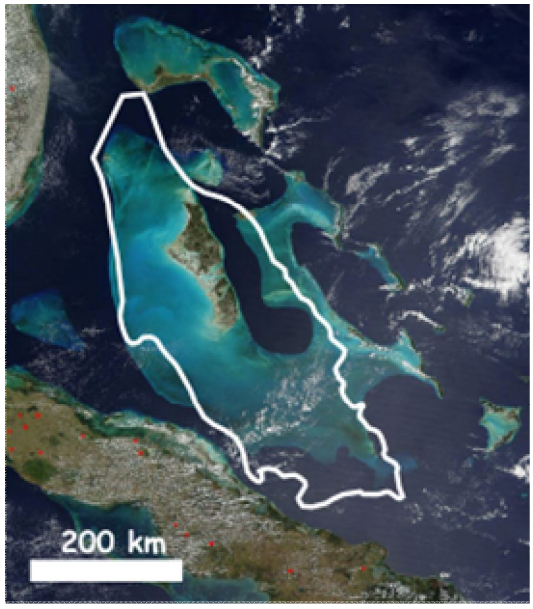

Figure 1.2: Satellite image of the Bahama Banks illustrating the size of a modern day shallow water carbonate platform. Concept after Harrison [1984].

A good deal of the geological information has already been published from various sources and entered the public record. To our knowledge, however, there have been no reports of the geophysical studies in this area. Further, the AOSTRA Project financed an extensive experimental seismic program over the pilot sites. Unfortunately, few details on the analyses of these data were provided in the AOSTRA Project reports[1] and with the abrupt termination of the AOSTRA Project in 1986, no detailed summaries are available; the work remained incomplete.

The work presented in this study attempts to provide an overview of the regional seismic character and re-examining much of the seismic data obtained in by the AOSTRA Project in the 1980's. The study begins with a review of literature relevant to geophysical investigation of complex carbonate formations that leads to a numerical study of the types of seismic responses that might be expected from karst-like features. The bulk of the study, however, consists of reprocessing and interpretation of two regional seismic lines in the area as well as most of the AOSTRA Project seismic data. These latter AOSTRA Project data are, too, for the first time simultaneously processed to allow them to be merged. The study ends with recommendations for future studies particularly about issues of fracture anisotropy, karst features detection, and seismic monitoring.

[1] That is, reports available through the Carbonate Research Program 'Carbosearcher' database of scanned Project documents.

Chapter 2 Literature Review

2.1. Overview

This chapter reviews the current understanding of the geology surrounding the Grosmont formation that is buried beneath much of northeastern Alberta. The Grosmont depositional environment, diagenesis, erosion, and eventual burial and uplift to its present day subsurface depth is reviewed along with the geological framework of which allowed for the migration and entrapment of with bitumen the formation. Some details into documented observations are present to support evidence that the erosional surface of the Grosmont under went serious dissolution and plausible karstification, however little is known as to the nature and degree of karst features present in the upper members of the formation. At this point the chapter breaks away into review of karst geomorohology. This enables an assessment of features that one might expect to encounter when investigating the Grosmont formation. Lastly, a review of geophysical sensing techniques is present followed by an in-depth look into reflection seismology and case studies for the detection of karst features in the subsurface.

The literature review suggests that the Grosmont formation in the area of our project is a highly heterogenic bitumen reservoir of which karsting is evident along subcropping edge of the formation between Devonian and Cretaceous aged rocks. The Grosmont by convention is divided into four carbonate members listed bottom to top of A, B, C and D units separated by interbedded shales. Grosmont members C and D are highly dolomitized, bitumen saturated and their dominant pore structures vary from microcracks and fractures to interpartical pores and large vugs. Grosmont members A and B are mostly limestone with little in-place hydrocarbon. The expected karsting of the upper members of the Grosmont may include such features as dolines, epikarsts, blind valleys, and caves.

Geophysical case studies over similar buried carbonate terrains of the Grosmont formation convey that reflection seismology has a high potential to measure and map features of karstification.

2.2. Geological Background

While much remains to be learned, particularly concerning second order features, it appears there is a consensus as to the overall geological structure of the Grosmont formation within the Western Canadian Sedimentary Basin (Figure 1.1). At this point, it may be useful to also indicate that in the broader context both the overlying Upper Ireton and Nisku formations also share many of the same characteristics and prospectively, and one needs to include these when referring to the 'Grosmont' generically.

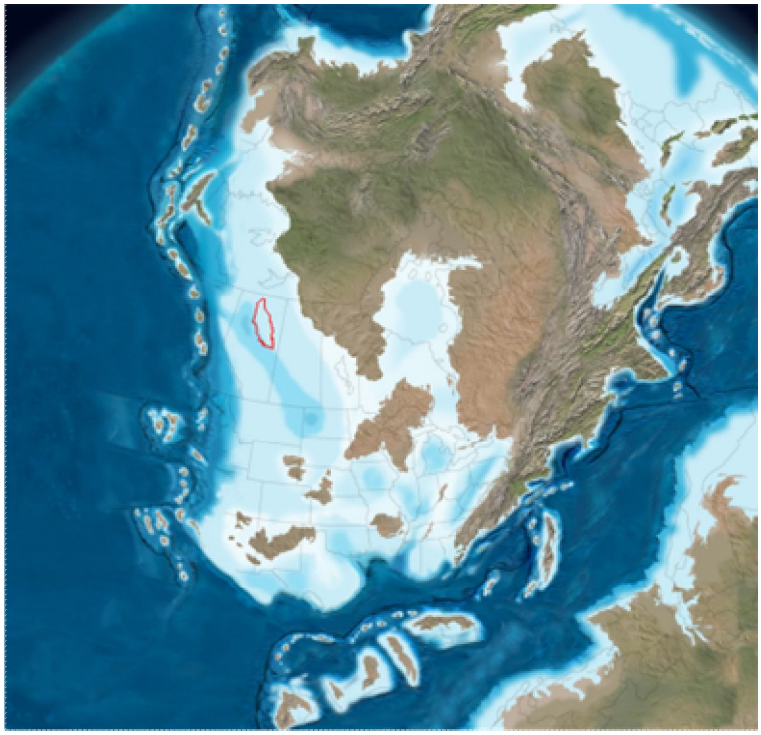

Figure 2.1: Paleogeographic reconstruction map of North America during the Late Devonian era (360 Ma) courtesy of Dr. Ron Blakey [2011] with present-day Grosmont Platform outlined in red.

Briefly, during most of the Paleozoic (542 to 251 Ma) the continental crust beneath current day Alberta resided near the equator and during the later parts of the Devonian period (~416 to 360 Ma) was a large intracratonic sea [*Switzer et al.*, 1994] on the western margin of the current North American Craton (Figure 2.1). This setting of a passive continental margin stretching from the Arctic to Wyoming submerged beneath warm shallow seas provided the conditions for deposition of vast quantities of limestone and shale as well as allowing the growth of series of carbonate reef complexes nearly 300 m high. It is these lithologies and

what has happened to them in the intervening periods that control the present day resource of the Grosmont formation.

Although a highly detailed account of the Devonian sediments of interest is found in Switzer et al. [1994] and Machel [2010] has recently provided a concise overview of the Devonian petroleum systems in the Western Canada Sedimentary Basin. Briefly, this consists of four distinct and major cyclical stratigraphic units that each include porous carbonates and source and trapping shales, marls, and evaporites. These units are D4 – Middle Devonian Swan Hills, and the upper Devonian D3 – Woodbend group (that includes the Grosmont platform), D2 – the Winterburn group (that includes the Nisku formation), and D1 – the Wabumun Group. According to Machel [2010] fluids moved roughly from SW to NE across the basin nearly independently within each of these groups.

At the basin scale, the Woodbend-Winterburn groups are particularly noteworthy as they resulted during a time of rapid basinal subsidence and high rates of sediment deposition superposed with variations in eustatic sea levels. Sediment thicknesses exceed 850 m in some locations and according to Switzer et al. [1994] this accumulation is exceptional in that it occurred within a relatively short period of time during the Frasnian Age (~375 Ma to 385 Ma).

As noted, the Grosmont platform lies within the Upper Devonian Woodbend Group (Figure 2.2). Over the last half century, geologists have further chronostratigraphically classified its sediments into five stratigraphic intervals called the Cooking Lake, the Majeau Lake/Lower Leduc, the Duvernay/Middle Leduc, the Lower Ireton/Upper Leduc and the Leduc formations. Each of the intervals has been interpreted to represents a cycle of relative sea rise in which reefs and shelf carbonates were built up followed by relative sea level fall with seaward deposition (progradational) of shales and marls.

This structure is further manifest in the bedrock geology of Alberta (Figure 2.3) with the ancient Canadian Shield rocks outcropping in the extreme NE corner of Alberta. A few of the Paleozoic carbonates border these Canadian Shield rocks, with the bulk of the Devonian carbonates underlain by the later

Cretaceous and Tertiary sediments. The Grosmont platform, except for some limited outcrop along the Peace River, underlies

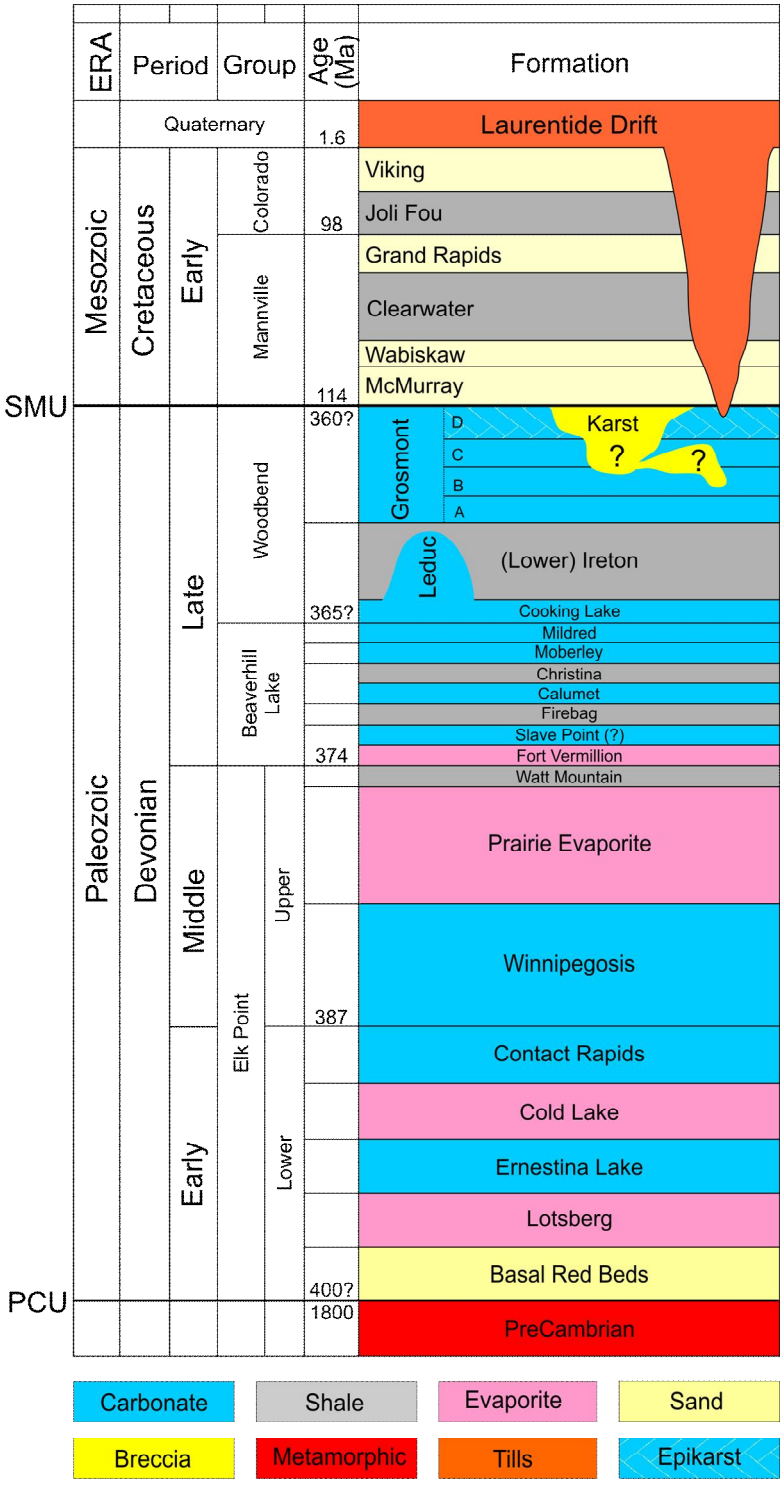

Figure 2.2: Generalized stratigraphy for the study area constructed and modified from ERCB [2009b]. Highlighted is the SubMannville unconformity (SMU) and PreCambrain unconformity (PCU).

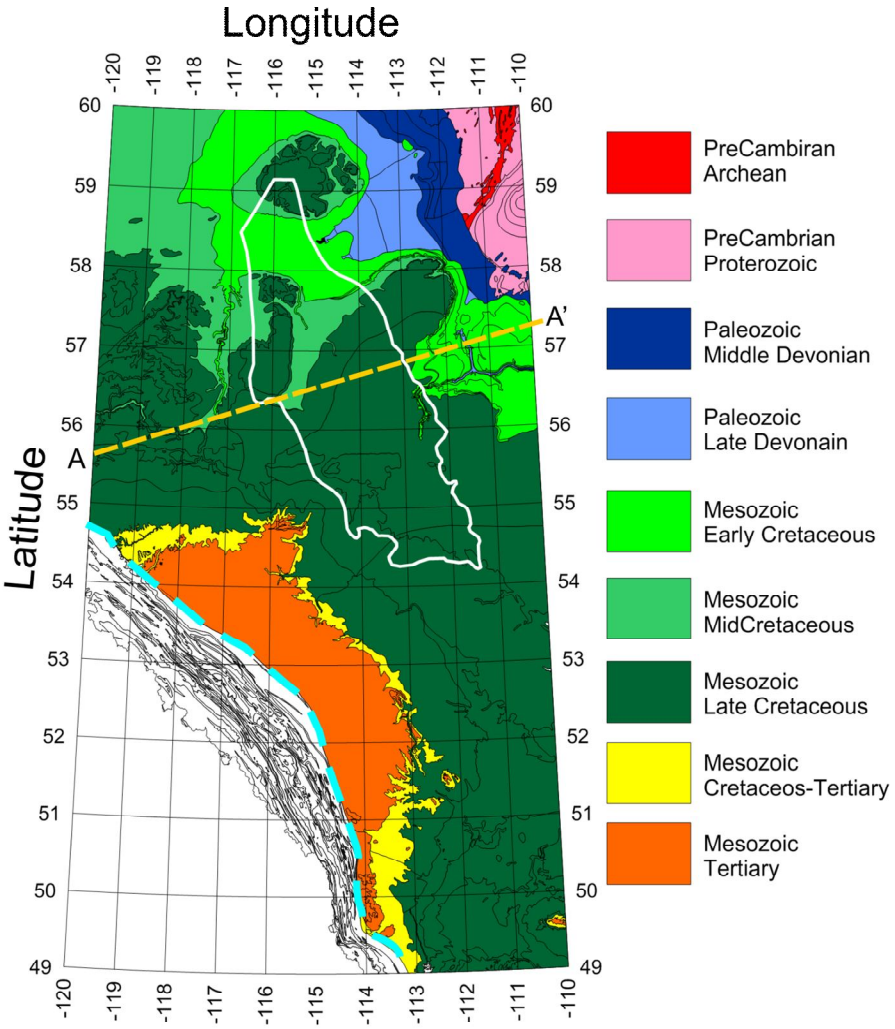

Figure 2.3: Bedrock map of Alberta modified from Mossop and Shetsen [1994] with Grosmont Platfrom outlined in white. Line A-A' show the location of the cross-section for Figure 2.4(a).

Cretaceous sediments. The cross-section A-A’ of Figure 2.4(a) shows the large scale geological structure representative of the study area. This figure highlights the predominant lithologies within the various sedimentary layers overlying the Canadian Shield beginning with the lower Devonian Elk Point formation containing significant evaporates (e.g. salt, anhydrite) and carbonates, the mid to upper Devonian Beaver Hills Lake group, the Upper Devonian Woodbend-Winterburn group, and the Upper Devonian and Mississippian Wabamum and other formations. These are all blanketed by the Lower Cretaceous Manville Group which is in turn covered by Upper Cretaceous and, in some locales, Tertiary sediments.

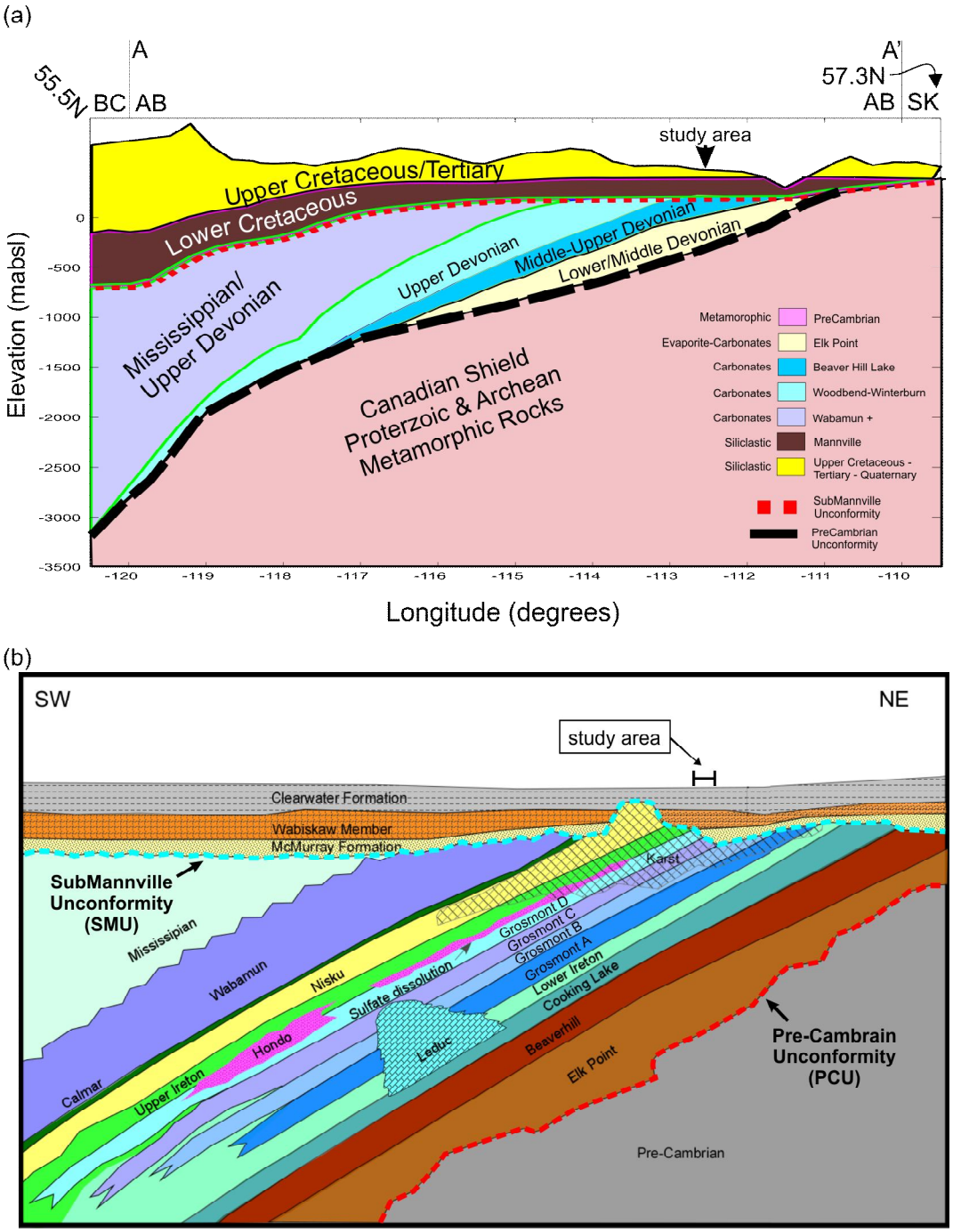

Figure 2.4: (a) A synoptic cross-section of A-A' from Figure 2.3 showing the general geology structure through the area. Developed from Mossop and Shetsen [1994]. (b) Cross-section of the gross geological structure in the study area [modified form *Borrero-Gomez*, 2010].

The general simplified regional stratigraphy of Figure 2.4(b) exaggerates the gentle westward dip of these various formations and shows how they subsequently subcrop at the SubManville unconformity (SMU) beneath the Cretaceous Fort McMurray – Wabiskaw formations. It is useful to note that the

SMU at the Devonian Grosmont – early Cretaceous McMurray contact represents a gap of more than 220 Ma of missing geological record. This unconformity goes by many different names in the literature (e.g., subCretaceous, Paleozoic) but here we employ 'SubMannville' because the Lower Cretaceous Mannville Group covers the subcropping Upper Devonian rocks in our study area.

There are two unconformities highlighted in Figure 2.4(b). The second is the unconformity between the Lower Devonian Elk Point and the 'PreCambrian' metamorphic Canadian Shield. The PreCambrian unconformity (PCU) separates the rocks in time by more than 1.5 Ga. While this unconformity will not play a major role in this study, it is important not to forget it as it may hold clues as to the potential for large scale tectonic motions that could directly via faulting or indirectly via deformation influence the shallower Upper Devonian formations being studied here [*Cotterill and Hamilton*, 1995].

Extensive discussions of the Devonian geology may be found in a number of dissertations [*Borrero-Gomez*, 2010; *Cutler*, 1982; *Huebscher*, 1996; *F. Theriault*, 1984] Briefly, however, the Grosmont 'member' was first described from cuttings from the Imperial Grosmont No. 1 13-17-67-23W4 as well as cores from nearby wells [*Belyea*, 1952] and subsequently promoted to the Grosmont 'Formation' in *Law's* [1955] early discussion of the geology of northwest Alberta. The large extent of the Grosmont formation was soon delineated by Belyea [1956] from drill results and from the rare outcrop at the Vermillion Chutes rapids along the Peace River described by Norris [1963]. This work suggested that the Grosmont formation subcrops beneath an area in excess of 100,000 km^2 extending along a northwest trend over 400 km in length and up to 150 km in width (Figure 1.1).

After this, there did not appear to have been a great deal of work focussed on the Grosmont formation itself aside from more general discussions of Devonian systems until Cutler [1983] carried out detailed interpretation of cores and logs. He arrived at a general framework that delineates the Grosmont formation into four regionally correlatable argillaceous units of Lower Grosmont (LGM), and the Upper Grosmont (UGM) 1, 2, and 3 units based on log-markers

(Figure 2.5). It is important to note that these are also referred to as the Grosmont A, B, C, and D units [see *ERCB*, 2010] and are adopted in

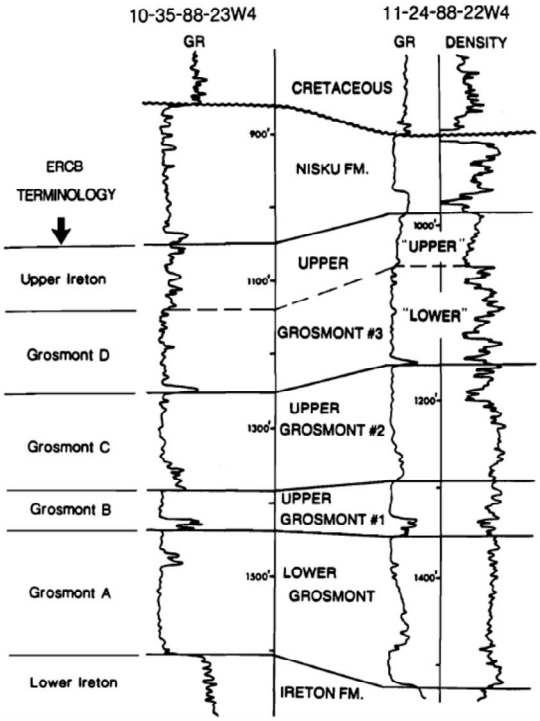

Figure 2.5: Representative natural gamma ray log deliniation of the Grosmont [modified from *R S Harrison*, 1986].

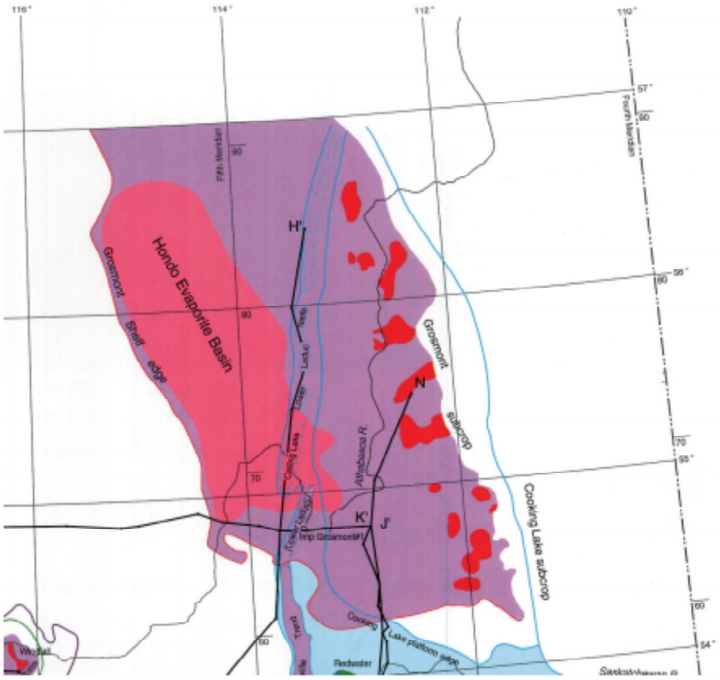

Figure 2.6: Areal extent of the topmost Hondo Evaporite Basin [modified from *Switzer et al.*, 1994].

this report. The base of each of these units, often clearly seen in gamma-ray logs [i.e. *Cutler*, 1983; *Dembicki*, 1994; *R S Harrison*, 1986; *Huebscher*, 1996] were interpreted to be platform-wide deposits of marine shales produced by transgressive events. Additionally, in the western parts of the formation, the anhydritic 'Hondo' evaporate lies at the top (Figure 2.6) (see Figure 12.11 of Switzer [1994] for a detailed illustration of the mapped areal extent of these units and the recent thesis of Borrero-Gomez [2010]). Regardless, as there have been a number of different schemes used to describe these deposits, care must be taken when making comparisons between the various literature contributions.

The younger Grosmont units cover larger areas as their edges grew progressively westward with the subsequent transgressive cycles. A proposed history of the construction of the platform of Figure 2.7 shows a number of cycles of deposition on top of the Cooking Lake platform resulting from eustatic sea level variations.

After this construction, the platform underwent numerous changes including dolomitization of most of the rocks, by uplift, erosion, and karstification, and finally burial in the early Cretaceous.

Briefly, calcite ($CaCO_3$) is the major constitutive mineral of the originally deposited limestones. It is converted to dolomite ($(CaMg)(CO_3)^2$) by the addition of Mg rich fluids. Although the origin of the dolomite in older sedimentary rocks is not well understood, and likely is due to issues of chemical kinetics, it is usually accepted that the Mg ions replacing Ca in the calcite are delivered by large amounts of either seawater or tectonically driven ground waters [*Holland and Zimmerman*, 2000; *Machel*, 2005; *F. Theriault*, 1984; *Francois Theriault and Hutcheon*, 1987].

The source of the dolomite in the Grosmont is somewhat beyond this study, but Machel [2010] presents a model of dolomitization that began penecontemporaneously (i.e. during or shortly after initial deposition) with reflux dolomitization. This was followed by pervasive replacive dolomitization from rising formation brines that were able to migrate through the tight aquitards between the Cooking Lake formation and the various Grosmont units and

suggests that water-rock interactions generally decrease upwards in the column. Machel [2010] suggests this replacement dolomitization occurred in the latest Devonian – early Mississippian times. It must be noted, however, that this

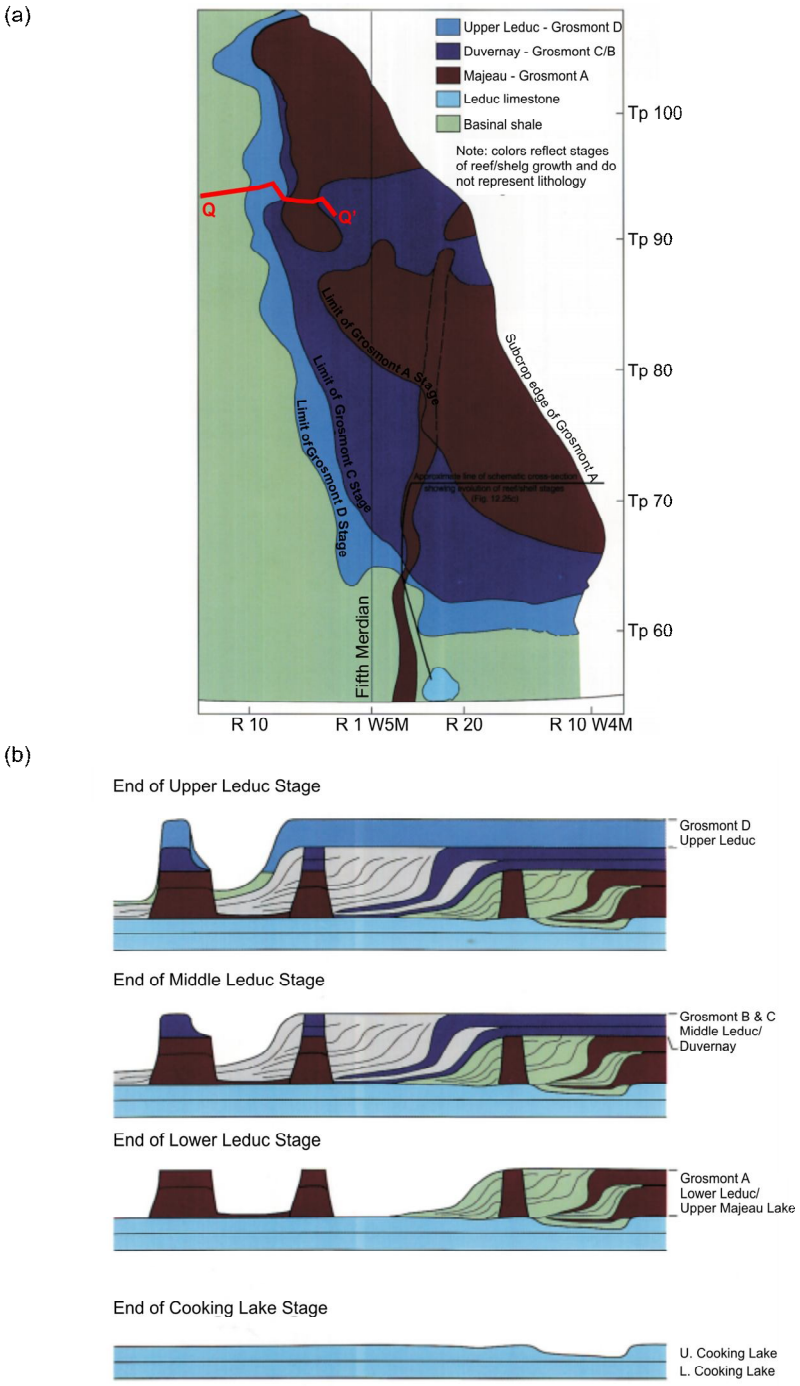

Figure 2.7: Proposed development of the Grosmont Platfrom (a) areal view and (b) profile view of Q-Q' [modified from *Switzer et al.*, 1994]

interpretation does not appear to agree with the recent detailed studies of Hopkins and Jones [2009] who find that the two lowermost Grosmont units A and B are predominantly limestone in their study area, although the main bitumen saturated C and D zones have experienced significant dolomitzation.

The bitumen within the Grosmont deposit is thought to originate from the high organic content Duvernay formation but biodegradation does not allow for unequivocal identification; and the extent to which hydrocarbons from the prolific Mississippian Exshaw formation occur is unknown [*Machel*, 2010].

The above lays out the general framework of the area, but the smaller scale structures superimposed on this framework are crucial to the development of the resource. However, the successes of the early pilot projects in the area were hampered by the apparently extreme heterogeneity of the Grosmont Formation beneath the SMU. This was evidenced by:

- rapid changes in the 'stratigraphy' depth of the unconformity observed from wellbores only a few tens of metres apart,
- anisotropic paths of fluid communication between wells during injection,
- vertical disruption and repeated sampling of sediment zones within a single well, and
- reports of rapid 'drops' of the drill string by a few metres possibly suggesting open cavities.

These limited borehole observations made the development of a representative geological model difficult; and these observations were most easily explained if the upper portions of the Grosmont beneath the SMU had undergone dissolution and erosion leading to karsts and perhaps even caves. In the later stages of these early pilot projects, effort was focussed on using the high-resolution seismic surveys to locate the karst features with limited success. These were able to show, via indirect scattered seismic energy, the existence of sharp doline-like features at the SMU (see Machel [2010]).

That said, geophysics could contribute to an understanding of the resource in general, and site planning. Mapping the topography of the unconformity may

show karst features that contributed to the removal of Grosmont members C and D, and thus affecting the presence of the bitumen reservoir itself. In addition, there is the possibility to use anisotropic responses to look for fracture patterns. The next section briefly reviews knowledge of the topography and inner structure of karsted areas as these may provide comparative analogues for understanding of structures seen in the subcropping Grosmont.

2.3. Karst Geomorphology

As noted in the previous section, erosional surfaces and karst features are important to the Grosmont as consequently they may influence the presence and production of hydrocarbons. Detecting and delineating such features will be crucial aspect in the evaluation of the resource. This fact is perhaps most relevant to 'remote' geophysical probing of seismic data to provide a reasonable context the interpretation of karst. In order for the problem to be fully understood, a brief overview of the structures associated with karst terrains is presented in order to prepare the reader for a literature review of geophysical studies related to karsting.

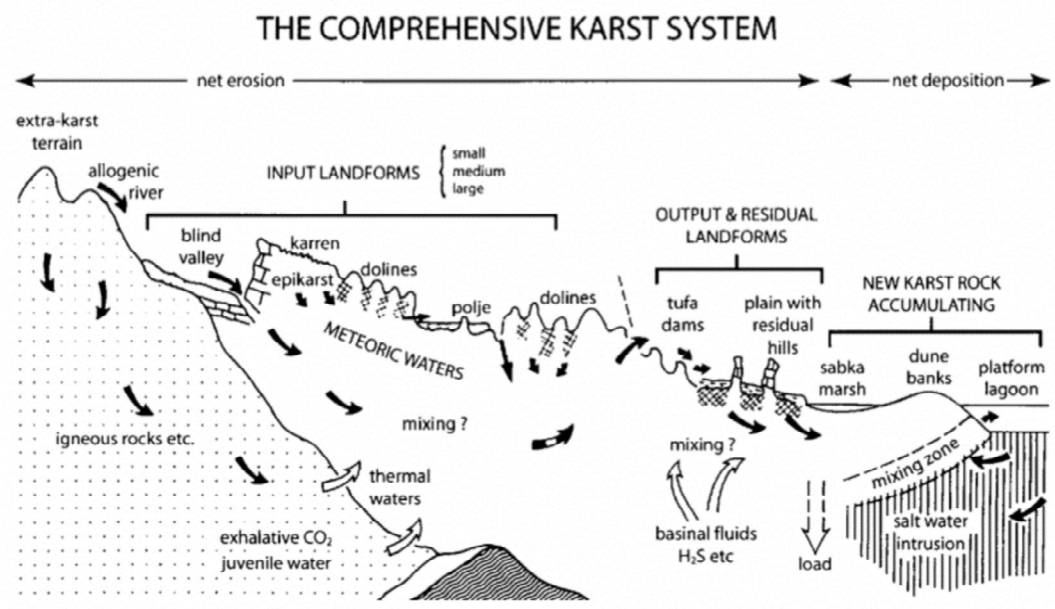

Figure 2.8: Schematic cross-section showing features and fluid flows within an active karst system [reproduced from *Ford and Williams*, 2007].

'Karsting' is a large topic and discussed in numerous texts [*Field*, 2002; *Ford and Williams*, 2007; *Jennings*, 1985] and even specialized journals, so only a brief review focussing on karst geomorphology is necessary or even possible here. Ford and Williams [2007] define karst as: "comprising terrain with distinctive hydrology and landforms that arise from a combination of high rock solubility and well developed secondary (fracture) porosity. Such areas are characterized by sinking streams, caves, enclosed depressions, fluted rock outcrops, and large springs"

Surface karst landforms result from dissolution in what is referred to as the erosional zone and a number of more major features are shown in Figure 2.8 that, following Field [2002], include:

Cave: A natural underground opening large enough for a man to enter and that can consist of a series of chambers connected by galleries. In the context here, it is formed by dissolution of carbonate rocks. Smaller underground features also produced in this way, but too small for a man to enter, can be called proto-caves, sub-conduits, fissures, and vugs to name a few of these conduits. A common linkage is that these are natural voids with connect input and output sites of an aquifer. These could have a geophysical response given the large contrasts between the carbonate rocks and the void or its fill.

Doline (sinkhole): A closed, funnel-shaped depression in karsted surfaces that results from either surface dissolution or collapse of underlying rock. Watercourse disappears underground into either a cave or shaft at the location. Dolines may be cylindrical, conical, bowl, or dish-shaped. Their dimensions can range from a few to many hundred metres in size (Figure 2.9). It is also a general term for a closed depression (i.e. a doline see Figure 2.9. Numerous classficiations of such features can be made but the simple descriptions of [*Jennings*, 1985] are given here. These consist of:

- Collapse dolines (Figure 2.10(a)) that result from the collapse of a cave roof, solution or dissolution dolines (Figure 2.10(b)) occurring at zones of concentrated water flow and which fill with insoluble residues (e.g. clays).
- Subsidence dolines that develop in areas with thick overlying deposits that subside intermittently (Figure 2.10(c)), subjacent karst, caprock, or dropout dolines are found in overlying noncarbonated deposits that results from cave collapse in the underlying carbonates (Figure 2.10(d)).
- Alluvial stream sink dolines in which streams disappear though overlying alluvium to the buried underground karst network (Figure 2.10(e)).

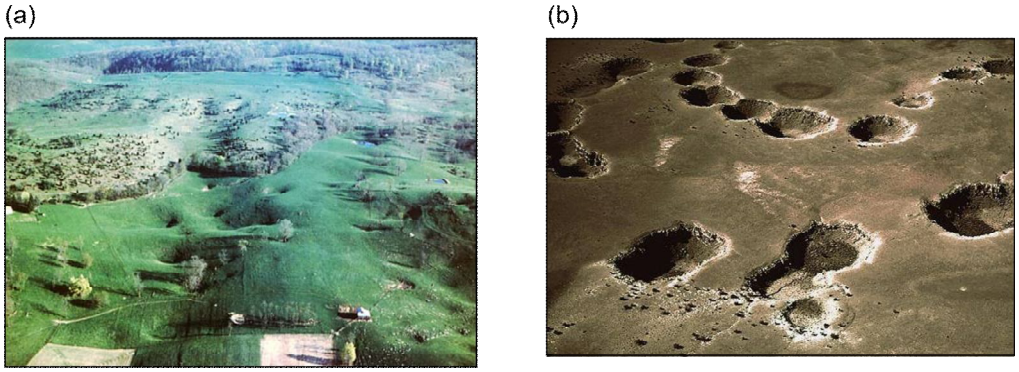

Figure 2.9: Air photos of dolines in (a) karst terrain near Lewisburg, West Virginia, U.S. (courtesy of William K. Jones and Virginia Speleological Survey) and (b) Permian limestone near the Little Colorado River southeast of Winslow, Arizona, U.S. (courtesy of Louis J. Maher, Jr.).

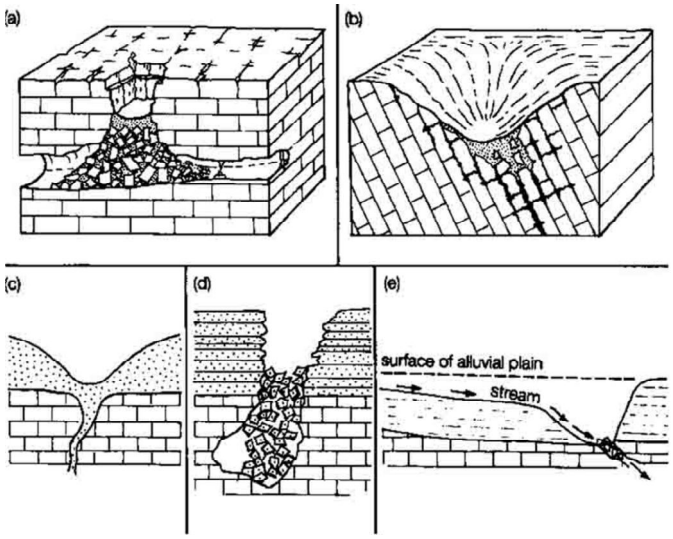

Figure 2.10: Types of dolines (a) collapse, (b) solution, (c) subsidence, (d) subjacent and (e) alluvial stream sink [reproduced from *Jennings*, 1985].

Karst valley: Elongated solution valley in carbonate rock. Most are either blind (due to being closed where the drainage sinks underground), headless or pocket (where river emerges from spring), or dry (flow has been lost to underground capture).

Blind valley: A karst valley that ends abruptly when the watercourse disappears underground. Water may run in this valley intermittently or the valley may be dry due to the loss of the watercourse further upstream. Medicine Lake in Jasper National Park is a blind valley (Figure 2.11).

Figure 2.11: Photograph of Medicine Lake in Jasper National Park.

Dry Valley: A valley without any surface watercourse channel. Valley formed by the collapse or subsidence of a cavern roof. Examples of dry karst valleys near Nahanni National Park are visible in Figure 2.12.

(a) (b)

Figure 2.12: Two air photos of a dry valley near Nahanni National Park, NWT (courtesy of Dr. Paul Sanborn). Dolines are also visible in (b).

Polje: A large flat-floored depression in karst carbonate, whose long axis is developed parallel to major structural trends. Drainage may be by either surface watercourse (an 'open' polje) or surface entry (a 'closed' polje) through doline depressions or swallets. This surface has the potential to be flooded. Medecine Lake can also be considered a polje.

Epikarstic: The dry zone above the water table and beneath the soil in a karsted environment through which surface and meteoric waters must first pass. Figure 2.13 gives an excellent example of this, including a sediment-filled doline, from Sicily.

Figure 2.13: Cutaway limestone face in a construction area in Sicily exhibiting a buried sinkhole on the left and dissolution fissures on the right [reproduced from *Waltham and Fookes,* 2003]. Person is shown on bottom left corner for scale.

This short list of definitions, for more information see Field's [2002] lexicon which is over 200 pages in length.

Waltham and Fookes [2003] attempted to classify various karst features for engineering purposes, and they pay a great deal of attention to the types of karst surfaces that can be encountered. Such knowledge is key if stable structures are to be constructed. Their classifications are reproduced in Figure 2.14 and provide an overview of what surfaces can look like:

- Juvenile surfaces (Figure 2.14(a)) are encountered only in arid and periglacial zones. The surface is relatively uniform with limited fissuring and rare sinkholes and caves.
- Youthful surfaces are found in temperate regions and have small solution sinkholes and stream sinks. The subsurface has many small caves (< 3 metres in across) while the near surface rockhead has many small fissures. (Figure 2.14(b)).
- Mature surfaces (Figure 2.14(c)) are mostly found in temperate areas and are the least karsted surface found in the humid tropics. The rockhead is extensively fissured with the carbonate blocks loose within the surrounding soils and has relief < 5 metres in height. There are many larger caves at multiple levels in the formation with dimensions typically < 5 across.
- Complex karst surfaces (Figure 2.14(d)) are the norm in tropical areas but can appear as localized zones in temperate regions. There are many large dissolution and subsidence sinkholes and more scattered collapse and buried sinkholes. The rockhead contains loose pinnacles with heights from 5 to 20 m and contains many large dissolutional fissures. Large caves can exist at many levels.
- Extreme karst surfaces (Figure 2.14(e)) exist only in the wet tropics. They have large sinkholes with soil compaction in the buried sinkholes as well as unstable pinnacles with reliefs in excess of 20 m. There are abundant

dissolution cavities and complex underground 3D caves systems with galleries and chambers that can exceed 15 m across.

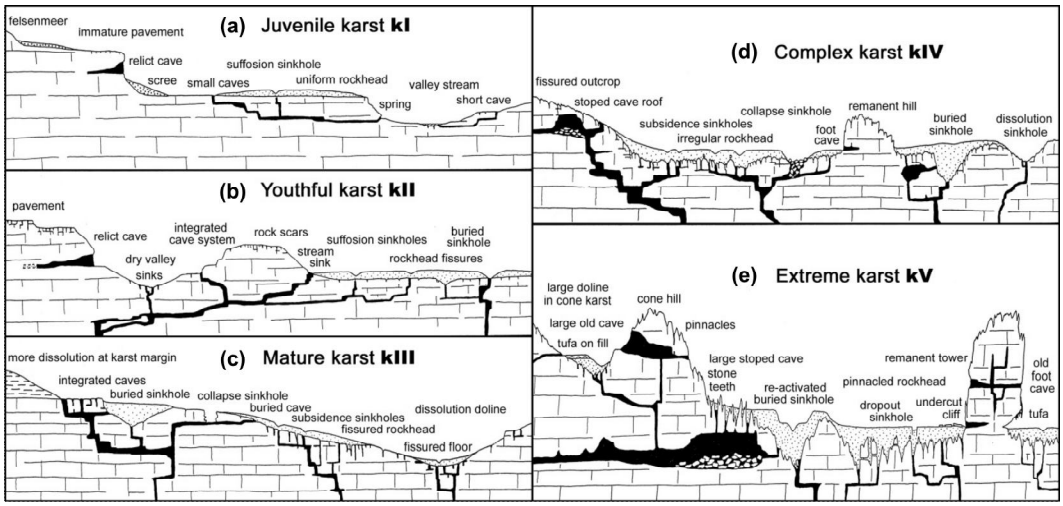

Figure 2.14: Classification of karst surfaces (rockheads) for civil engineering purposes of (a) juvenile karst, (b) youthful karst, (c) mature karst, (d) complex karst and (e) extreme karst [modified from *Waltham and Fookes,* 2003].

The SMU surface of the Grosmont is anticipated to be a 'mature-to-complex' karst surface. Evidence of reported drops in drill strings, variations in stratigraphy and depth of SMU for wellbores only a few 10's of meters and possible 40 m wide sinkholes documented in some of the vintage seismic data suggests the probably presence of caves, and sinkholes, or dry valleys.

Although the Figures 2.8 through 2.14 provide only short summary of geomorphological features and textures in karsted terrains, they do provide a sense of the structures that might be expected and the scales that can range from centimetres to kilometres. From the perspective of blind drilling into a potential subcropping carbonate reservoir such as the Grosmont, movement of the drill site laterally by only a few metres can sample a drastically different 'stratigraphy'. The Nahanni dry valleys of Figure 2.12 are good examples of this where the karst terrain surface (equivalent to the SMU surface) essentially contains vertical cliffs tens of metres high [*Brook and Ford*, 1978].

While the above discussion of modern day karst surfaces is useful, the evolution of these surfaces once they are buried is perhaps less clearly

understood. Such information likely is important, however, as it obviously affects the distribution and character of sediments that cover and enter the karst zones.

From the geophysical perspective, particularly concerning reflection seismic imaging, a few key factors need to be considered. In the context of imaging and interpreting the SMU, a large contrast in the physical properties between Paleozoic carbonates and the Mesozoic siliclastics is expected (i.e. a strong reflector and diffractor of seismic energy). There are secondary concerns are related to the 'effective' properties of the 'mixture' of the suffused and collapsed sediments within the voids of the carbonates and the potential existence of caves within the deeper carbonate body. A tertiary characteristic will be the spacing, sizes, and orientations of any joints or diffusionally opened fissures within the matrix. Such fissures are typically important to production from the reservoir and they may have a geophysical response, particularly concerning anisotropy of the formation.

2.4. Carbonate and Karst Geophysical Studies

Despite being relatively common in regions with carbonate rocks near the surface and their importance to water and hydrocarbon production, the imaging of buried karst features is poorly represented in the literature. Most of the literature deals with practical issues of delineating karst features, particularly near surface caves or potential sinkholes in reconnoitring of land suitability for development [i.e.*Waltham and Fookes*, 2003]. It is worthwhile to review some of the seismic imaging literature, the studies shown here were undertaken to resolve buried karst features, and in a sense gain experience with such surveys on general structures and variations in the physical properties that could be analogous to the SMU.

Ford and Williams [2007] and Waltham and Fookes [2003] provide a brief overview of some of the near surface techniques employed to map shallowly buried karst terrains. A summary of the main fields of application of geophysical surveying together with an indication of the most appropriate method of applications is provided in Table 2.1. The primary focus of this study is the seismic method.

Table 2.1: Geophysical methods.

Method	Measured parameter	Operative physical property
Seismic	Travel times of reflected/refracted seismic waves	Density and elastic moduli, which determine the propagation velocity of seismic waves and reflectivity of boundary interfaces.
Gravity	Spatial variations in the strength of the gravity field of the Earth	Density
Magnetic	Spatial variations in the strength of the geomagnetic field	Magnetic susceptibility and remanence
Electrical		
Resistivity	Earth resistance	Electrical conductivity
Induced polarization	Polarization voltages or frequency-dependent ground resistance	Electrical capacitance
Self-potential	Electrical potentials	Electrical conductivity
Electromagnetic	Response to electromagnetic raditation	Electrical conductivity and inductance
Radar (GPR)	Travel times of reflected radar pulses	Dielectric constant

Seismic methods of refraction [*Hiltunen and Cramer*, 2008; *Hiltunen et al.*, 2007], surface wave [*H D Harrison and Hiltunen*, 2003] and reflection [*Evans et al.*, 1994], are principally sensitive to the elastic moduli and density of the different rocks. Table 2.2 provides a summary of what one might expected for the different types of minerals related to the geology of the Grosmont of which calcite and dolomite are shown to have denser and much higher elastic moduli than quartz and clays (kaolinite and smectite). This large difference between in physical properties between carbonates (calcite and dolomite) and silicates (quartz and clays) is the primary driver for reflectivity at the SMU boundary.

Reflection seismic profiling often offers the only method to examine deeper paleokarsts as most of the near surface techniques have shown to be ineffective, and some of this work is worth reviewing. The images provided in many of these earlier studies have important lessons for seismic interpretation of karst features and the discussion mostly focuses on these aspects. Examples are

taken from land and marine studies from the U.S.A., the Barents Sea, and Indonesia.

Table 2.2: Physical properties of carbonate and associated minerals.

Mineral	Density kg/m^3	Bulk Modulus GPa	Shear Modulus GPa	VP/VS ratio	P wave velocity m/s	S wave velocity m/s
Calcite †	2712	73.3	32.0	1.90	6539	3435
Dolomite †	2795	94.9	45.7	1.85	7467	4044
Anhydrite †	2963	54.8	29.3	1.79	5628	3145
Aragonite ♦	2920	45.0	52.0	1.48	6257	4219
Quartz †	2648	37.8	44.3	1.47	6048	4090
Kaolinite ◈ (well crystallized)	2444	47.9	19.7	1.94	5509	2839
Smectite ◈ (Na-rich montmorillonite)	2598	34.7	20.3	1.76	4876	2746

† Bass [1995]
♦ Ellis et al. [1988]
◈ Wang et al. [2001]

To out knowledge, the earliest work on this topic arose from the early Industry-AOSTRA Grosmont project [*D. R. Schmitt*, 2010] where a series of seismic tests and surveys were carried out from 1980 to 1986 in the vicinity of a number of pilot projects to aid in the planning of bitumen production from the Grosmont Formation. Many of these projects were frustrated by 'heterogeneity' of the Grosmont Formation due to drilling into what appear to be sediment filled karst features that complicated production. It was not until nearly the project end that the rapidly improving geophysical methods were used to actually site a well location. By the final experiments in 1986, quite high resolution seismic images were obtained such that workers were able to identify what they referred to as 'sinkholes' as small as 40 m in diameter [i.e. *G. Carrington*, 1986a; *Tesanovic*, 1985]. Unfortunately, all of their reports remain confidential though some of their seismic data and interpretation was released for a written review in Chapter 4.

Contemporaneous seismic measurements of karstification with the AOSTRA project was also described by Steeples et al. [1986] and Steeples et al. [1984] who carried out seismic reflection profiling near Interstate I-70 in Kansas as part of a project to locate potential sinkhole hazards. At the time, sinkholes were being actively formed by dissolution of salt layers at a depth of greater than

300 m by inappropriate reinjection of produced brines. This inadvertent removal of material resulted in subsidence in all the overlying formations with both slowly lowering sections (along the highway) and even catastrophic sinkhole formation. As such, safety concerns motivated the study to see if such features could be imaged prior to such failure occurring on the highway. The scale of such subsidence reaches as much as 45 m in some locations with the production of

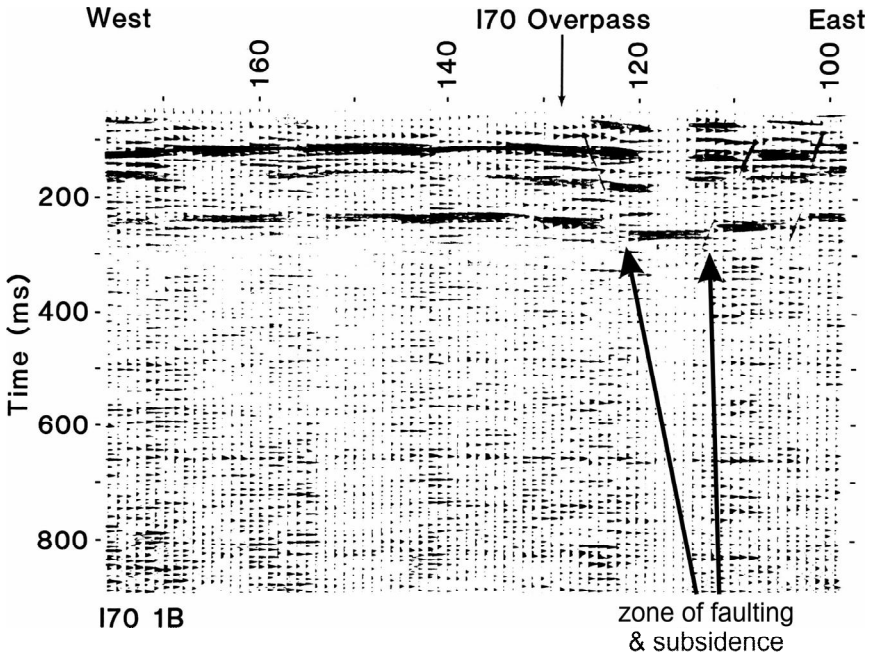

Figure 2.15: Mapping of subsidence zone at a depth of 300 meters near interstate I-70 [modified from *Steeples et al.*, 1986].

buried graben-like features. While the geological situation is not directly karst, the structures involved are of similar depths and magnitudes as are found in the SMU. Although these authors had only crude instrumentation even relative to the Grosmont efforts, their seismic sections show some interesting features (Figure 2.15). Their imaging was assisted because of a series of strong reflecting events and these show the development of faults and significant subsidence in the immediate vicinity of the highway.

More recent mapping of karst features were presented with studies coming from the Finnmark Platform, a large Late Paleozoic shelf that stretched from the Sverdrup Basin in Canada's Arctic through the Norwegian Barents Sea to Arctic

Russia. The platform was the northern margin of Pangea that dipped to the north and steepened with outboard distance, not unlike the structure of the Grosmont Formation. The Barents Sea, too, was subject to periods of uplift and sub-aerial exposure, which promoted development of karsts in the upper part of the Gipsdalen Group, Late Paleozoic age, in the Eastern Finnmark Platform in the Barents Sea. Rafaelsen et al. [2008] were able to show convincing evidence of doline development in their seismic images in Figure 2.16. Similarly, the images published by Colpaert et al. [2007] of karsting were particularly interesting and may be most relevant to the Grosmont situation. Their final map Figure 2.17, arrived at from a trained neural network data set that incorporated a number of different seismic attributes, separates the region into non-karsted (yellow-white) and karsted (red) zones. The image shows numerous isolated doline-like features as well as sets of dolines that appear to follow one another (refer to Figure 2.9 for modern equivalents). These patters of dolines may merge into larger drainage systems that are not unlike the modern day equivalents of Figures 2.9 and 2.10.

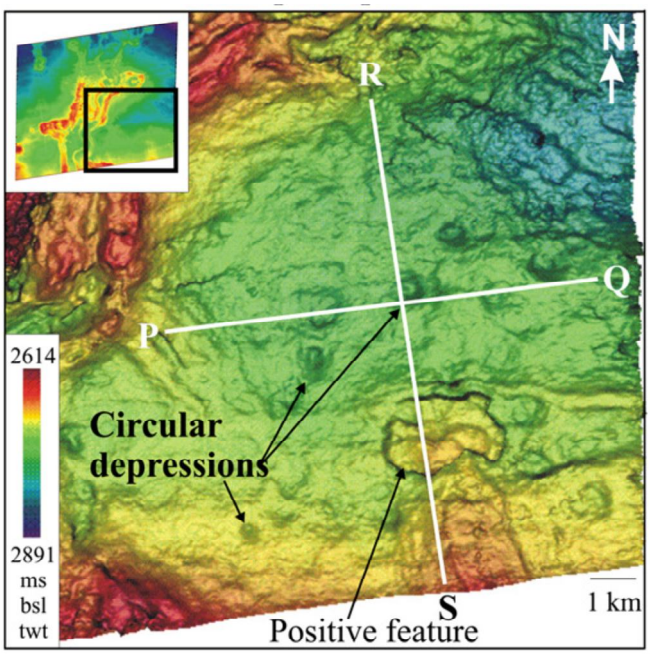

Figure 2.16: Time structure map at the Top Evaporites horizon displaying cicular depressions interpreted as sinkholes [reproduced from *Rafaelsen et al.*, 2008].

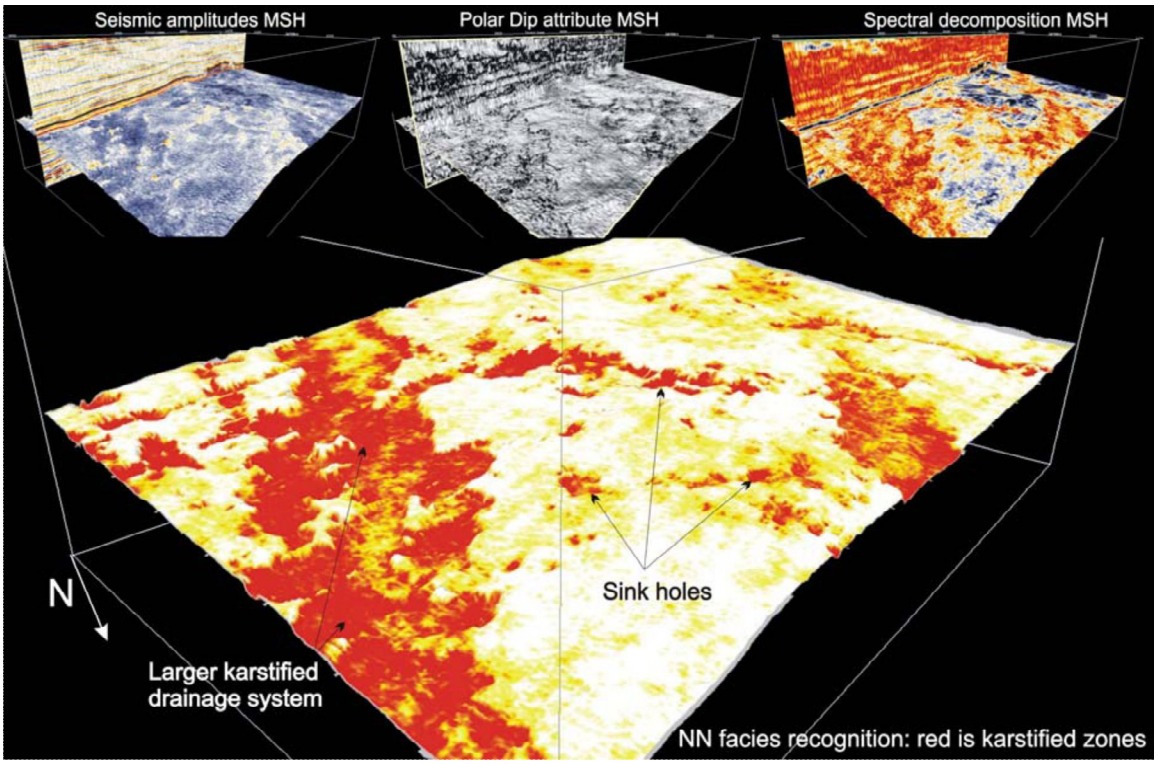

Figure 2.17: Result of an analysis of a 3D seismic data over Late Paleozoic carbonates in the Eastern Finnmark Platform in the Barnet sea. The cutaway views of the 3D seismic data volume at the top of the figure display the data using different attributes of seismic amplitude, dip attribute, and spectral decomposition of the base of the Artinskian horizon. The larger image is the result of a neural network analysis that combined the above attributes to arrive at a map on non karsted (white-yellow) and karsted (red) zones [reproduced from *Colpaert et al.*, 2007].

The above represents a subset of the contributions in the public literature. The interest in seismic detection of buried paleokarst zones appears to have been growing as indicated by the number of recent abstracts presented at applied geophysics meetings. These include studies of the use of various volume attributes to identify paleokarsts in the Ordos Basin, China [*Duan et al.*, 2010], the Persian Gulf [*Farzadi and Hestharnmer*, 2007], and the Permian Basin, Texas [*Dou et al.*, 2009] to name a few.

In summary, there are a number of examples where reflection seismology has played a significant role in delineating karst features. One issue, brought up by many authors is the fact that while the karst may be evident from mapping of unconformity surfaces, data often do not give information about the internal structure of the karst zone as might be desired. The use of differing types of seismic attributes, together with artificial intelligence methods of analyses that

can be trained using well log and seismic data together [i.e. *Colpaert et al.*, 2007], may have many advantages in extracting information about structure and possibly material properties.

One final comment here is that, while many of the images derived from seismic data are quite good, these are often built from marine data that is often much easier to extract good quality seismic data than those built from land data. While many modern data sets have been collected over Grosmont subcropping edge, these data are highly proprietary and are not available for examination. We will endeavour in the following chapters, using vintage seismic reflection lines, to map the topography of the SMU and attempt to make inferences about it.

2.5. Summary

The buried carbonate rock of the Grosmont formation in north-eastern Alberta is conjectured to have possible dissolution features such as dolines, caves, karst valleys, and epikarsts present near the SMU boundary. Evidence from drilling and pervious seismic work is suggestive that this eroded surface of the Grosmont platform may reflect a 'mature-to-complex' karst surface and thus mapping of such a surface buried approximately 300 m is best suited for 3D seismic imaging. Modern techniques to map karst features with seismic data has shown to work great when appropriately applied. Overall the mapping karst features is expect to be achievable at local scale. Mapping of such a buried surface was conclude The use of n summary, it is not only possible to detected the acoustic reflection of the SMU but in fact we may observe further evidence to support karstification along the subcrop edge of the grosmont formation.

Chapter 3 The Vintage Seismic Surveys and Well Log Data

3.1. Overview

This chapter provides a brief historical account of the vintage seismic data obtained for this project. To keep in accord to confidentiality agreements, the original names and coordinate locations of the seismic lines will not be shown. Figure 3.1 shows a map of the relative locations of seismic survey series A through E. Table 3.1 below summarizes the specific acquisition parameters deployed for each survey. Acquisition information was supplied supplementary with the field records.

Concerns with the initial data quality and incomplete interpretation have led to the data being reprocessed at this time in an attempt to consolidate all the independent surveys and improve their resolution of the SubMannville unconformity (SMU) surface.

A short summary of the local well log data obtained in the area will also be covered. There many of borehole locations found throughout the area but unfortunately most did not have the appropriate well log data of sonic and density logs for the creation of synthetic seismic traces and other such seismic related uses. Furthermore, depths of the boreholes on the majority were shallow (< 300 m) with only a few extending deep enough to penetrate through the Grosmont Formation.

Table 3.1: Acquisition parameters deployed by the vintage seismic surveys.

Survey	Year Acquired	Total Distance	Survey Type	Source	Source Configuration	Source Depth	Source Interval	Geophone	Geophone Group Configuration	Group Interval	Maximum Offset	Fold	Recording Parameters	Recording Filters (Hz)
Series A	January 1984	103.64 km	2-D Digital	Dynamite	1 x 0.25 kg	15 m	80 m	Mark L-25D 30 Hz	9 inline at 4 m spacing	16 m	960 m	12	120 traces @ 2 ms for 2 sec	Low-Out High-128
Series B	March 1981	19.93 km	2-D Digital	Dynamite	1 X 1 kg	18 m	45 m	L-15 14 Hz	6 clumped	22.5 m	540 m	12	48 traces @ 1 ms for 2 sec	Low-Out High-256
Series C	February 1984	35.99 km	2-D Digital	Dynamite	1 X 0.5 kg	20 m	40 m	Mark L-28 14 Hz	12 inline at 1.8 m spacing	10 m	480 m	12	96 traces @ 2 ms for 2 sec	Low-12 High-180
Series D	March 1985	3.21 km	Full 3-D Digital	P-shooter	20 drops	Surface	40 m	L-28D 14Hz	9 inline over 20 m	20 m	NA	10	120 traces @2 ms for 2 sec.	Low 12.5 High 125
Series E	February 1986	17.14 km	2-D Digital	Dynamite	3 X 0.1 kg over 20 m	5 m	20 m	Mark OYO 14 Hz	12 inline over 10 m	10 m	Max 250 m	12	48 traces @ 1 ms For 2 sec	Low-Out High 256

3.2. Regional Seismic Surveys

3.2.1. Survey Series A - January 1984

To our knowledge, the bulk of the publicly available literature describing the Grosmont Platform and formations rely entirely on well logs and core. This is partly because there have been no basin wide seismic studies through northern Alberta across the platform (as has been done further to the south with the Lithoprobe Alberta basement transects). Most of the commercially available data in the area also consists of smaller surveys. However, two EW profiles of ~40 km or more length that were acquired in the 1980's have been obtained for this study under restrictions that only final processed images may be displayed with approximate positions. The source of these data are unknown but they were never associated with the original Alberta Oil Sands Technology and Research Authority (AOSTRA) / Industry project in the 1980's that acquired the rest of the high resolution seismic surveys for this project. The approximate locations of the north and south regional lines of survey series A are shown in the regional map of Figure 3.1(a).

3.3. High-Resolution Seismic Surveys

Four separate high-resolution seismic surveys of series B, C, D and E (see map in Figure 3.1(b)) were obtained for this study near the southeast vicinity of series A regional seismic lines. These high resolution surveys at the time of acqusitionin the early to mid 1980's were unique, closely spaced receivers and sources have not been employed until more recently (i.e. Schmitt, 1999).

To the varying degree, some of these high-resolution seismic surveys were processed and interpretation for the topography of the top of the SMU (often called the top of Grosmont D in the area). These maps were developed from the seismic base map in Carrington [1986] and have been discussed to varying levels of detail in reports produced for AOSTRA that in many cases provided the majority of the funding for acquisition and processing of the seismic data. Abrupt termination of the AOSTRA project in the mid 1980's left much of the seismic

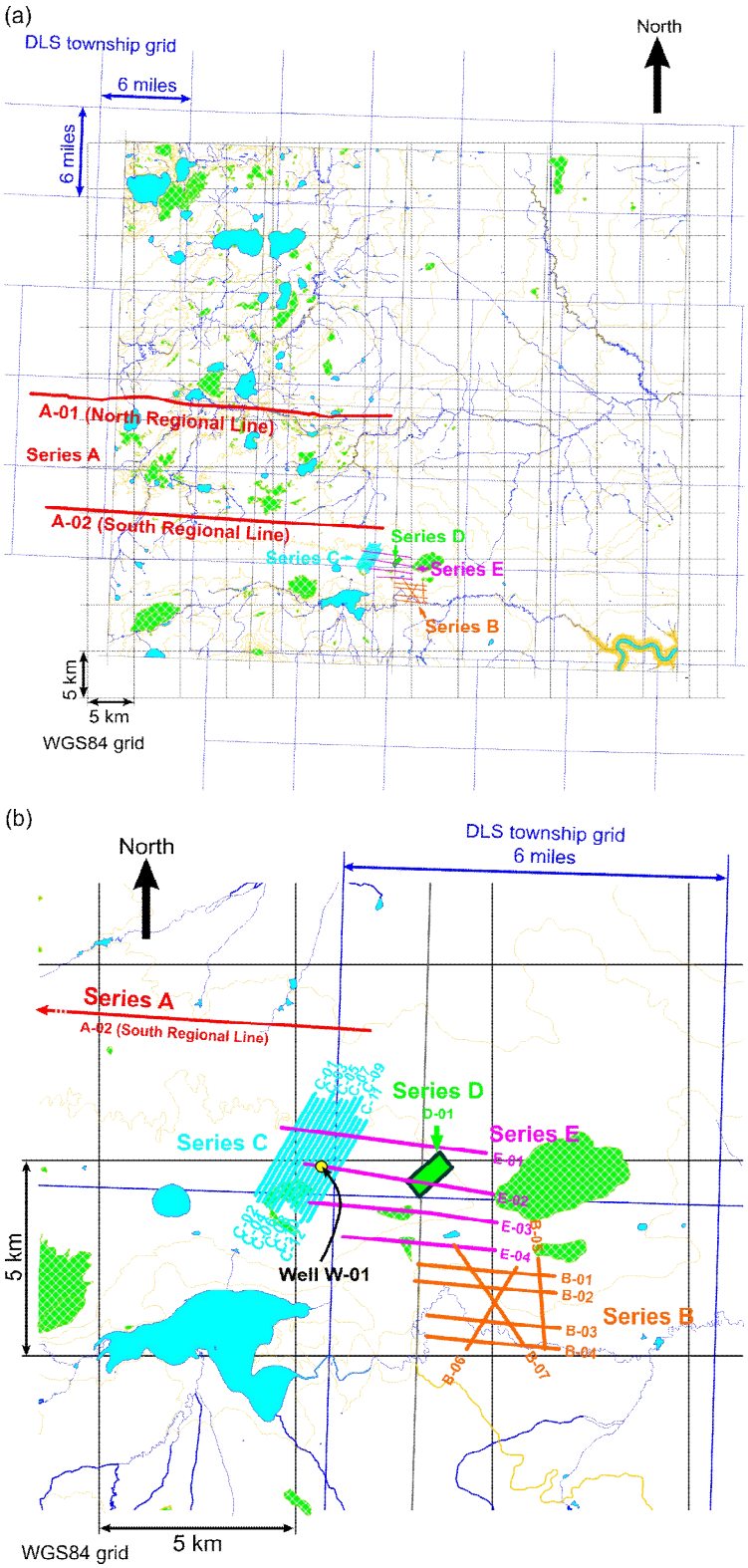

Figure 3.1: Map showing the locations of the seismic data obtained for this project where (a) is the regional map of all the seismic data and (b) the local area map highlighting Series B, C, D and E data sets. The yellow dot in (b) denotes the location of a well with VSP data.

data in an incomplete form and no unifying interpretation of the local area.

A vertical seismic profile was also acquired in one well site shown by the yellow dot in on the map of Figure 3.1(b).

Most of the results of these surveys are presented in the later UNOCAL reports of AOSTRA to varying degrees of detail. Unfortunately, it does not appear that there was sufficient time for those workers to fully analyze most of the data sets of this project as the reports mostly show, at best, a few images and no interpretation or lineage to the existing well logs. While there are some interpretive maps provided, there is no rationale for the various interpretations given. The earlier and more extensive report by Tesanovic [1984] is the exception to this rule although here too the rationale behind the interpretations are not provided.

Here we review the various high-resolution seismic surveys obtained for this project.

3.3.1. Survey Series B - March 1981

Survey series B data consist of seven short 3 to 4 km long profiles (see map Figure 3.1(b)). This data was shot with closer shot and receiver spacing than would have been employed in standard industry practice at the time in order to better image the unconformity Carrington [1986b] indicated that these data had better quality than pervious studies in the area likely due to the increased fold and perhaps to improved data processing. The example from his report of Figure 3.2, a stacked section from series B data, did show features in the Cretaceous sediments that immediately overly the SMU. Detail was also seen in the underlying Paleozoic sediments including features that could be interpreted as ‘diffractions’ that would be indicative of sharp changes in structure: this is consistent but does not prove the existence of dolines or karst collapse zones. This diffraction appears substantially beneath (~ 50 ms) the unconformity surface and may point to the existence of deeper karsting (cave?) features.

The reports seem to indicate that a major goal of the series B data was to allow for discrimination of the Upper Grosmont 2 from Upper Grosmont 3

(currently Grosmont C and Grosmont D, respectively). This does not seem to have been accomplished in these surveys. However, given that almost no appropriate well logs (sonic and density) were acquired in the many wells drilled, these authors would have had a difficult time attempting to properly model and even to tie the geology to the actual seismic response (this lack of critical information is noted in later reports, e.g. Tesanovic [1984], and even applies to the modern day).

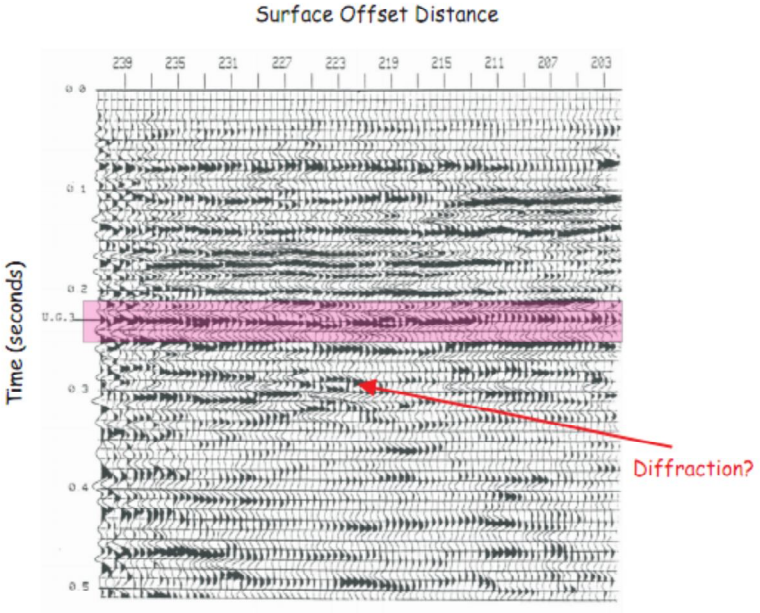

Figure 3.2: A portion of seismic section from survey B where the highlighted magenta area was interpreted as the waveform arrival of the SMU with a noted diffraction beneath the unconformity [modified from *G. Carrington*, 1986b].

3.3.2. Survey Series C - February 1984

Survey series C seismic survey consisted of 12 closely spaced parallel profiles spaced only 110 m apart was carried out over an AOSTRA pilot site in early 1984 in advance of potential development (see map Figure 3.1(b)). This is somewhat unique survey appears to have attempted '3D' coverage by having the 2D profiles in close proximity to one another. While this is definitely an improvement over more sparsely placed seismic 2D profiles, such data is still limited in that it cannot account properly for seismic diffractions and reflections that occur outside the plane of the profile. However, at the time 3D imaging was

still struggling to be accepted as a useful tool. An example of a portion of one of the profiles from this survey is given in Figure 3.3.

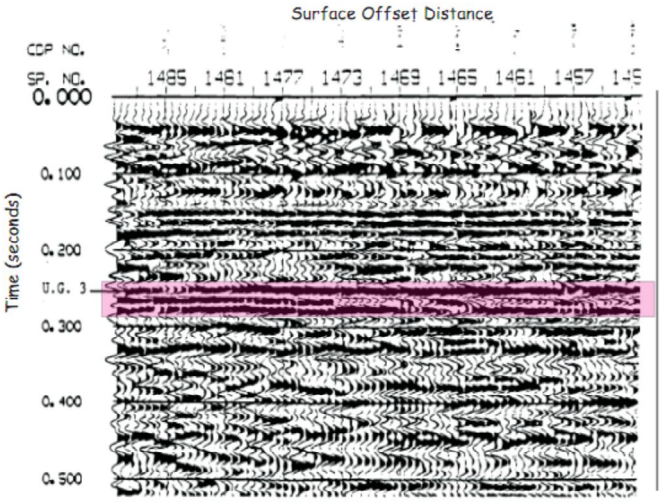

Figure 3.3: A portion of seismic section from survey B where the higlighted area in magenta is the interpreted waveform arrival of the SUM [modified from *G. Carrington*, 1986b].

This data received the most attention out of the high-resolution seismic surveys of this project. A report by Tesanovic [1984] whose 'Location Evaluation Map' (Figure 3.4) provided his analysis towards the risk of karstification over the area. Although not indicated in his reports, it was likely that his interpretations was a integration of both lower seismic amplitude and travel times sags associated with the top of the unconformity to assess high risk areas. He provides the following qualitative criteria for his assessment of the 'Location Evaluation Map' Figure 3.4:

- *Low Risk Areas (Green)*: the seismic data displays high reflective amplitudes without any time sag. This designation is qualified, however, by indicating that the author would not discount the potential existence of sinkholes smaller than 100 m across.
- *Very High Risk Areas (Red):* these are presumed to be large sinkholes or depressions at the SMU.
- *High Risk (Yellow):* Are 'usually' in the vicinity of sinkholes and have low amplitudes

- *Poor Data Quality (Light Green):* The Grosmont reflectors completely disappear for unknown reasons.[2]

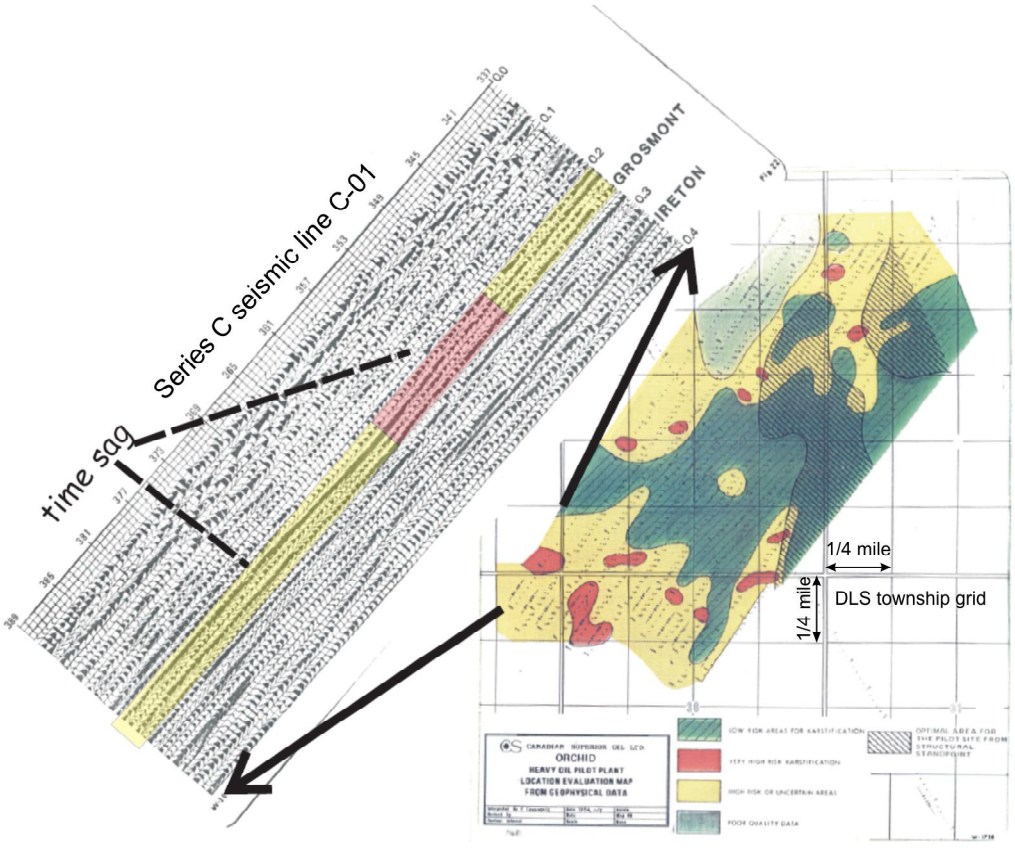

Figure 3.4: 'Location Evalutaion Map' created by Tesanovic [1984] and a portion of the originally processed seismic data where yellow and red regions highlight the SMU and match the color coding on the location evaluation map.

In addition to the Location Evaluation Map, Figure 3.4 shows the SW portion of the originally processed seismic line C-01; the arrows here indicate the extend of the seismic section on the map. The transparent yellow and red colors along the Grosmont reflection package at ~250 ms two-way time are delineated according to the same colors seen in the map. This comparison of the profile to the map does not assist in the understanding of the application of the various risk criteria. For example, a time sag of the reflectors, that should be indicative of a '*Very High Risk Area'* is apparent in the profile between common midpoint

[2] The current reprocessing of the data to be provided in the following chapter does show a reflector but with complex topography.

(CMP) numbers 353 to 373 while the map shows this only from CMP 349 to 361. This suggests that the maps shown are already highly interpreted products and, without having the author's direct insight, likely cannot be replicated.

The time sags of the SMU were reported as much as 17 ms over the area of survey series C (Figure 3.5). Assuming the overlying Cretaceous sediments were on the order of 2500 m/s, this 17 ms difference in the time surface would correlate to topography variations up to 20 m.

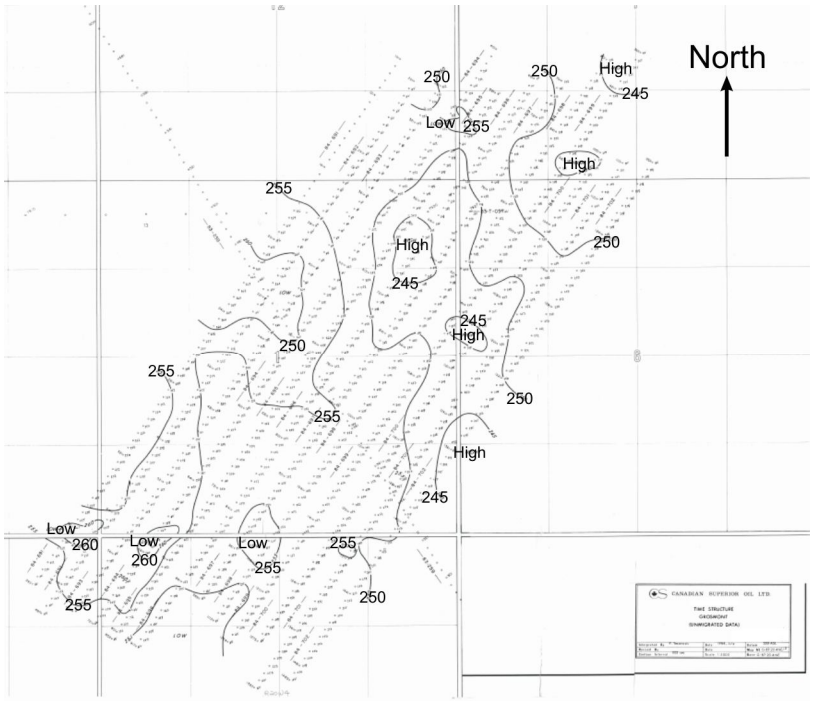

Figure 3.5: Map of two-way seismic reflection time to the SMU [modified from *Tesanovic*, 1984].

3.3.3. Survey Series D - March 1985

Survey series D is a small full 3D seismic survey obtained over an area approximately 400 m X 1000m (see map Figure 3.1(b) for location) was an interesting experiment in seismic acquisition. The measurements were doubly unique because at the time 3D seismic surveying was still in its infancy and had not been accepted as the primary method it is today, but also because the short source and receiver spacing employed would still be rare in industrial practice.

The short spacing between the sources and receivers as well as the small offsets show that its authors attempted to enhance the imaging of the unconformity surface [Appendix C by Carrington in McGillivray et al. [1987]]. Substantial efforts went into the planning of this survey with various proposals and consultants opinions provided [*CGG*, 1983].

This was the only full survey to employ a surface seismic source; all others had previously used buried dynamite. This source was called a 'pea shooter' [*Omnes and Robert*, 1982] that is classified as a type of weight drop system in which seismic waves are generated by accelerating a mass onto a plate on the surface. Such sources have certain cost advantages in that they do not require that holes be drilled as needed for dynamite and that they are easily moved and operated. A disadvantage of such sources, however, is that that the quality of the seismic pulse put into the ground is much degraded (lower frequency and bandwidth) relative to a buried dynamite explosion. This is particularly true in marshy areas that exist at the site of the 3D survey. Despite this, reasonable quality data was collected with an example of one line given in Figure 3.6. Carrington [1986] comments that the quality was '*no better or no worse*' than the nearby surveys and says any deficiencies in the data set are likely due to the type of seismic source employed.

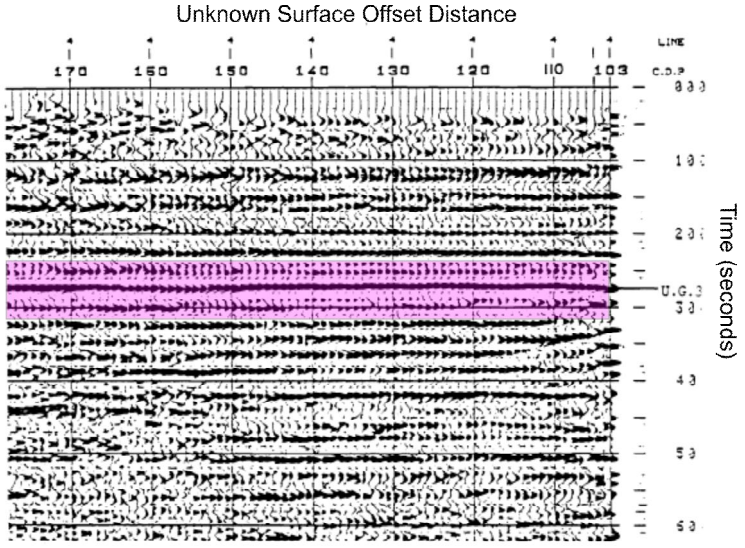

Figure 3.6: A portion of an arbitrary seismic section within the 3D survey of survey series D where the highlighted area in magenta was the interpreted waveform arrival of the SMU [modified from *McGillivray et al.*, 1987].

A time structure map of the unconformity surface in Figure 3.7 from Howell [1987] also shows some variation but much less than at McLean or Orchid with times ranging from 263 ms to 269 ms. This time difference would result in topographic variations safely less than 10 m. This map, too, has been interpreted in the same manner with different areas denoted as hill, karst, plain, and water shelf. It is not clear how these assessments are made particularly as it the time surface in is relatively uniform. There is also one additional caveat that must be added to these maps: the seismic data was collected sometime after injection and production tests had been run in borehole denoted as the black dot in the map.

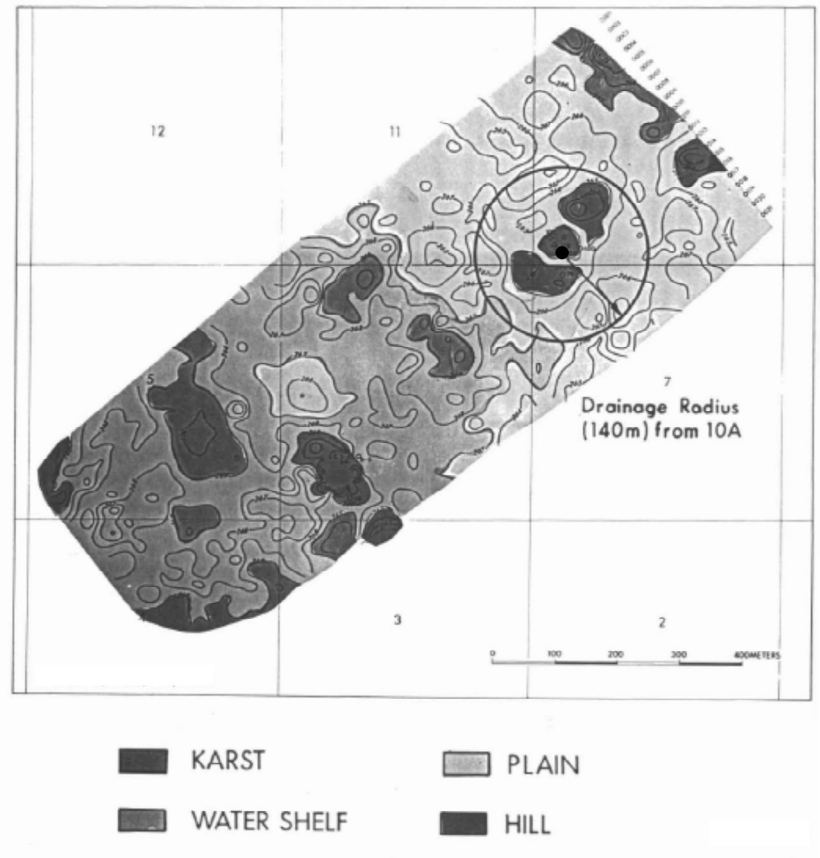

Figure 3.7: Map of SMU paleostructure superimposed on the time structure of the unconformity [modified from *Howell,* 1987]. The black dot and circle indicate the location of a pre-existing pilot well and predicted drainage.

As noted in final reports of Carrington [1986b] and McGillivray [1987] there was insufficient time for this data set to be properly analyzed and at that

time they hoped to see future reports on its use and utility for such shallow imaging.

3.3.4. Survey Series E - February 1986

A series of five final high resolution 2D profiles for survey series E were acquired to 'tie' all of the earlier seismic lines together. Of these, only 4 of the 5 lines were obtained for this study (see Figure 3.1(b)). The acquisition parameters were developed with the results of prior experience and testing [*G. Carrington*, 1986a; b]; triple shots each of 100 g of dynamite buried at 5 m depth provided seismic energy to the geophones. Nine geophones were 'clumped' at each receiver station to increase the signal to noise, and the stations were spaced only 10 m apart. This was deemed the highest quality data of all of the surveys and an example of one of the processed lines in Figure 3.8 displays an excellent seismic section. Carrington [1986b] claims that karsts as small as 40 m across could be imaged and further goes on to indicate that this seismic data allows discrimination of the Grosmont C from the Grosmont D. Unfortunately, none of the reports show any of these zones explicitly. As noted earlier, even with the increased resolution of these 1986 data, it is not clear how the C and D horizons can individually found.

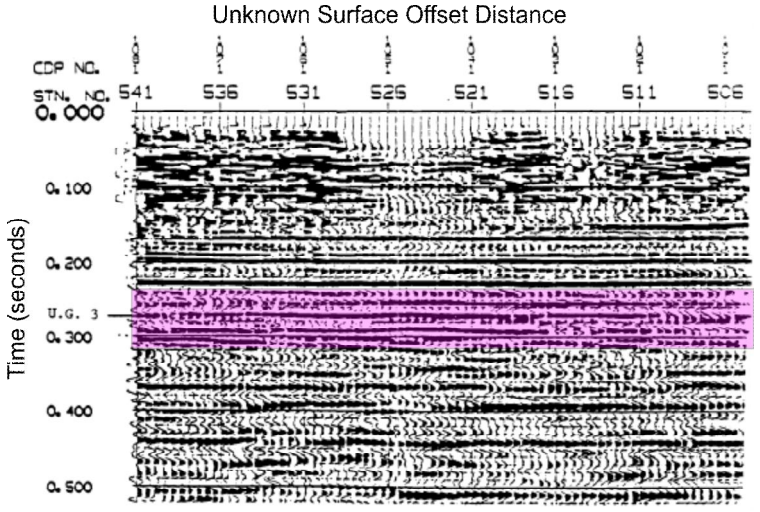

Figure 3.8: A portion of seismic section from survey series E data where the highlighted area in magenta was the interpreted waveform arrival of the SMU [modified from *G. Carrington,* 1986b].

It does not appear that these data were ever employed for their final use in tying the various surveys together and, to our knowledge, no interpretation of them has been found in the existing records although some brief discussion of this issue does appear in some of the project technical meetings. The fact that all of the different surveys had been independently acquired and processed may have prevented this data being used fully, and a full reprocessing of all of the data simultaneously would likely have been necessary to integrate the results.

3.4. Well Log Data

All of the well log information available to us over the area was obtained via the IHS Accumap database. All 117 wells in the immediate vicinity of the two regional and the local high-resolution seismic lines that were available on this data base were obtained with their relative locations as shown in Figure 3.9. Unfortunately, most of these wells were drilled for shallow gas production and often only just touch the SMU and this reduced the number of wells available to tell us about deeper structures. Further, only a very small fraction of the wells had geophysical sonic and density logs that are necessary for the proper calculation of 'synthetic seismograms'. Of such wells, well W-01 (shown in Figure 3.1(b)) also had a vertical seismic profile (VSP) run along its length. Results from the VSP data were used to further calibrate the seismic response of the geological formations in this area. Details of VSP acquisition, processing, and interpretation are beyond the scope of this report, further details can be found for example in the book by Hardage [2000].

Of the problem noted in attempts to calibrate the seismic response to the geological formations in this area was the lack of sonic and density logs; the reason for this likely being the complications with lost circulation and tar within the wells drilled. This problem appears to persist to the present day as there are very few logs that contain sonic measurements, and of those that do, the velocities are primarily measured within the only in the Paleozoic.

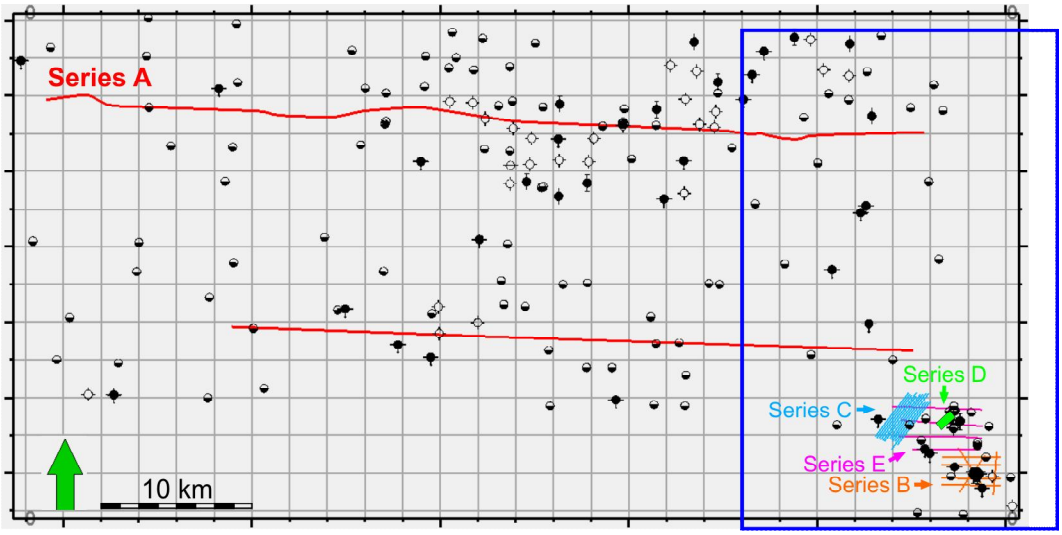

Figure 3.9: Map view of the seismic data with the 117 wells investigated in the area. The blue rectangle indicates the area where the geological model of Figure 3.10 was constructed.

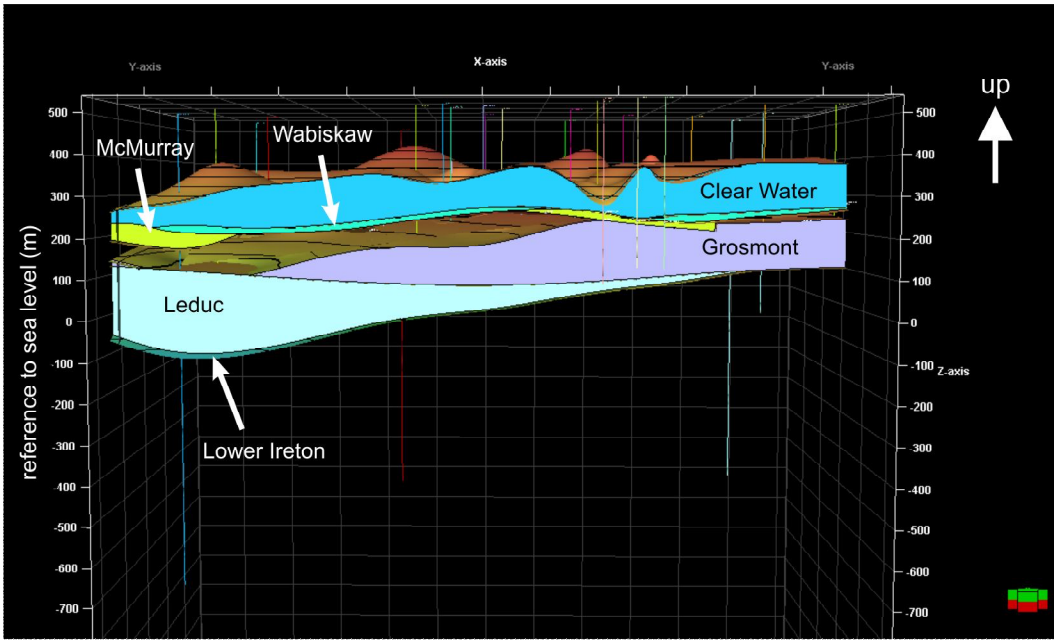

Figure 3.10: Perspective view from the south into the geological model constructed from available well data (courtesy of Mr. Mohamed Fatmed) in area indicated by the blue square in Figure 3.9. Note the model show that the bulk of wells (vertical pipes) only penetrate to the SMU.

One image from the geological model produced from the picking formation tops from available well logs, Figure 3.10 shows the variations in the various formations over the regional study area. Most wells had available gamma ray logs for the identification of formation tops. While such models are best viewed in digital form, this image does show some interesting aspects concerning

the stratigraphy in the area. For example, Figure 3.10 shows that the McMurray Formation is absent in some locations; and this may be due to topographic high points of the SMU that may have existed during Mannville time deposition. One would expect such topographic anomalies to influence the deposition of the fluvial-estuarine McMurray Formation.

Such features are hinted at in Figure 3.10, and have been incorporated into the modified regional stratigraphy chart of Figure 2.2 that attempts to represent features including buried Quaternary valleys that can cut into the SMU, relict knobs of Devonian carbonate elevating the SMU, Leduc reefs, and epikarst immediately beneath the SMU.

3.5. Summary

The historical account of analysis and interpretation of the vintage seismic data acquired for this study was reported as vague and incomplete. Re-processing of the entire data set, even the handful of surveys that were fully processed back in the 1980's, offers the advantage of modern processing schemes that may have the ability to enhance the data quality and allow some uniformity between the data for the eventual merging of the individual surveys.

Most boreholes drilled in the area were shallow in nature with only a select few penetrating beyond the SMU. Unfortunately appropriate borehole data of sonic and density logs shall be used to generate synthetic seismograms in the project area were sparse. Most wells had other conventional logs such as gamma ray for the identification of formation tops. One well in the area had VSP data and should prove instrumental during the interpretation phase of this study.

The geological model built from the well log data shows that there are significant geological lows and high of the SMU. Deposition of McMurray sediments was also suggested to be controlled by the SMU topogarphy.

Chapter 4 Seismic Processing

4.1. Overview

The seismic data for each survey were received on media disk as copies of original acquisition files. These files included the SEGB digitally formatted shot records, a geometry text file, and digitally scanned images of hand written field reports of chaining, drilling, surveying, and observer report. This media package was typical of archived, unprocessed seismic data acquired in the 1980's. However, this means that there was a tremendous amount of work involved in data preparation such as re-formatting, organizing, editing, and merging of field geometry before the application of processing workflows.

Once the data was in a ready-to-use format, several processing workflows were investigated and scrutinized to optimize on signal preservation and enhancement in the stacked images of the seismic data. The processing workflow outlined in Figure 4.1 was ultimately employed to process the vintage seismic data. The seismic data processing package VISTA™ provided for research purposes courtesy of GEDCO, Calgary was used for all the data processing.

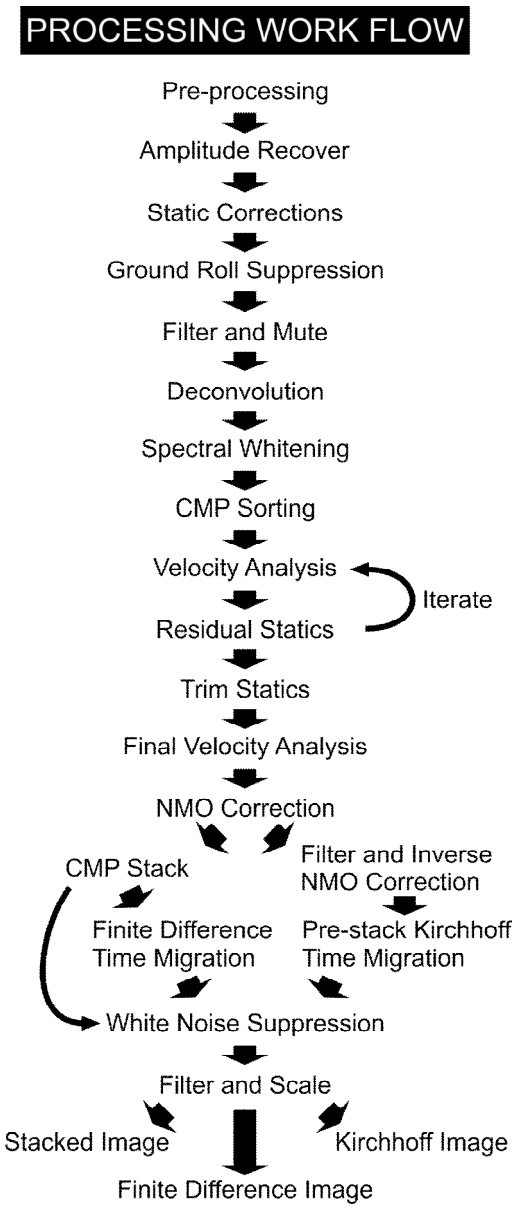

Figure 4.1: Illustration of the applied seismic processing workflow used for this study.

4.2. Pre-Processing

4.2.1. Demultiplexing and Reformatting

The first step taken in seismic data processing was the demultiplexing and transcription of the original SEG-B data files into SEG-Y format. The process of demultiplexing rearranges the time samples of a shot record, taking the matrix transpose, from scan sequential into trace sequential format. The time samples

were now chronologically arranged with respects to traces. This process was performed with the aid of Vista Tape 9.00® software package.

SEGY format is a better digital storage form of data that can be readily processed by main algorithms. Another main advantage is an expanded trace header. Trace headers stores important information uniquely relevant to the trace such as number of samples, sample rate, format code, field station number, field record number, channel number, trace sequential number, elevation, and x-y coordinates.

4.2.2. File Edits

During the acquisition of the seismic data for this study, defective shot records and tests records were intermittently recorded with good shot records. Therefore, the next step was to screen the data on file-to-file basis to remove all unnecessary records while keeping only those that would provide acceptable data.

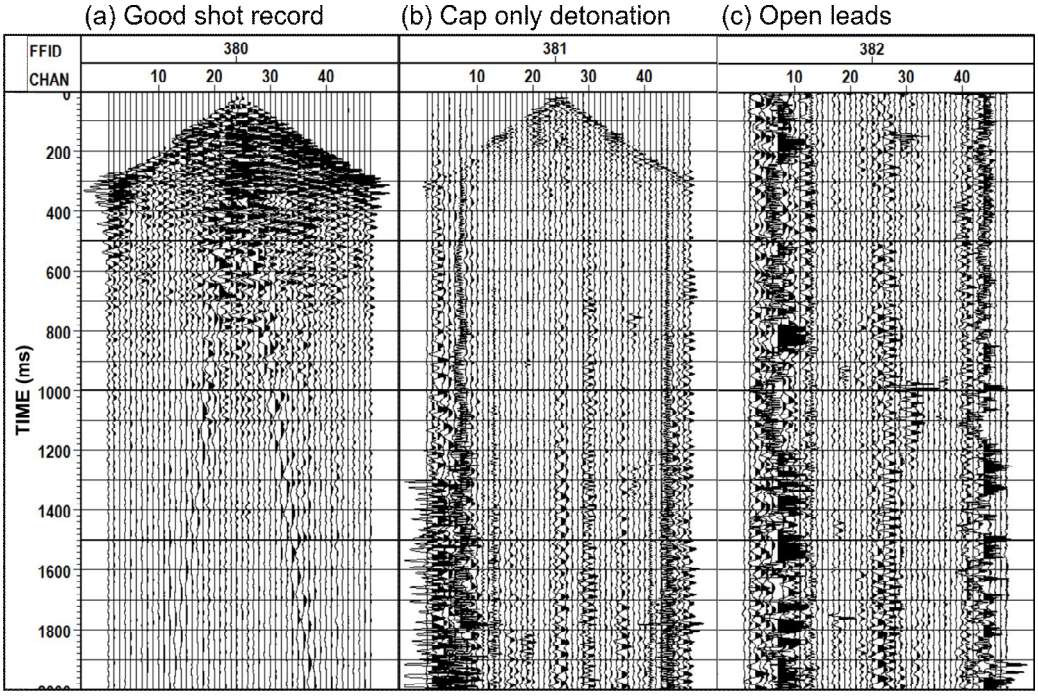

Figure 4.2: An example of three shot records from seismic line B-04 illustrating (a) good shot record, (b) cap only detonation and (c) open leads.

Test records and defective shot records, such as cap only firing, open leads, miss-trigger, and other such logistical and equipment issues, were apparent

in the field data (i.e. Figure 4.2). These records were screened and removed with some difficulty, as not all were properly document.

After defective shot records and test files were pulled from the data, the rest of the shot records were loaded into Vista Seismic Processing® software for the rest of the sequential data processing of this chapter.

4.2.3. Merging of Field Geometry

Merging of field geometry with the seismic data consisted of assigning a field station number, a shot point number and positioning data to each trace of each of the seismic surveys. The merging of the field geometry with the seismic data was found to be a time intensive task. Experienced professionals note that this step is most prone to human error, thus great attention to detail was used when performing this step. The observer report served as the main linkage between acquisition geometry and digital shot records.

First was the loading of shot information of shot sequence number, shot point number, shot depth, and skid for each shot record. This was followed by the loading receiver information of field station numbers for all traces. It was extremely important to be mindful of any acquisition changes, such as wrong wraps, changes in near trace offsets, or end of line roll on and roll off, and how they would effect the standard spread configuration.

Each survey had an SEGP1 file associated with the field data. The SEGP1 file contained the geometrical locations of horizontal and vertical positioning for all stations along a survey's profile, i.e. relating to field station and shot point numbers. Most of the positioning data for the seismic surveys was compiled under universal meridian transect (UMT) coordinates of the North American Datum 1927 (NAD27) reference datum with some in North American Datum 1983 (NAD83). It was imperative that all positioning data for the Grosmont project, whether it be the seismic surveys or well log data, was unified under a common reference frame to avoid any positioning errors. The reference frame chosen the project was the World Geodetic System 1984 (WGS84) reference datum. All x and y coordinate information contained in all SEGP1 files were translated into

WGS84 reference datum of UTM zone 12N. Trace headers were then fitted with x-y coordinates and elevation information based on their shot point number and field station number.

The next step was to find the geometrical relationships between a shotpoint and the traces of a shot record. Simple calculations of source-receiver offset and mid-point locations were computed and written to trace headers.

The last objective of this section was to define common mid-point (CMP) bins along the profile to sorting traces from shot records (common shot gathers) to CMP gathers. CMP bin sizes were defined as having half the geophone group spacing for all 2-D seismic lines to meet the specified full-fold requirement of each survey [*Mayne*, 1962]. This meant that seismic line A-01 with a geophone group spacing of 22.5 m had a bin size of 11.25 m and a fold 1200%.

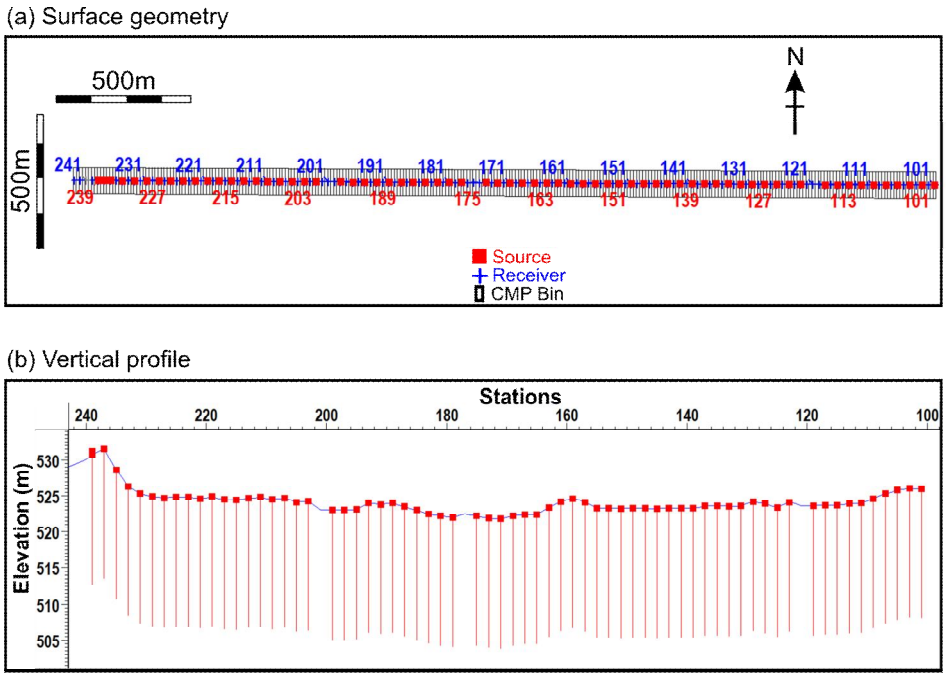

Figure 4.3: (a) Map of surface geometry and (b) vertical profile for seismic line B-01 Red lines extending below the sources in (b) indicate depth of shot from surface.

Figure 4.3 displays an example of the surface map for seismic line B-01 with displayed source, receiver and CMP bin locations. For the regional seismic lines of survey A data, crooked line binning was employed [*Nedimovi and West*, 2003] because of significant bends present in the surface geometry due obstacles

such as lakes. The fold coverage for seismic line A-01 is shown in Figure 4.4. Observe that full fold coverage is reached from CMP number 26 to 264 (i.e. stations 113 to 233 respectively). The fold tapers off at the ends of the seismic line.

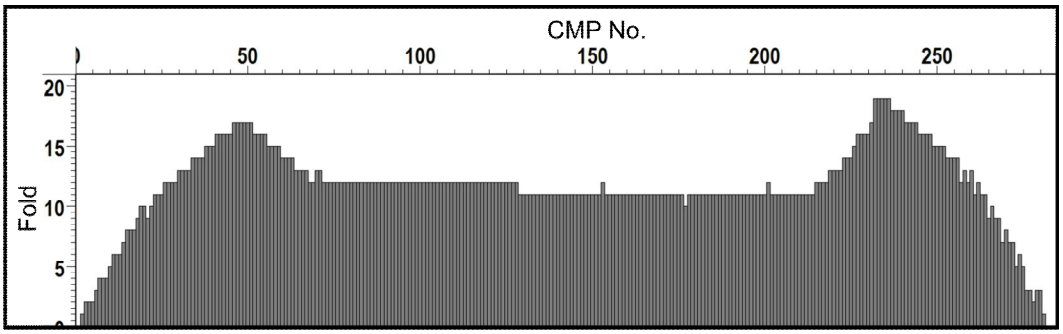

Figure 4.4: Fold chart for seismic line B-01.

4.2.4. Trace Edits

Pre-processing involves the deletion of dead and noisy traces. If not removed, they can be problematic to processing algorithms such as trace scaling, stacking, and residual static corrections. This section outlines methods used to sift through thousands of traces to seek those that were unacceptable due to dead, noise or poor recording issues.

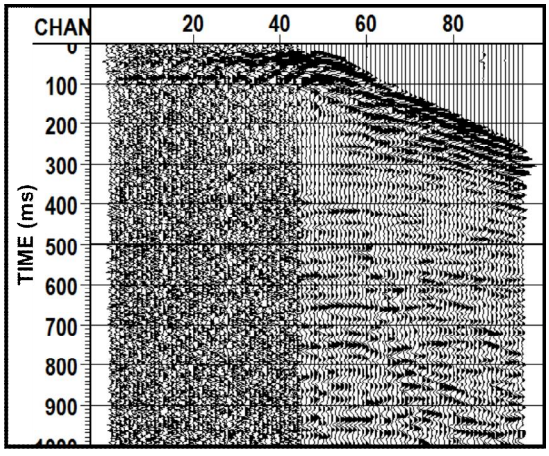

Figure 4.5: Shot record from seismic line B-06 displaying dead traces from channels 1 to 44.

A dead trace is a channel that records no seismic information either due to a receiver being disconnected or broken equipment. These types of traces only record very low amplitude random, white noise as illustrated on the left side of Figure 4.5. The observer log documented most of the dead traces found in the data and some were visually determined by viewing the shot records directly. All of these traces were deleted from the existing dataset.

Noisy traces such as those with transient glitches, and mono-frequency signals were next to be investigated. Since the data set of the entire project encompassed over 330,000 traces, cross plotting of trace attributes provided a quick means of analyzing and evaluating large amounts of data at time. These trace attributes were calculated over one second time window just below the arrival of the direct wave.

Attribute maximum frequency, the frequency with largest amplitude in the amplitude spectrum, was the first trace attribute to be analyzed. It was noticed in Figure 4.6(a) that reflection energy of survey series C had a maximum frequency predominantly ranging 20-50 Hz. This was a reasonable response given the dynamite source used in the survey and depth of time window. Traces with high maximum frequency values typically record high levels foreign signal not associated with the seismic source. Traces with high maximum frequency values above 55 Hz, in this case, were further examined in (i.e. Figure 4.6(b)) to confirm presence of noise and then removed from the dataset.

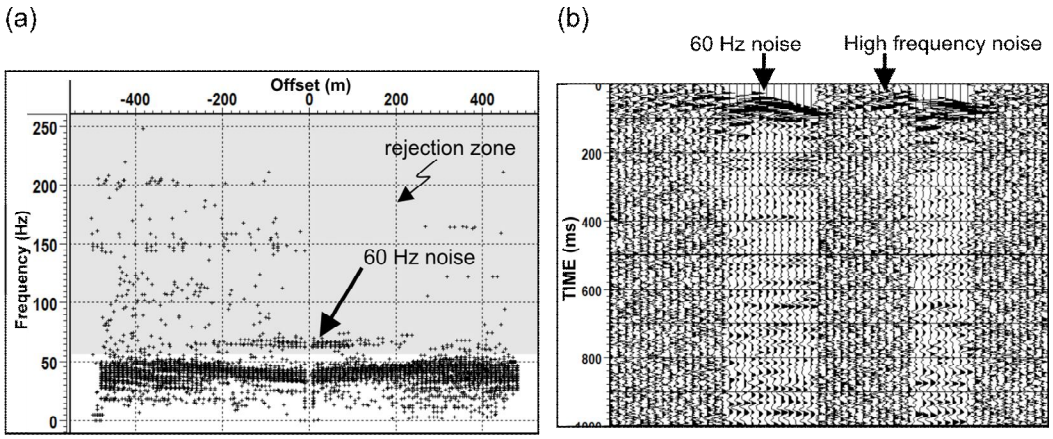

Figure 4.6: (a) Cross plot of maximum frequency versus source-receiver offset for seismic line C-11 and (b) a display of some of those traces that lie within the rejection zone.

Special attention was given to traces that had a maximum frequency very close to 60 Hz. Since power lines and generators in North America transmit alternating current at 60 Hz, geophone cables placed near them would experience induced current in their wires. The result would be a strong 60 Hz sinusoidal signal (i.e. a mono frequency signal) superimposed on the trace. This could be seen on the cross-plot of Figure 4.6(a) as a clustering of points about 60 Hz. All of these traces deleted.

The second attribute used to delineate problematic traces from the data set was the root mean squared (RMS) amplitude of a trace. Recall that energy amplitude of seismic wave propagation in a homogenous medium decays at a rate proportionate to $1/r^2$ where r is the radius and thus this 'trend' should be observed in a cross-plot of trace RMS amplitude versus source-receiver offset as illustrated in Figure 4.7(a). Those traces whose RMS amplitude fell within the green highlighted area did not follow closely this trend and are shown in Figure 4.7(b). These traces with suspiciously high RMS amplitude were found to contain character of 'ringing' or anomalously high amplitude throughout the trace, and thus delete.

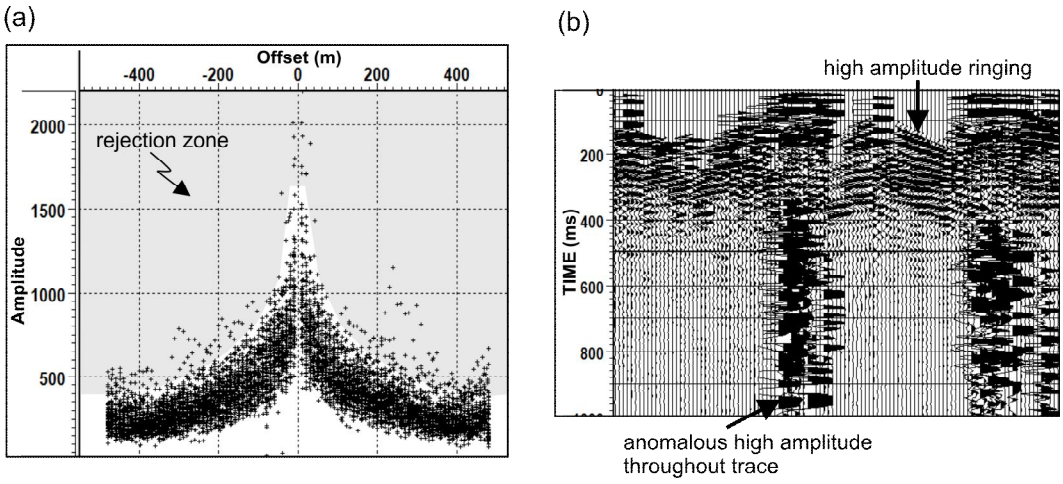

Figure 4.7: (a) Cross plot of RMS amplitude versus source-receiver offset for seismic line C-11 and (b) a display of some of those traces that lie within the rejection zone.

Polarity reversals of traces in the data were seldom seen. Almost all polarity reversals were documented in the observer log. Figure 4.8 shows a shot

record from seismic line C-03 with polarity reversed for channel 6 highlighted in red. Correcting such a trace involved a simple sign change of the trace's amplitude values.

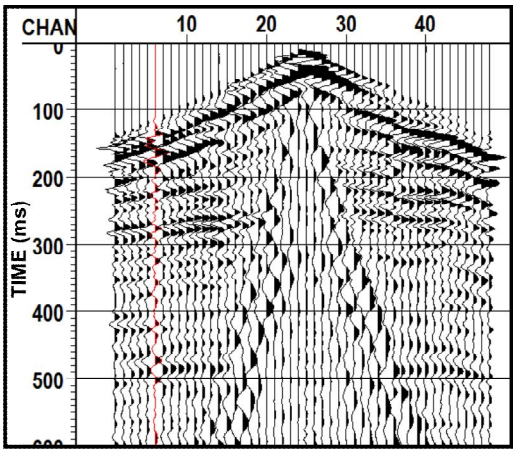

Figure 4.8: A shot record from seismic line C-03 recorded with a polarity reversal of channel 6 highlighted in red.

4.3. Initial Harmonic Analysis

The purpose of the initial harmonic analysis was to identify some of the major signal and noise events present in the data and assess the overall quality the seismic survey. The analysis was carried out by combining three separate signal analysis techniques: a frequency bandwidth analysis, a signal to noise analysis, and an amplitude/phase spectrum analysis. The results of the initial harmonic analysis were used to develop an initial frequency filter, and served as a benchmark for forthcoming processing workflows.

4.3.1. Frequency Bandwidth Analysis

The frequency bandwidth analysis was used to divulge frequency bands that embodied laterally continuous reflections across the shot record. The purpose was to identify the largest frequency window that would contain reflective signal. This analysis was also found useful in characterizing source generated noise events, such as ground roll, air wave, direct wave, and refractions.

The procedure itself involved applying a series of narrow, band-pass filters [*Shanks*, 1967] to a shot record. The ultimate high and low frequency limits

of the band-pass filters were chosen based on the practical frequency limits of the seismic data. Table 4.1 outlines these band-pass filters.

Table 4.1: A series of narrow band-pass filters.

Band-pass filter frequency range (Hz) (low truncation / low corner - high corner / high truncation)		
0/3 - 5/10		45/50 - 60/70
2/6 - 10/15		50/60 - 70/90
5/10 - 20/25		55/70 - 80/115
15/20 - 30/35		65/80 - 90/125
25/30 - 40/45		70/90 - 110/135
35/40 - 50/60		90/110 - 125/150

The zone of interest hereafter is the reflections residing between a time window of 200 and 500 ms on a shot gather. This is where the reflection arrival from the SMU is anticipated. Recall that chapter 3 suggested that a SMU reflection of zero-offset should arrive around 270 ms.

The lateral continuity of reflections was first to be analyzed. Upon examining Figure 4.9 and 4.10, the good shot record had reflection events in the zone of interest spanning a frequency band from 10 to 110 Hz. Alternatively the poor shot record had reflection events spanning from 10 to 90 Hz. Below in Table 4.2 summarizes the results of continuity of reflections and bandwidth in the seismic surveys. It appears that series C data had the highest quality while the 3D survey of series E was the worst. Furthermore, observe the entire length of the shot record and notice that the dominant frequency of reflected signal becomes lower and their bandwidth narrower with the passage of time. This is due to the stronger intrinsic attenuation of higher seismic frequencies common within all sedimentary rocks [*Jacobson*, 1987; *Neep et al.*, 1996; *Sams et al.*, 1997].

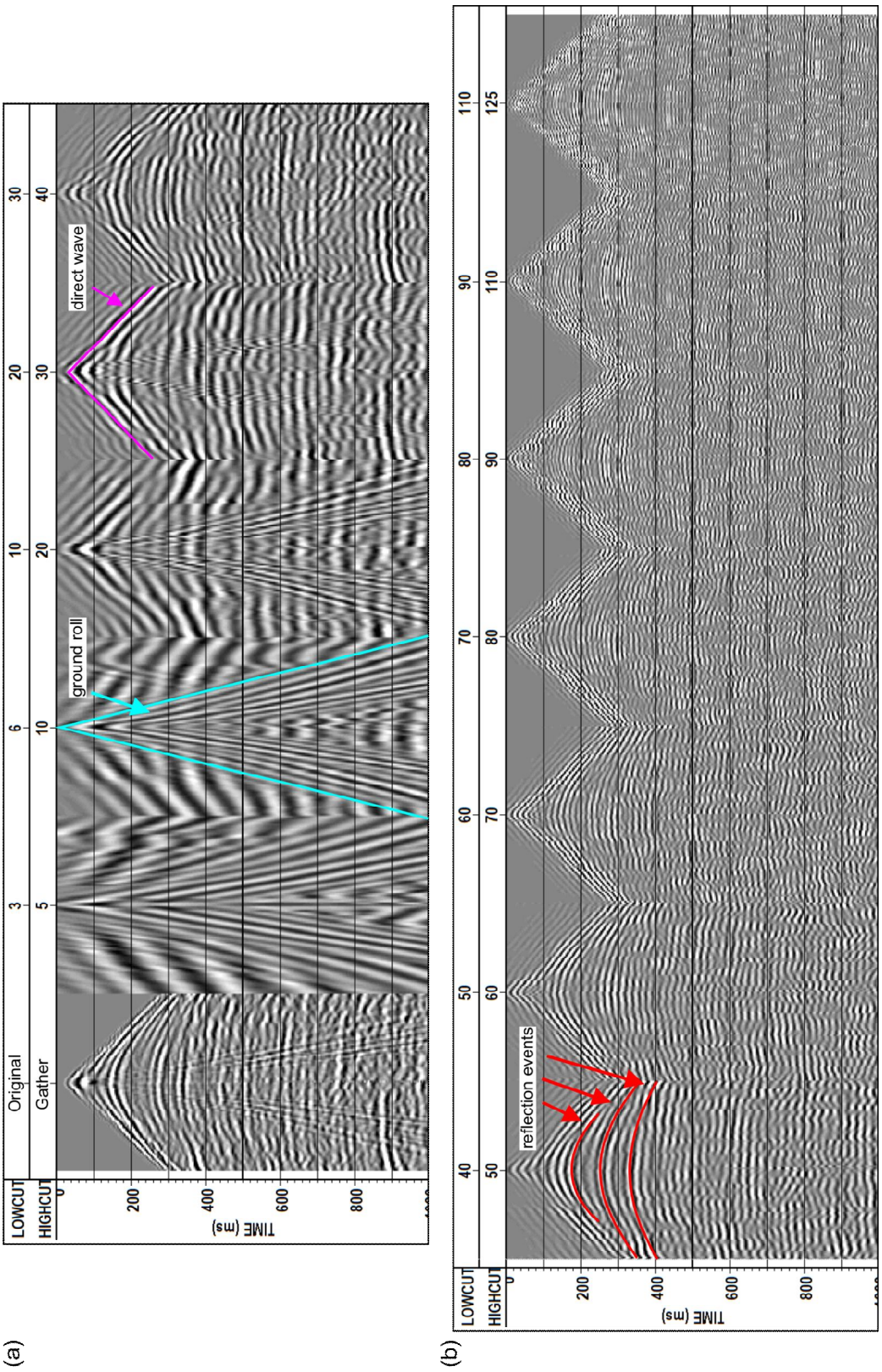

Figure 4.9: Frequency bandwidth analysis for a good quality shot record from seismic line C-10.

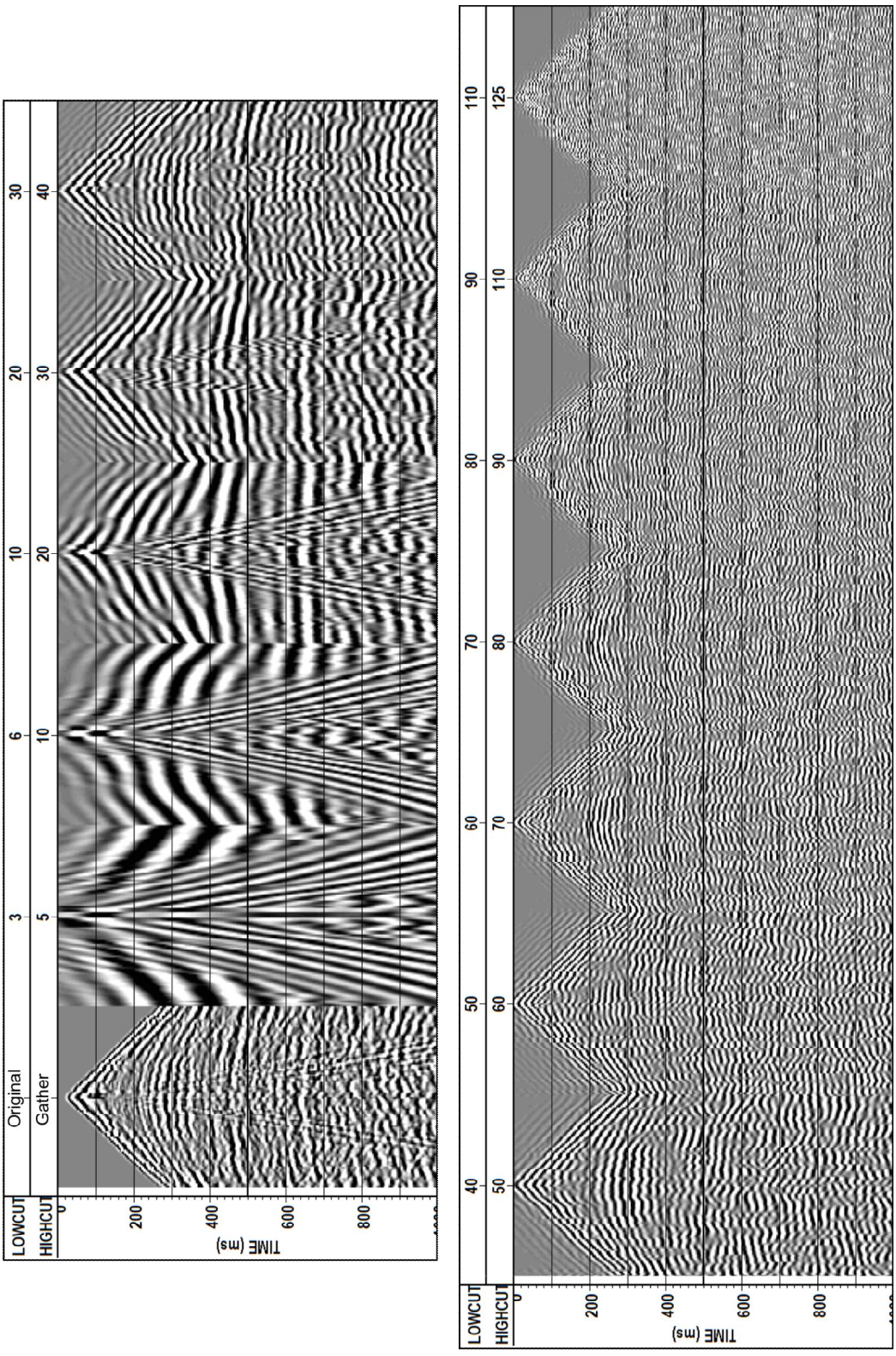

Figure 4.10: Frequency bandwidth analysis for a poor quality shot record from seismic line C-10.

Table 4.2: Estimated frequency range of laterally continuous reflection events across the zone of interest in shot records for each of the seismic surveys.

Survey Series	Frequency range (Hz)	
	Good shot record	Poor shot record
A	20 - 80	20 - 70
B	10 - 90	15 - 70
C	10 - 100	15 - 90
D	20 - 60	20 - 50
E	10 - 110	15 - 100

Secondly, Figure 4.9 and 4.10 were investigated for source generated noise. Ground roll was evident and dominated the lower frequency bands below ~20 Hz. The average linear velocities of ground roll across the entire project was about 440 m/s and widely ranged over 360-560 m/s. Moreover, the degree of ground roll contamination present in the shot records varied drastically across the different survey groups (see Table 4.3) and was largely attributed to changing acquisition parameters. The 3D survey of series D was noticed to have extremely high amounts of ground roll while the regional lines of series A virtually had no presence of ground roll. The other seismic survey fell in-between these two extremes.

Table 4.3: Summary of ground roll contamination in shot records.

Series	Recorded level of ground roll	Suppression required	Comments
A	very low	No	Ground roll in rejection band of receiver array and workers used of 30 Hz geophones. Ground roll highly suppressed.
B	moderate	Yes	Clumped geophones, no suppression.
C	low	Yes	Moderate receiver array suppression of -7 dB together with low-cut frequency filter at 12 Hz suppressed ground roll recording.
D	very high	Yes	Pea-shooter induced large amount of ground roll and virtually no suppression from receiver array. Low-cut frequency filter at 12.5 Hz had little overall effect.
E	moderate-high	Yes	Higher amplitude ground roll motion possibly due to the source array three charges per shot point. Source-receiver array had only minor suppression of -4 dB on ground roll.

The airwave was very low in amplitude or not apparent in most of the seismic surveys due to relatively small charges buried at depth for series A, B, C, and E. Survey series D, however, used a surface source that produced a significant

airwave signature in the recordings. It was present through all frequency bands and traveled with a velocity of about 340 m/s.

The direct wave was clearly recognizable at almost at all frequency bands and travelled with speeds of about 2000 ± 200 m/s. This was seen across all of the five surveys.

No other significant noise sources were found likely due to the relative remoteness of the study area from human habitation.

4.3.2. Signal to Noise Ratio Analysis

Signal to noise ratio (SNR) analysis was used to quantify the strength of reflection amplitude against the noise level in the upper 1000 ms of a shot record. The analysis was performed only on a few representative shot records from each survey group. The method used to estimate SNR was the *'trace correlation method with implications of stacking'* as outlined by Rietsch [1980].

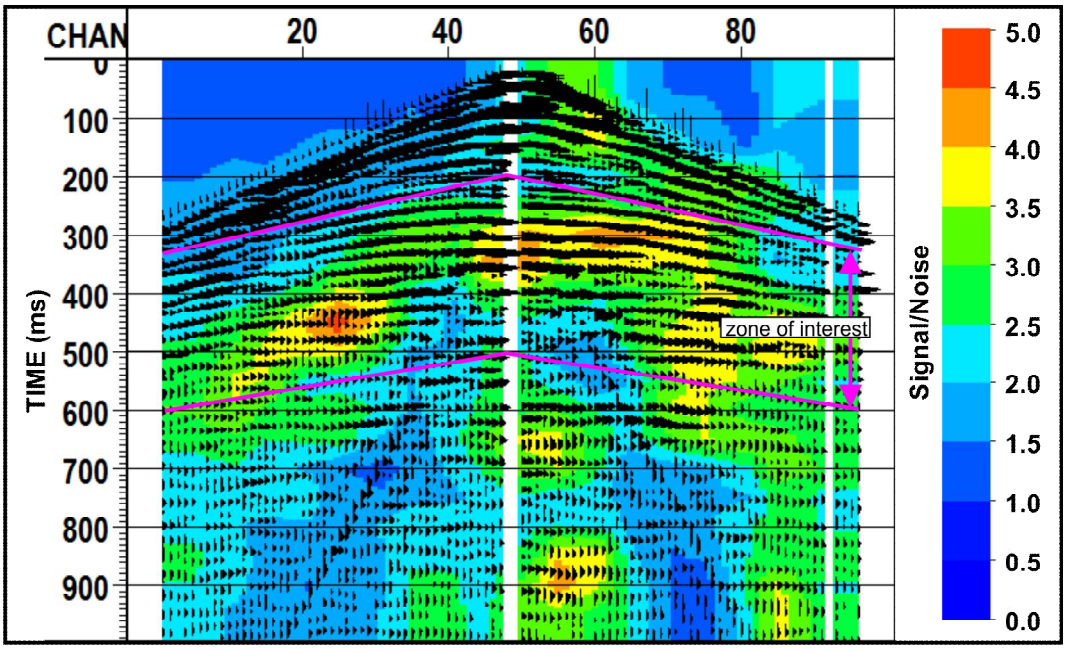

Figure 4.11: Signal to noise ratio estimates superimposed together with a shot gather from survey series C.

Estimated SNR of a shot record from survey series C is shown in Figure 5.11. Rule of thumb states that areas of SNR 3 or greater are of good quality signal. Observations from Figure 5.11 suggest that this shot record has good

signal strength over the zone of interest. Deeper reflections, such as those arriving below 650 ms, showed lower SNR values of 2-3. This was likely associated with the less seismically reflective metamorphic rocks in the Precambrian basement. All the other surveys conveyed similar results.

Furthermore, ground roll was observed to have a significant depreciative effect on SNR. Suppression of ground was also recommended by SNR analysis.

4.3.3. Amplitude Spectrum Analysis

The amplitude spectrum analysis was used assess the dominant frequency and bandwidth of the recorded seismic signal of each survey. This will provide an excellent benchmark for comparison against subsequent seismic processing techniques.

Measurements of bandwidth and dominant frequency shown in Table 4.4 were measured from a shot gather's amplitude spectrum. These measurements were averaged over 10 shot gathers to minimize the effects errors.

Table 4.4: Estimated dominant frequency and bandwidth of recorded seismic energy.

Series	Bandwidth (Hz)		Dominant Freq. (Hz)
	Low	High	
A	8	87	41
B	13	105	41
C	10	112	41
D	7	53	30
E	5	119	41

An example of measurements made for a shot record's amplitude spectrum is shown in Figure 4.12(a). The dominant frequency of the signal here is measured at 38.5 Hz. When the amplitude spectrum is shifted into decibel scale, as seen in Figure 4.12(b), the measured bandwidth is 5-123 Hz.

Survey series E was noted as having the broadest bandwidth and thus shall have the highest resolution of all the surveys. Since spectral bandwidth of the seismic pulse is inversely proportional to charge size [*A. Pap*, 1983], this is somewhat expected because survey series E used three very small 0.1 kg charges which created a sharper impulsive source while maintaining a higher energy

density. Overall, a push was noticed over the chronological time of acquisition from surveys A through E towards broader bandwidths in the signal.

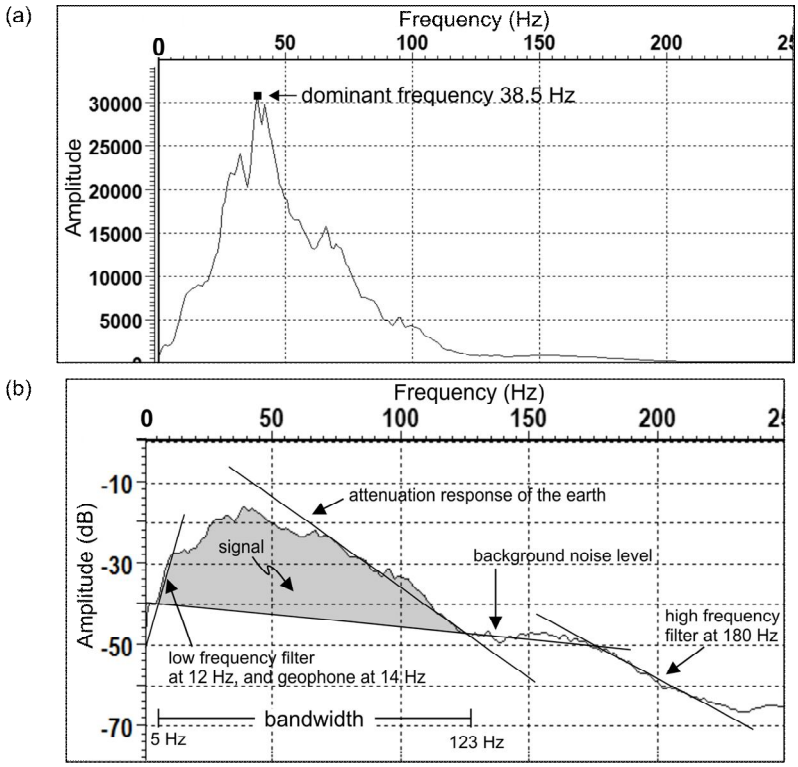

Figure 4.12: Amplitude spectrum in (a) linear and (b) decibel format for a shot record from survey series C.

4.4. Amplitude Recovery

4.4.1. Exponential Gain

Recall that the laws of physics state that energy density (i.e. the intensity) of our propagating wavefront will decay near a rate of $1/r^2$, where r is radius, due to the geometric spreading. Therefore, the amplitude of a wavefront will decay approximately at rate $1/r$. To correct for amplitude decay of the recorded seismic signal Tanner [1997] recommends the use of an exponential gain when imaging shallow carbonates. He states that its the least harmful gain correction and ensures that later processes such as deconvolution and wavelet estimation do not become problematic. Therefore the exponential gain function of

$$g(t) = t \cdot e^{nt} \tag{4-1}$$

was applied to the data, where *t* is the time and *n* is a user specified constant and must be assessed according to energy divergence of the system under study.

To assess the energy decay of our seismic data, an exponential decay analysis was performed by plotting the amplitudes of a shot record versus two-way travel time shown in Figure 4.13. The graph is plotted in such that the slope of the decaying signal directly corresponds to the exponential constant *n*, but in a negative sense [*Taner*, 1997]. The fine line represents the maximum amplitude value while the heavier line represents the geometric mean of amplitude. A slope of -1.5 was measured over a time window a time window of 0.4-1.8 seconds and thus gave $n = 1.5$ for our gain function.

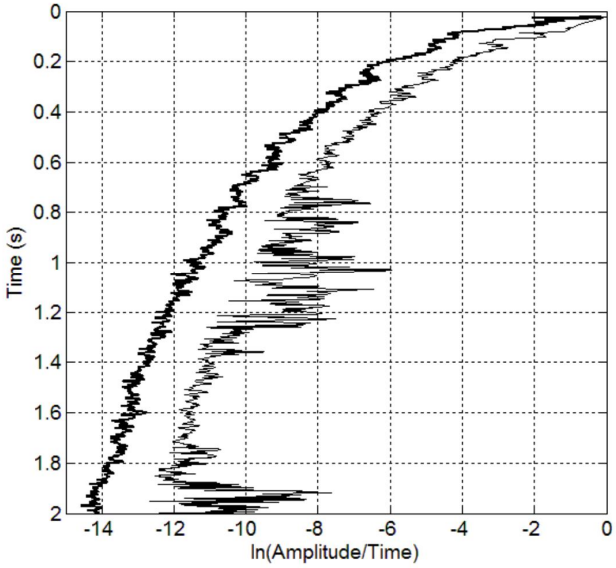

Figure 4.13: Natural logarithmic amplitude decay analysis for a shot record from survey series B. Fine line represents the absolute peak amplitude and heavier line is the geometric mean amplitude.

An example of the gain function before and after its application to a shot record is illustrated in Figure 4.14(a) and (b), respectfully. Notice that reflection amplitudes arriving later in time are increased to a similar level as early arriving reflections. Though the trace amplitudes are now balanced in time, the shot record still shows a scaling issue between lower amplitude traces on the far left and the rest of the gather.

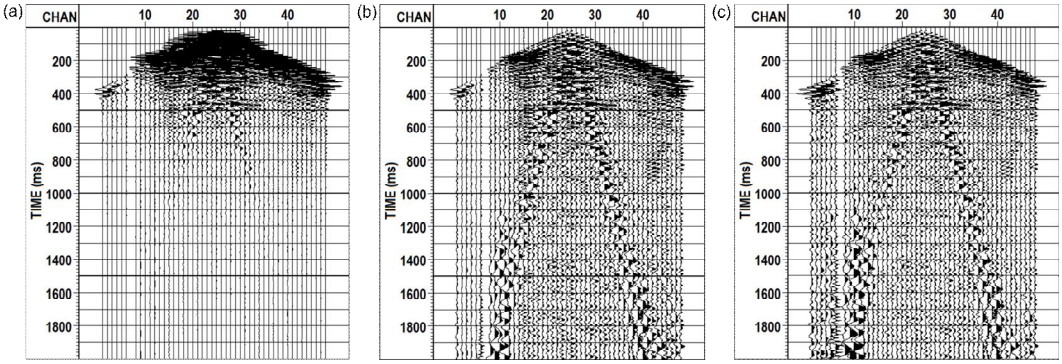

Figure 4.14: Amplitude recovery of seismic traces for (a) raw shot record, (b) shot record with an exponential gain of n = 1.5 and (c) shot record with gain and surface consistent scaling.

4.4.2. Surface-Consistent Scaling

In land surveys, amplitude variations between traces are common and usually indicative of local near surface structures affecting the local wave propagation or varying surface conditions that can cause poor source or receiver coupling with the earth. The reported presence of muskeg, a slow velocity and energy absorbing material, in near surface of our seismic surveys may have contributed to some of the major trace amplitude variations seen within the seismic lines of the project. To eliminate these amplitude variations as showcased on the left side Figure 4.14(b), trace scaling must be applied to normalize their amplitudes with respects to one another. This was accomplished by employing an approach called surface-consistent scaling based on work by Cary and Lorentz [1993]. Furthermore, simple normalization of the trace with respect to its RMS or mean amplitude was found not to be an effective method for our data set.

Surface consistent scaling was applied in the form of a *trace multiplier* = *shot performance* × *receiver performance*. The result of surface-consistent scaling applied to the shot record of Figure 4.14(b) is shown in Figure 4.14(c). Observe that channels 1 through 12 of the shot gather are now properly scaled to the rest of the traces in the record.

4.5. Static Corrections

Static corrections are applied as time shifts to a trace that amend time delay anomalies associated with changes in source-receiver elevation or variations in the depth and velocity structure of the near surface (i.e. the low velocity layer). The utility of these static corrections is illustrated by the improvement to the moveout curves of reflections with the implications of stacking and the improved imaging of seismic reflection profiles. Here we apply elevation and refraction static corrections.

4.5.1. Elevation Statics

Elevation static correction involves the time shifting of traces to rectify varying source and receiver elevations by translating them to a common datum. For a fixed datum the calculated time shift to a trace is simply given by

$$t_E = (E_S + E_R - Z_S - Z_R - 2E_D)/V_R \qquad (4\text{-}2)$$

where E_S source elevation, E_R receiver elevation receiver, Z_S source depth, Z_R receiver depth, E_D datum elevation and V_R replacement velocity. To apply the time shift t_E, it is subtracted from the two-way traveltime of the trace belonging to that particular source-receiver pair.

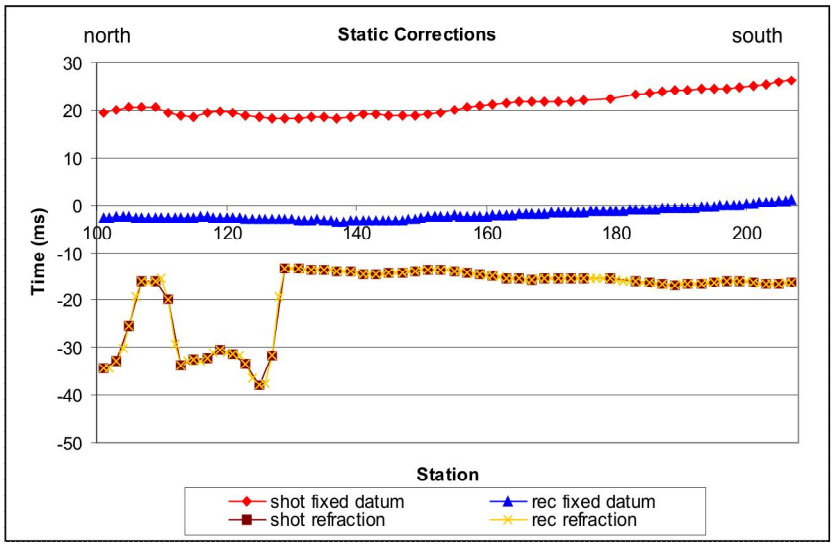

Figure 4.15: Elevation and refraction statics for sources and receivers of seismic line B-05.

For all the seismic surveys of this project, a datum of 518 m and a replacement velocity of 2255 m/s were employed. The replacement velocity was estimated from measurements of velocity of direct waves. A chart of calculated elevation statics that were applied to seismic line B-05 is shown in Figure 4.15. Observe that the time shifts of source corrections were about 20 ms larger than the time shifts for any of the receivers. This was due to the shot placed at a depth of 18 m for survey series B which positioned the source further away from the fixed datum then the receivers located at surface. Overall, elevation static variations were relatively small for seismic line B-05 and thus affirmed the proper use of a static datum (< 100 ms) in contrast to a floating datum. Of the entire seismic dataset, surface topography was rather flat and elevation static corrections were noted to be small, that is < 65 ms, for the chosen fixed datum of 518 m.

4.5.2. Refraction Statics

Refraction static correction (a.k.a. long-wavelength statics) attempts to correct for the effect of variable thickness and lateral velocity variation of the weathering layer relative to receiver spread length. An excellent review of the different refraction static correction methods is provided in the literature of Marsden [1993].

The refraction method utilized here to construct a 'model' of the near-surface layers [see pages 146-147 in *Cox*, 1999] was implemented by measuring velocity and time intercepts from the first-arrival traveltimes of shot records. An example of first break picking was shown in Figure 4.16(a) where the green dash-bots indicates the picked first-arrival traveltime on a shot gather. The first-arrival times from shot gathers were graphed versus source-receiver offset (Figure 4.16(b)). The graph was fitted with a line of best fit of which the slope (i.e. velocity) and time intercept were recorded. From these velocity and time intercept measurements a velocity model of the near surface constructed (Figure 4.17). The weathering layer was set to have a constant velocity of 600 m/s and the final velocities averaged laterally over 100 m. This velocity model was then used to calculate time corrections pertaining to each source and receiver location. These

time corrections for refraction statics are displayed back in Figure 4.15. By subtracting time per source-receiver pair of a trace corrects any time delay anomalies associated with the varying structure of the near surface.

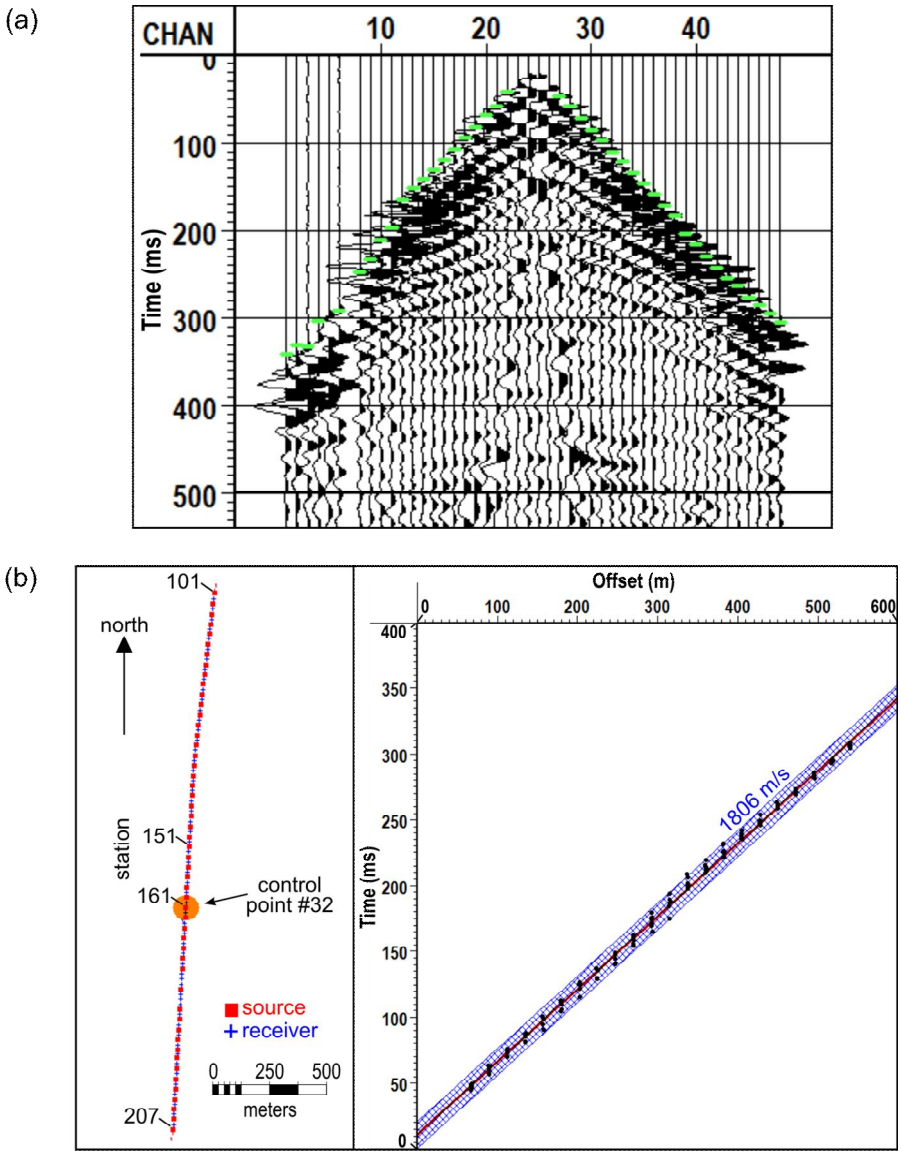

Figure 4.16: (a) Shot record with first break picks. In (b) the left panel is the surface map seismic line B-05 with a highlighted control point and right panel is the first break picks (black dots) with that control point. The line of best fit is red while the tolerance range for outliers is indicated by the blue mesh.

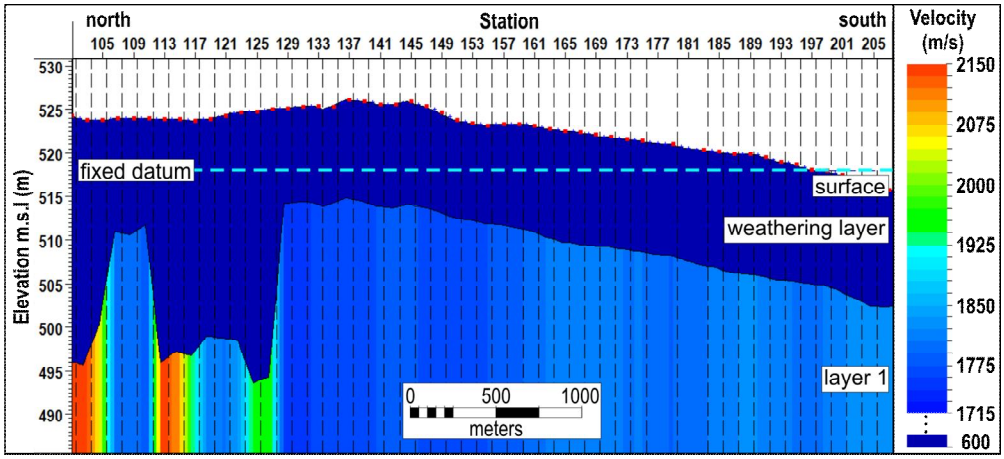

Figure 4.17: Derived model of the near surface for seismic line B-05.

4.6. Ground Roll Suppression

Ground roll is high amplitude, low velocity surface wave that can severely mask the arrivals of reflections in seismic data. Suppressing the ground roll from a shot record greatly increases signal strength over noise.

It was noted in previous the section of 4.3.1 that survey series B, C, D and E required ground roll suppression. Depending on the acquisition parameters of each survey, either f-k filtering or band-pass filtering was employed to attenuate the ground roll energy. Survey series C and E saw the application of f-k filtering while survey series B and D had a band-pass filter applied.

The use of f-k filtering (also known as velocity filtering) is to remove coherent noise events, such as ground roll, from seismic records on the basis of apparent wave velocity across the spread length and frequency [*March and Bailey*, 1983]. Illustration of Figure 4.18(a) shows the plotting of 'apparent' velocity arrivals of different seismic events on the f-k plot for a typical shot gather. Figure 4.18(b) displays the f-k plot of a shot gather from seismic line E-01 with a rejection zone, called a pie shape filter, denoted on the plot. We can see that the application of this filter successfully suppresses the ground roll in the shot gather shown in Figure 4.19.

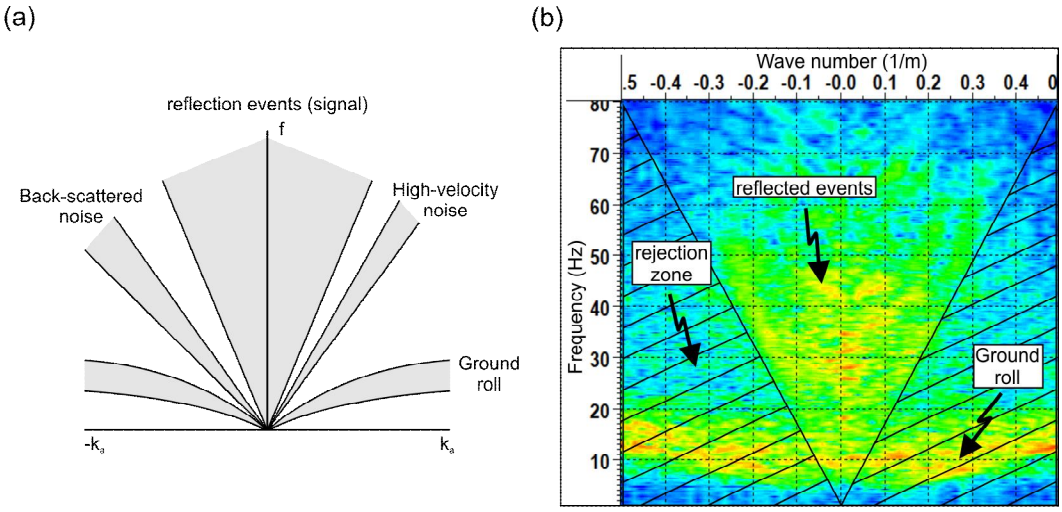

Figure 4.18: (a) An illustration of the translation of energy from a shot gather onto an f-k plot and (b) f-k plot created from a shot gather of seismic line E-01. Warm and cold colors depict high and low amplitude of energy respectively.

Although f-k filtering worked extremely well for survey series C and E, it was not a suitable approach for survey series B and D due to the fact that thier larger geophone group spacing spatially aliased the ground roll energy. When this happens, f-k filtering performance is an imperfect process, as the aliased part of the ground roll event is not removed. Therefore, a band-pass filter of 18-20-150-20 Hz was designed to reject frequencies below 20 Hz to suppress ground roll energy from series B and D data. Figure 4.20 displays the applications of band-

On a further note, it was brought to the author's attention at the conclusion of this project that the application of a curvelet domain strategy proposed by Naghizadeh and Sacchi [2011] would be an effective method to suppress spatially aliased ground roll energy rather than a band-pass filter. They suggest that building mask functions from higher scales curvelets (ground-roll-free frequencies) and projecting them to lower scales (ground roll-contaminated frequencies) provides an excellent way to subtract ground roll energy from a shot gather.

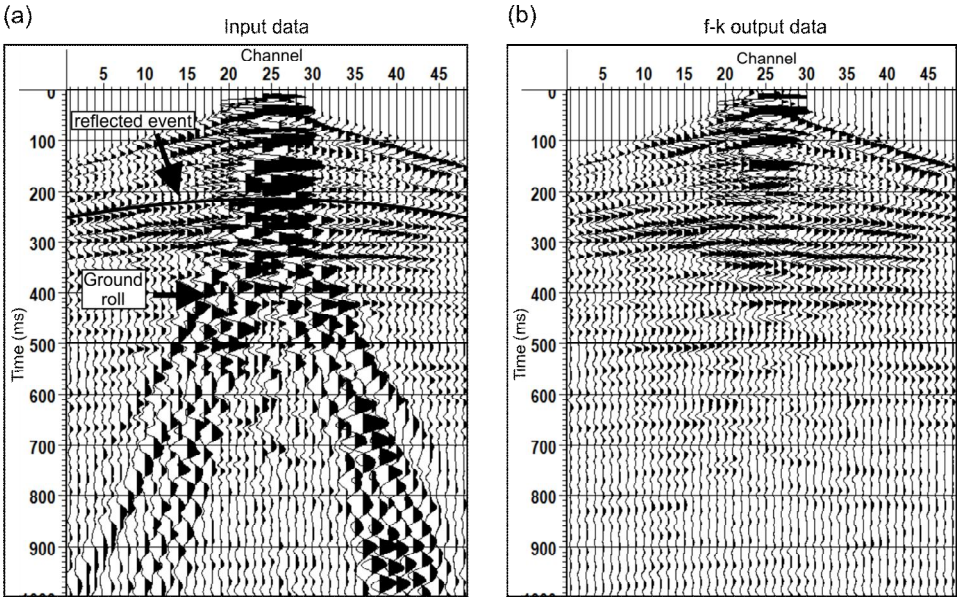

Figure 4.19: Ground roll suppression via f-k filtering method where (a) is the original and (b) the f-k filtered shot gather from seismic line E-01.

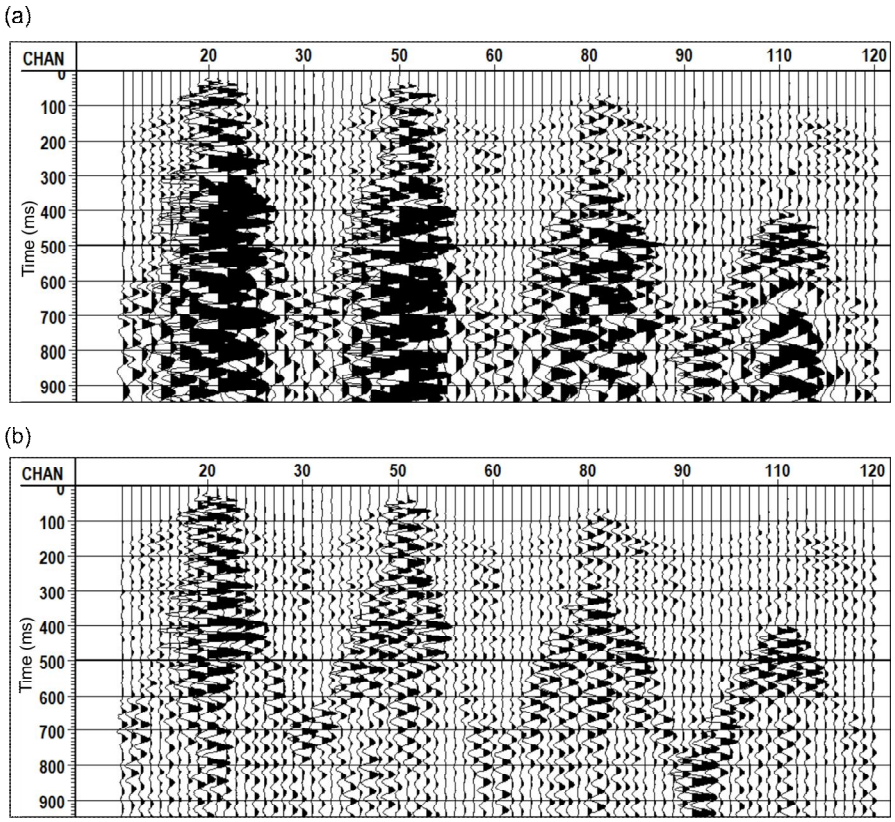

Figure 4.20: Ground roll suppression via band-pass filtering method where (a) is the original and (b) the band-pass filtered shot gather from the 3D seismic survey of series D.

4.7. Frequency Filter and Top Mute

The seismic data sets were passed with a frequency filter to remove any high or low frequency noise deemed outside the bandwidth of reflection events. From the frequency bandwidth information provided in section 4.3 wide band-pass filters were applied to the individual seismic surveys as outlined in Table 4.5.

Table 4.5: List of initial band-pass filters applied to the seismic data.

Survey Series	Band-pass filter (Hz) (low truncation / low corner - high corner / high truncation)	Comments
A	8-12-125-150	
B	17-20-190-250	Low frequencies were removed for the suppression of ground roll.
C	8-12-150-175	
D	17-20-125-150	Low frequencies were removed for the suppression of ground roll.
E	8-12-190-250	

Muting of the direct wave energy improves the subsequent stacking method of reflection events; if the direct wave is not muted, energy from the direct wave introduces noise onto stacked, shallow reflections. Muting of the direct wave is shown in Figure 4.21.

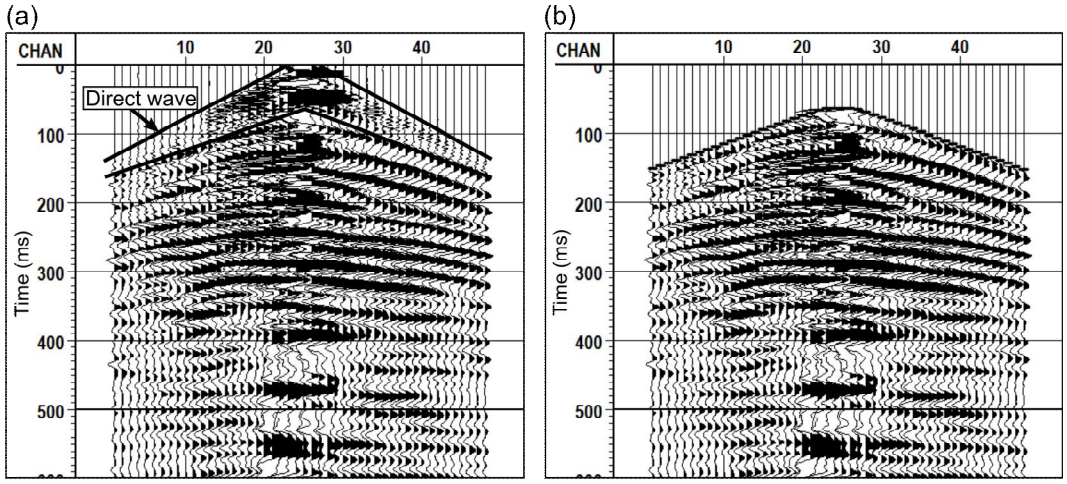

Figure 4.21: Muting of the direct wave in a shot gather (a) before and (b) after.

4.8. Deconvolution

A recorded seismic wavelet is not an ideal, clean or instant pulse. Naturally existing effects such as a bandlimited source, receiver and recording system responses, source and receiver coupling with the earth, surface reverberations and, short-period multiples all influence the seismic wavelet to become elongated and distorted. The idea of deconvolution, abstractly, is to restore the instant pulse created by the source and thus improves subsurface resolution. The process is an inverse filter operation of the seismic wavelet with the recorded trace to produce the 'reflectivity sequence' of the earth. Deconvolution yields a cleaner seismic section with much higher temporal resolution due to compression and simplification of the seismic wavelet and the attenuation of reverberations and short-period multiples.

Such as the case for this project where we have near surface conditions transitioning from wet to dry and changing soil types changing of composite soils to muskeg, we also must accounting for variations in wavelet shape caused by these near-source and near-receiver conditions. This ensures that spatial changes seen in a subsurface reflection are primarily due to a changing earth response and not of the near surface. Therefore, the surface-consistent convolution model by outlined by Taner and Coburn [1981] can be applied to the Grosmont data set.

Figure 4.22 displays the before and after effects of surface consistent, spiking deconvolution on a shot gather from seismic line E-01. An operator length of 160 ms and pre-whitening of 1% was used. The deconvolution successfully compressed the seismic wavelet into a 'spike', though are some apparent noise issues in the center-bottom half of the gather. This noise is the remnant signal of the ground roll energy.

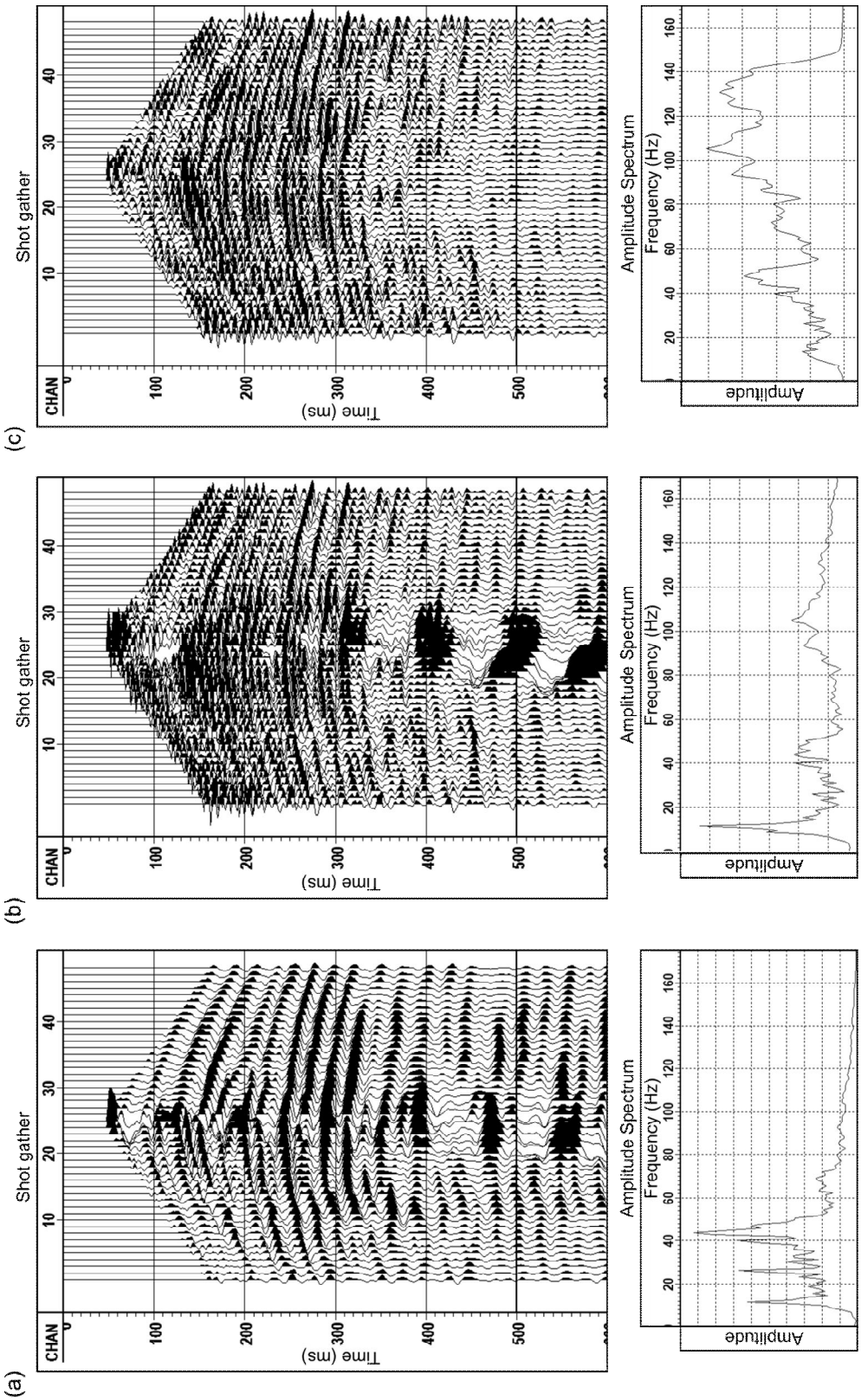

Figure 4.22: Shot gather and amplitude spectrum from seismic line E-01 (a) original (b) deconvolved and (c) spectral whitened.

4.9. Spectral Whitening

Time variant spectral whitening is utilized for the correction of source signature effects and differential attenuation of frequencies due to the inelastic response of the earth. The objective of spectral whitening is to boost lower amplitude frequencies to ultimately obtain a relatively balanced (i.e. white) amplitude spectrum (i.e. Figure 4.23). In practices the high and low frequency limits of seismic data are likely to contain higher amounts of noise and thus a more sensible approach is to have high and low frequency cut-offs.

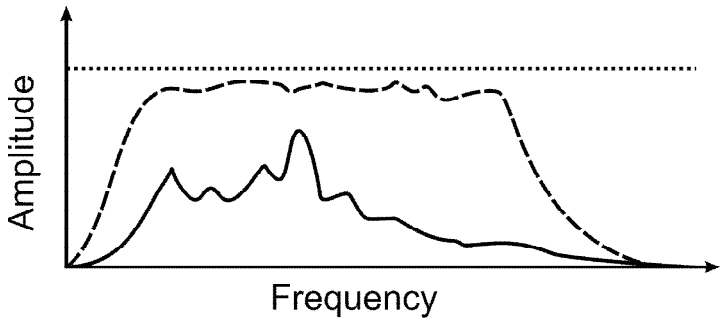

Figure 4.23: Amplitude spectrum illustration for the reflectivity response of the earth where the solid line is the recorded response, dotted line the ideal case and dashed line sensible balance via spectral whitening of the recorded response.

Spectral whitening approach used here [see *Helmore*, 2009] was applied to the deconvolved shot gather of Figure 4.22(b) to produce the spectral whitened gather of Figure 4.22(c). This new shot gather has a better balance of frequency content as observed in its amplitude spectrum. The shot gather itself has improvements in sharpness of reflection events and reduce noise from low frequencies.

4.10. CMP Sorting

A CMP gather is a collection of trace whose source-receiver combinations share a common midpoint. Since seismic data was collected in the form of shot gathers, sorting must occur to reorganize the traces into CMP gathers (see Figure 4.24 for illustration) so stacking of traces at a CMP location can take place.

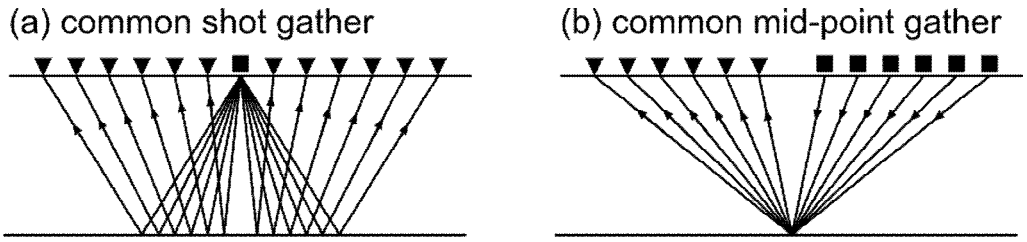

Figure 4.24: Illustration of reflected ray paths for (a) a common shot gather and (b) common mid-point gather where squares and triangles are representative locations of sources and receivers respectively.

The sorting of traces was performed by use of CMP bins defined back in section 4.2.3. The placement of source-receiver midpoints of traces within a CMP bin defines the CMP gather. An good example of this is seen in the CMP binning of seismic line A-01 where the surface geometry of the profile becomes significantly irregular (bends). Crooked line binning groups trace midpoints (black dots) that fall within a common bin location. The fold is displayed in color depicting the number of trace midpoints that fall within each bin.

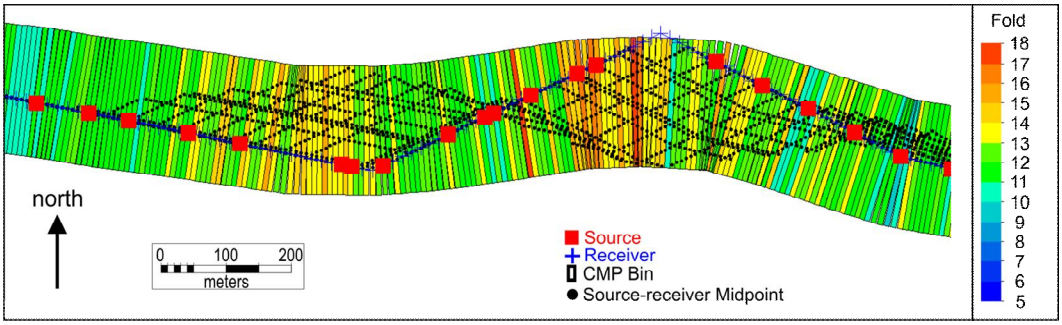

Figure 4.25: Crooked-line binning of trace midpoints for a portion of seismic line A-01.

4.11. Velocity Analysis

The objective of velocity analysis is to develop a velocity model for the earth. Recall the traveltime curve, or normal move-out (NMO) equation, of a reflection event is

$$t^2 = t_0^2 + \frac{x^2}{V_{RMS}^2}, \tag{4-3}$$

where t_0 is the initial zero-offset, two-way traveltime, x is the source-receiver offset and V_{RMS} is the velocity root mean squared structure of the earth at t_0. From

this formula we can define a hyperbola across a CMP gather by varying offset while holding the initial traveltime and V_{RMS} constant.

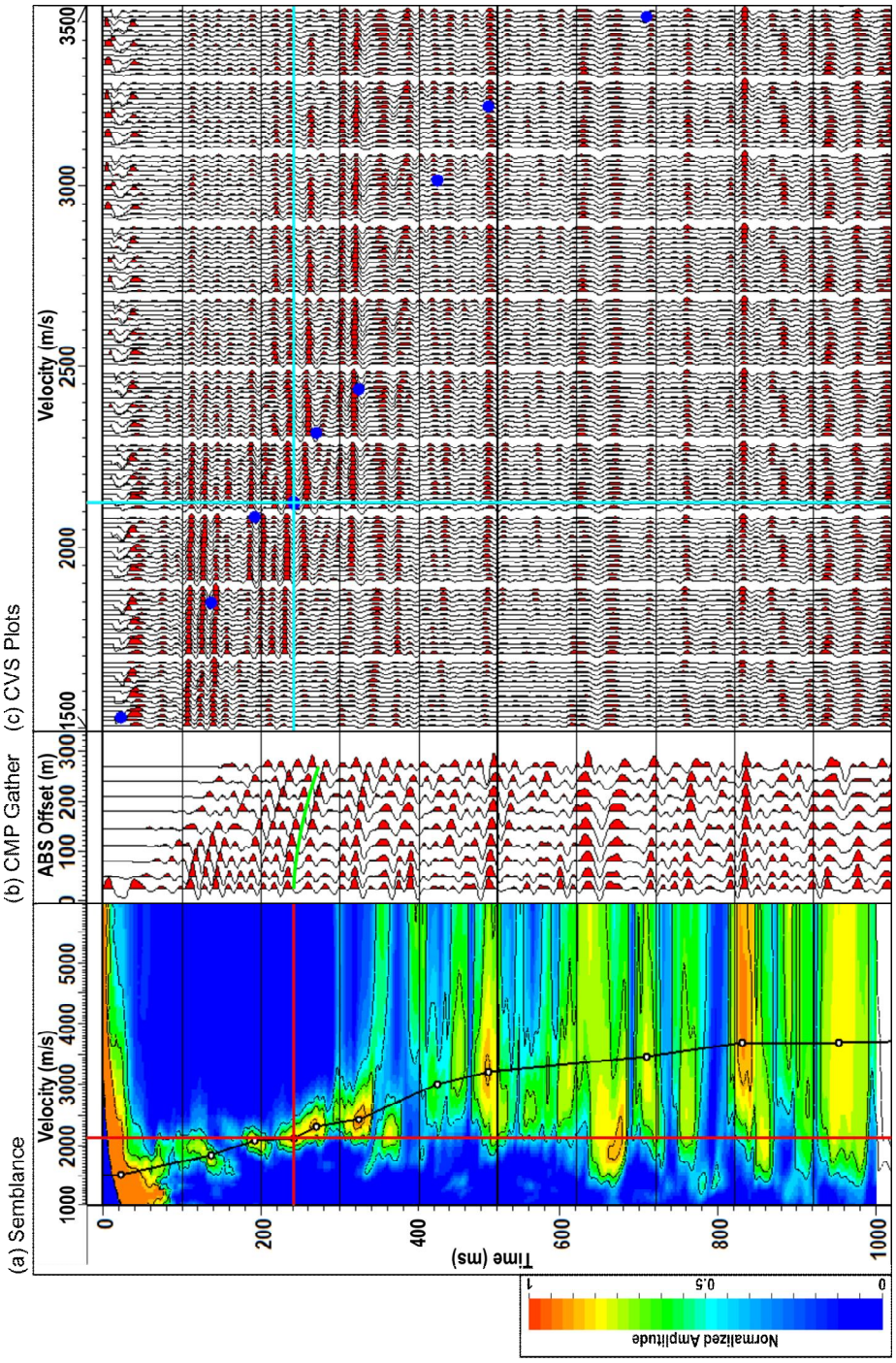

Figure 4.26: Velocity analysis for CMP #80 of seismic line E-01 where (a) semblance plot with velocity picks (white dots), (b) CMP gather and (c) CVS plots with the corresponding velocity picks from the semblance plot (blue dots). The red cross, green NMO curve and cyan cross indicate an initial two-way travel time of 240 ms and V_{RMS} velocity of 2150 m/s.

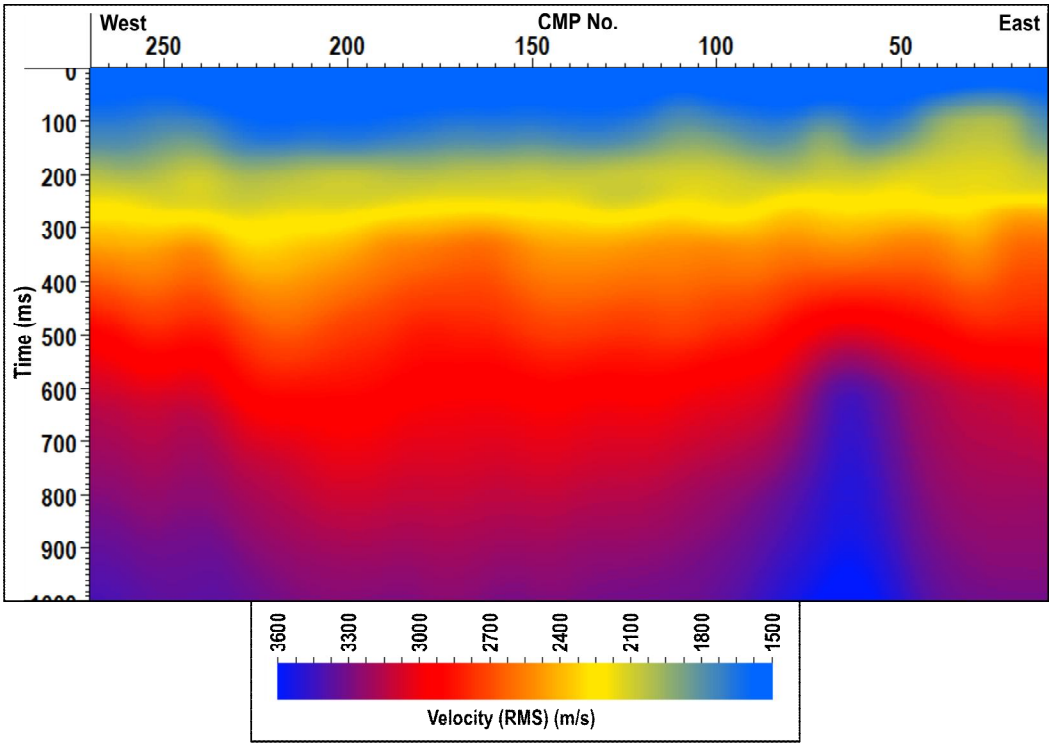

Figure 4.27: Estimated final velocity model of the earth for line E-01.

4.12. Residual Statics

Residual static (short-wavelength) correction is needed because heterogeneities in the near surface structure of the earth are not perfectly known. The model constructed in section 4.5 for refraction static correction is an estimate of this layer. It is a simplification of the geology resulting in a trade-off between thickness and velocity that result in inexact static corrections. In other words, this approximates a more complex problem that leads to the existence of 'residual' static anomalies in seismic data. Residual static correction attempts to account for this oversight by further aligning the reflections along the NMO curve in the CMP gathers.

The method used here to calculate residual statics was by the widely accepted stack-power maximization technique proposed by Ronen and Claerbout [1985]. The main advantages of this technique is that it is automated and no further supplementary information about the low velocity layer is required.

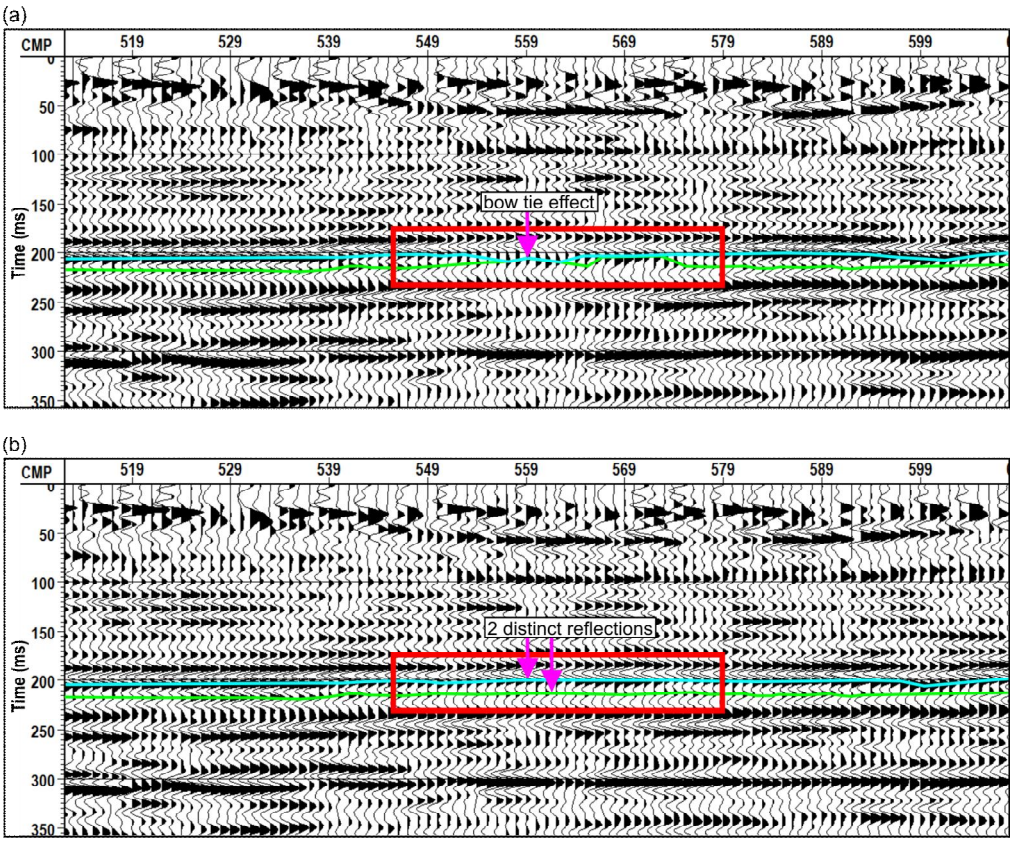

Figure 4.28: Illustrating the improvement effects residual static correction on a portion of seismic line E-01 where (a) is the original stacked section and (b) the stacked section after application of residual statics and updated velocity.

In this section, we calculated the residual statics for the traces, applied them to the CMP gathers and performed another velocity analysis to update our velocity model. This procedure repeated twice.

Figure 4.28 shows an example of the effective application of residual static correction of a portion of a stacked section from seismic line E-01. Notice the bow-tie effect highlighted in part (a) between the two, closely spaced reflectors. This phenomenon arose because these events had significant residual time anomalies that caused interference between them during stacking process. By applying residual static correction prior to stacking, the bow-tie seen in part (b) is amended. One should also note that these reflections themselves have become significantly sharper, more defined and have higher signal to noise ratios after the application of residual statics.

There is a drawback to the iterative approach of residual statics followed by velocity analysis as it is non-unique, that is the optimization is based on the interpretation of data quality of the stack section. Thus, the whole process can be highly interpretational in which a geophysicist must gauge its ultimate purpose.

4.13. Trim statics

Trim statics are used to remove small non-surface consistent time shifts in traces that may not have been resolved by the residual static algorithm of the pervious section. The method is similar to the residual static applied previously but with one important difference regarding the choice of pilot trace [see *Cox*, 1999]. In residual statics, the pilot trace is simply defined as the stacked trace of that particular CMP gather. In the case of trim statics, however, a 'model' provides the pilot trace. This model is created from a smoothed version of the latest stacked section that is constructed with all of the current static corrections and the most recently developed velocity model.

Smoothing of the stacked section was performed by F-X deconvolution [see *Canales*, 1984] which 'smoothes' the data across space (i.e. horizontal direction). This trick that alters the stacked pilot trace at particular CMP location and differentiates trim statics from residual statics. The parameters employed in F-X deconvolution were a filter length of 3 traces, a design window of 100 traces and a cut-off frequency of 100 Hz. The prediction filters were calculated over a time window range of 150-700 ms.

Trim statics were calculated and applied to the CMP gathers. This was followed by another velocity analysis to produce the final velocity model of the subsurface.

4.14. NMO Correction

The purpose of NMO (normal move-out) correction is to prepare the data for stacking by flattening reflection events in a CMP gather. The NMO correction, is described by a simple time shift of amplitudes within a trace given by the difference between t and t_0, that is

$$\Delta t_{NMO} = t - t_0 , \qquad (4\text{-}4a)$$

or by way of Equation (4-3),

$$\Delta t_{NMO} = t_0 \left[\sqrt{1 + \left(\frac{x}{V_{RMS}} \right)^2} - 1 \right] \tag{4-4b}$$

where we recall that t_0 is the initial two-way traveltime of a zero-offset reflection in a CMP gather, x is the source-receiver offset of a particular trace and V_{RMS} is the velocity root mean squared is the velocity structure, estimated from velocity analysis, of the earth at t_0. Values of V_{RMS} and are taken from the final velocity model developed for a seismic line.

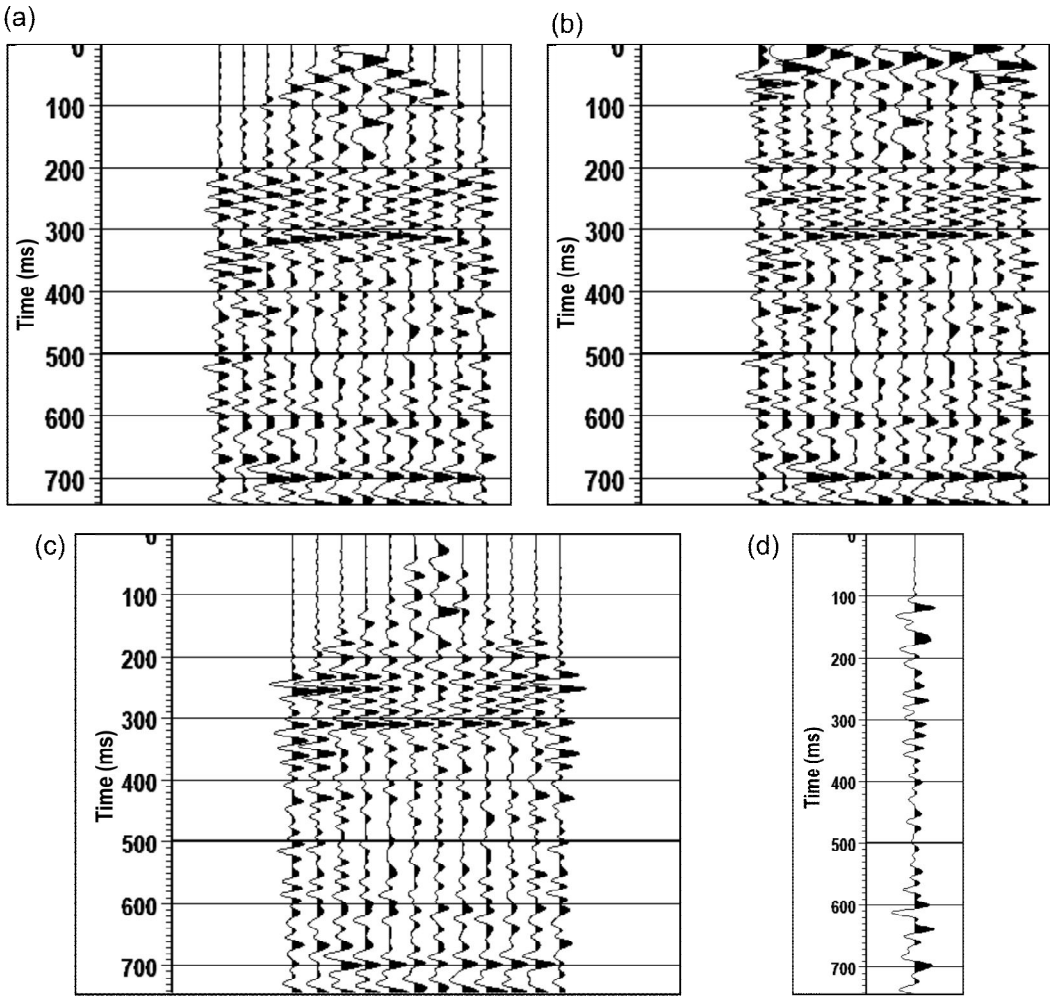

Figure 4.29: Stacking of a CMP gather where (a) is the original gather, (b) NMO corrected, CMP gather, (c) with stretch mute applied and (d) the final stacked trace by summing of traces in (c).

If the estimated velocity model of the earth is correct, a reflection event in NMO-corrected CMP gather should appear horizontally flat. However, if the velocity is too high the event will be undercorrected (i.e. concave down) and likewise if the velocity was too low the event will be overcorrected (i.e. concave up). Figure 4.29 shows the result of a CMP gather before and after the application of NMO correction. Observe that the reflection events have been flattened in the NMO-corrected gather of Figure 4.29 (b).

A common problem with NMO correction is the stretching, frequency distortion, of the seismic wavelet particular to shallow events at large offset. This is inherently due to the V_{RMS} function in Equation (4-4b) and illustrated by Figure 4.30 where the dominant period T of a wavelet is stretched so that its period is T_0 is greater than T after NMO correction. Because of this stretching at large offsets, stacking the NMO-corrected CMP gather of Figure 4.29(b) can severely degrade the quality of shallow events. The problem can be ratified by muting the stretched zone of the gather.

Automatic muting, using a quantitative definition of stretching, of a NMO corrected CMP gather is performed by

$$\frac{\Delta f}{f} = \frac{\Delta t_{NMO}}{t_0} \tag{5-10}$$

where f is the dominant frequency, Δf is the change in frequency and Δt_{NMO} is given by Equation (4-4b). By defining a percentage of allowable stretch in frequency, one is able to automatically mute zones of excessive stretching in the seismic wavelet.

A trade-off does exist between the signal to noise ratio and the amount of stretch muting applied. In particular, if the signal to noise ratios of shallow events is good, then it may be preferable to mute more harshly to preserve signal bandwidth. Conversely, if the signal to noise ratio is poor, it may be necessary to accept a large amount of stretch in the waveform to get events to appear of the stacked section.

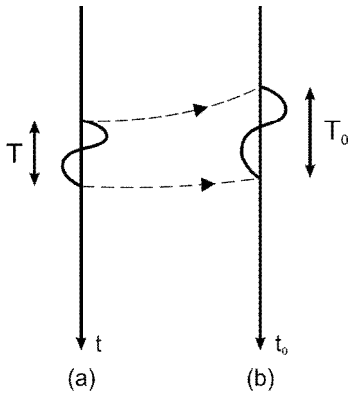

Figure 4.30: A signal of period *T* (a) is stretched to a signal of period T_0>*T* (b) after NMO correction.

A stretch mute of 20% was chosen. It was felt that this was a good compromise between the low fold of the surveys, and signal to noise ratio. Nevertheless, Figure 4.29(c) shows an NMO-corrected CMP gather with the applied stretch mute.

On a further note, no compelling evidence was uncovered, given the geology and rather small offsets of the seismic surveys, in the project area to suggest that non-hyperbolic moveout would not present a significant factor nor was it observed in any of the seismic data. No further corrections, such as dip moveout correction, were required if this phenomenon was present. That said future work may want to include borehole seismic studies to assess the degree of anisotropy in the area to see if it should be accounted for in the processing.

4.15. CMP Stacking

Stacking NMO corrected traces enhances the signal to noise ratio of a reflection by the constructive interference; thus, also suppresses coherent and incoherent noise through the averaging effects. CMP stacking is the process of summing traces within a NMO corrected CMP gather (Figure 4.28(c)) [*Mayne*, 1962; *Yilmaz*, 2001] to produce a single stacked trace (Figure 4.28(d)). This trace is then normalized to account for varying fold along the profile of the seismic line.

An example of the stacked section for line E-01 is shown below in Figure 4.31.

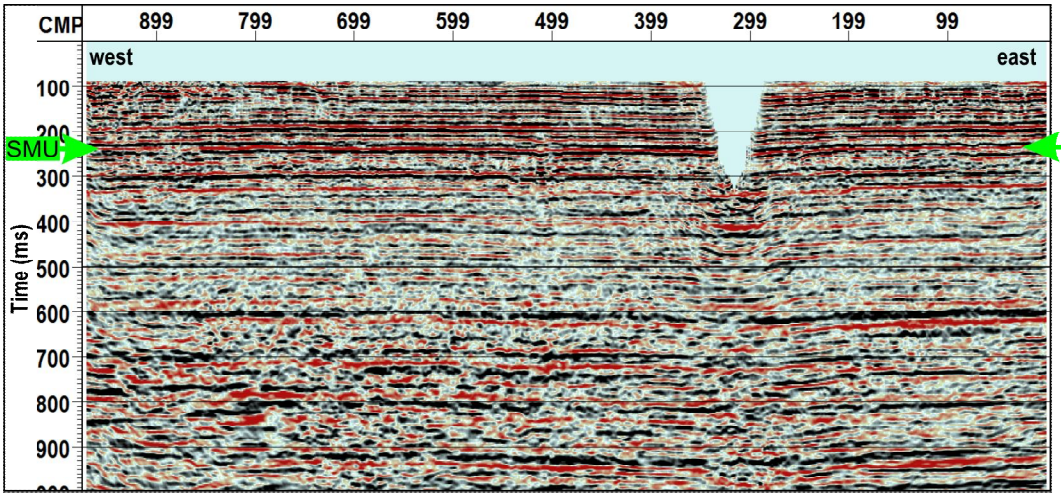

Figure 4.31: Stacked section for seismic line E-01.

4.16. Migration

Seismic migration is the practice of collapsing diffraction events to points, thereby moving (i.e. migrating) reflection events to their proper location creating a true image of structures within the earth. Here we look at two different methods of post-stack and pre-stack time migration.

4.16.1. Finite Difference Migration - Post-Stack

The finite difference (FD) migration [see *A. J. Berkhout*, 1979; *Hale*, 1991; *Ristow and Ruehl*, 1994] is based on the fundamental principle of the parabolic equation for a diffraction. The application of this migration algorithm is a straightforward task that can be applied to any post-stacked data set with an arbitrary velocity model.

The FD migration algorithm used final velocity model of the earth developed by velocity analysis. Parameters of the algorithm were 2 ms tau step, 50 trace taper pad and applied a filtered 45-65 degree solution. An example of the post-stacked FD migrated image for seismic line E-01 is shown below in Figure 4.32. This method was found to perform suitably at collapsing diffractions and migrating events on the stacked section of Figure 4.31. Also note that FD migration effectively acted like a smoothing filter in the *x* direction (horizontal).

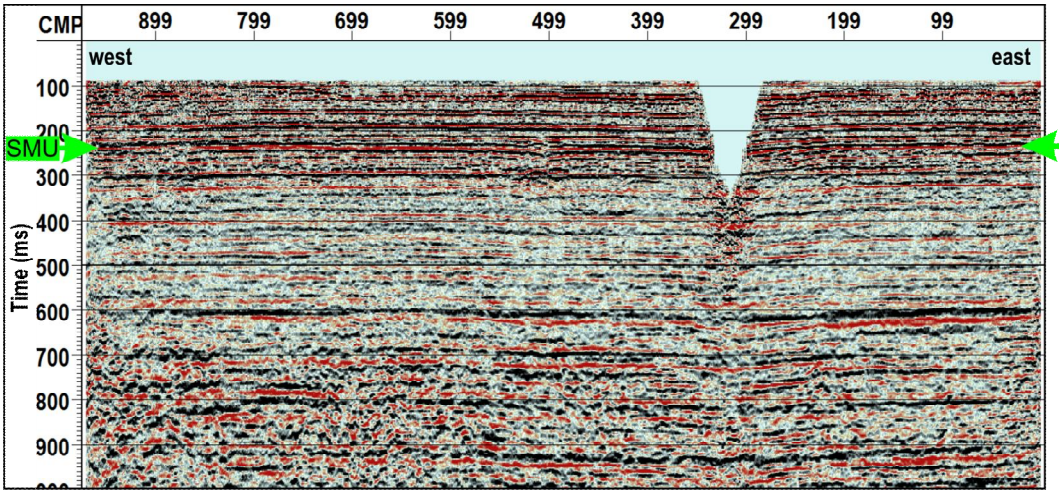

Figure 4.32: FD migration for seismic line E-01.

4.16.2. Kirchhoff Migration - Pre-Stack

The basis of pre-stacked Kirchhoff time migration (PSTM) of wavefield theory for scattering points will not be covered here, but there is vast reference literature available on this topic [to name a few *Alkhalifah*, 2006; *Claerbout*, 1985; *Docherty*, 1991; *S H Gray et al.*, 2001; *Hubral*, 1977; *Schneider*, 1978; *Yilmaz*, 2001]. The application of PSTM is rather simplistic as it involves defining a velocity field and an aperture width for migrating CMP gathers. We proceed with a two steps procedure of velocity image analysis and aperture image analysis to update our velocity model and build a space-time-variant aperture profile, respectively.

The purpose of migration aperture analysis was to adjust the aperture limits along a seismic profile. This was important because signal quality in many of the seismic lines of the project varied along their profile. In areas of poor signal to noise ratio the aperture width was made narrower to avoid migrating large amounts of noise. A summary of the fundamental limitations of aperture width in practice was found on page 509 of Yilmaz [2001].

The final constructed PSTM image of Figure 4.33 for seismic line E-01 utilized an updated PSTM velocity model and a space-time-variant aperture profile designed for a seismic line. The PSTM image shown below is a smoother solution than the FD migrated image of Figure 4.32. This is due primarily due to a

superior migration algorithm of the Kirchoff migration performed in the pre-stacked domain.

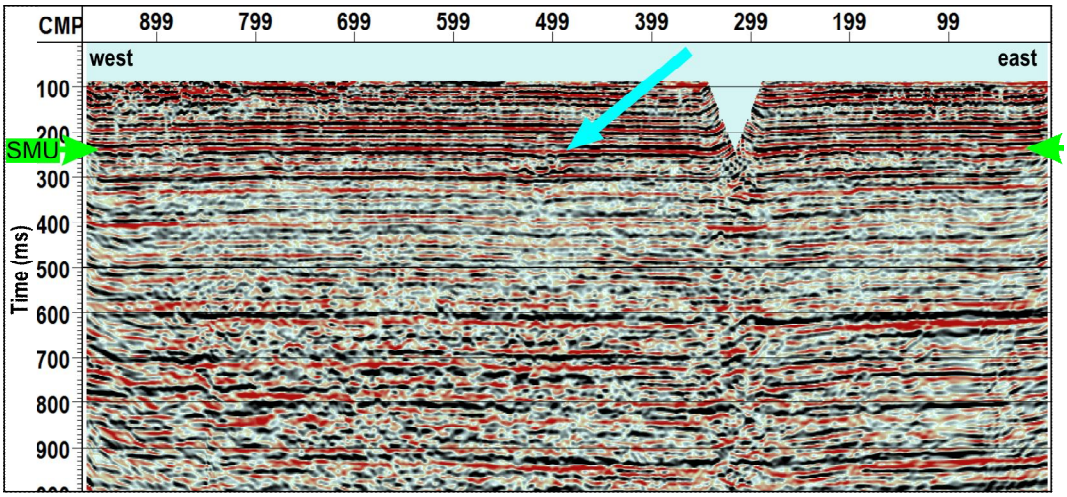

Figure 4.33: PSTM image for seismic line E-01.

One final note, an interesting undulation is clearly evident in the PSTM image of Figure 4.33 (denoted by cyan arrow) near CMP 520 and time 280. This could be related to karsting or other internal structural changes within Grosmont formation. At this point, it is hard to prove either but it is admissible that the structure is somehow different at this location from the background geology.

4.17. Post-Stack Clean-up

4.17.1. White Noise Suppression

Despite our best efforts, it was evident that most of the seismic data, except for survey series E, still had significant noise issues in their stacked sections. Therefore, it was decided that post-stack noise removal would be of benefit to enhance the reflection events in the stacked and migrated seismic sections. The method of white noise suppression called W2DNoise and W3DNoise [see *GEDCO*, 2009] provide in Vista™ software was employed for this task, it is similar to a neighbourhood noise attenuation technique. This was chosen over other methods, such as f-x predictive deconvolution, because it

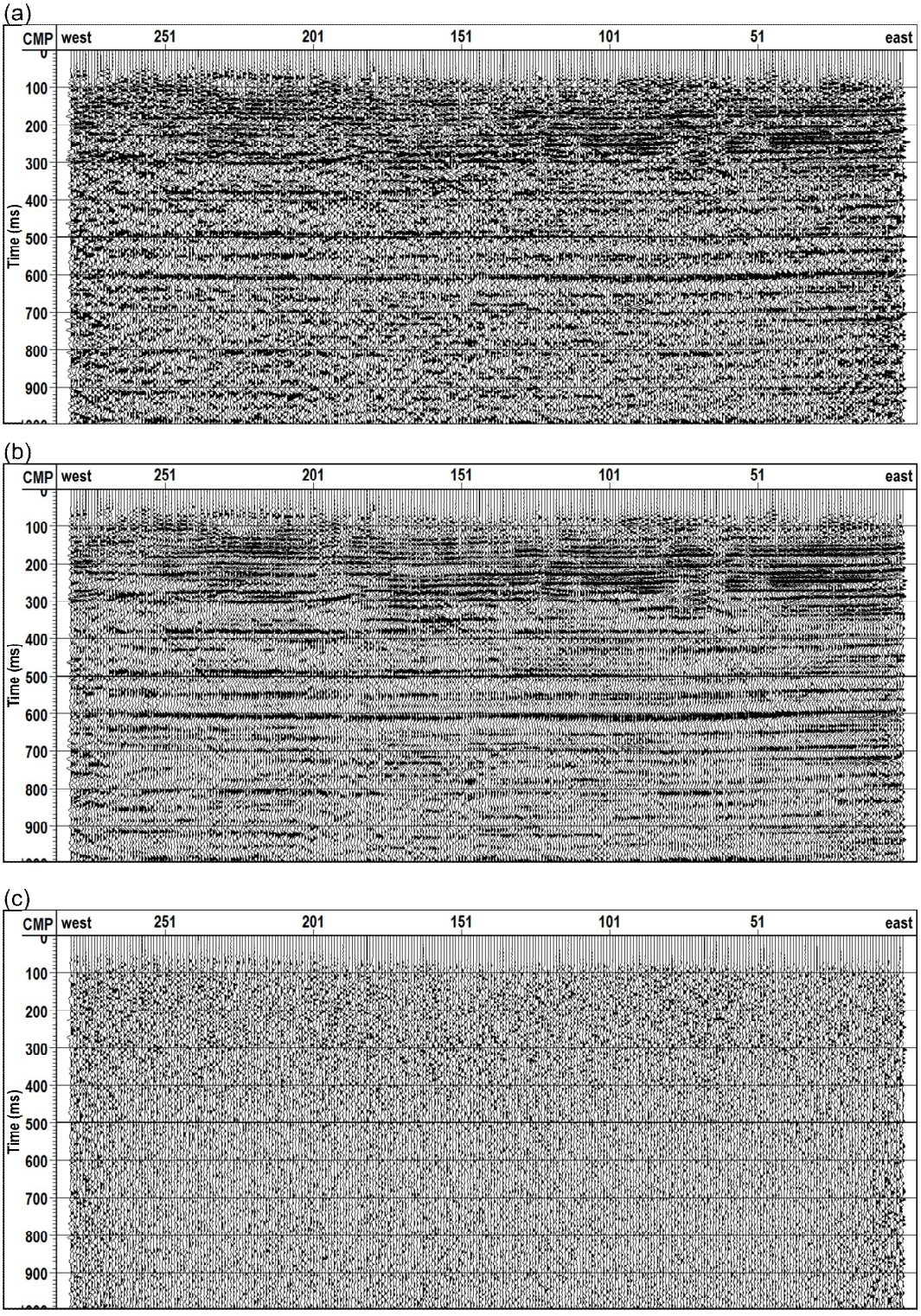

Figure 4.34: White noise suppression for seismic line B-02 where (a) is the final stacked section, (b) cleaned stacked section and (c) the difference between (a) and (b).

'preserves' trace amplitudes while adequately suppressing spatially random noise that is uncorrelated from trace to trace.

Seismic line B-02 was definitely not of the best quality data. The results from white noise suppression performed on this data is shown in Figure 4.34, the original stacked section and the cleaned stacked section and the difference between the two images. The Minimal loss of signal was apparent from this cleaning process. This filtering technique adequately suppressed the noise and greatly improved the data quality of the final stacked images.

Stacked and migrated images were cleaned by this process for every seismic survey for all of the seismic surveys.

4.17.2. Frequency Filter and Scale

A final filter and trace scale were applied to the cleaned seismic data. All data was passed with an Ormsby band-pass filter of 2-7-90-105 to rectify any last noise issues and to establish a uniformity of frequency content between the seismic surveys. Finally, trace normalization was applied over a time window of 150 ms - 700 ms based on mean amplitude. The full processed stacked and migrated images of survey series A, B, C, D and E were finally ready for interpretation.

4.18. Summary

In summary, the frequency band analysis highlighted that reflection events arriving over the time window of 200-500 ms generally had a broad bandwidth ranging from 10 to 100 Hz . Survey series D was the exception to this, it had a notably smaller bandwidth of 20-60 Hz. Ground roll was noted as being the most prominent noise in the data and suppression of it was key in maintaining high levels of signal to noise about the SMU reflection. Seismic survey E was found to have the best recorded signal due to the application of an array of small charges for the source. Seismic survey D was noted as the worst due to the poorer performance of the pea-shooter as a source.

The processing workflow was optimized on enhancing the reflections residing about the SMU. A major part of this was proper application of residual statics and careful velocity analysis. Taking care in building the velocity model was found to be the most crucial step in the processing workflow.

Fold was also noticed to hamper data quality. Reflection off the SMU for offset greater than 280 meters arrived near to the direct wave arrival. Muting of the direct wave also caused muting of SMU and shallower reflections at these far offsets. This essentially meant that the fold coverage at the SMU reflection for survey series B dropped from 1200% to 600% and survey series A dropped from 1200% to about 400%. Signal to noise ratio of the SMU of these surveys were drastically lower than the others.

Diffractions were noticed about the SMU in the seismic data. These could be due to karst structures related to the Grosmont Formation. The migrated images, with there improved spatial resolution and collapsed diffractions, should be more sensitive to small karst features than those in the regular stacked section.

Data quality of the large regional lines was better in the western section of the profiles than the east. It was not clear as to why.

Chapter 5 Forward Seismic Modelling of Karst Features

5.1. Overview

The goal here was to study the resolvable limits of 2D seismic data over karst features present at the SMU interface. This section will focus on the development of an appropriate geological model, the full-wavefield seismic modelling technique and a discussion of the results. It was shown that dolines could be imaged on migrated sections down to an approximate diameter of 160 meters by presence a break and time sag in the surface of the SMU horizon. For doline diameters ranging between 25-160 meters, a varying degree of dimming should be observed. On the other hand, karst valleys will have better resolution lateral resolution in regards to 2D seismic data. Karst valleys greater than 25 meters wide that were oriented nearly perpendicular to the profile of a seismic line. Resolution of these narrow karst valleys will diminish as the seismic line is rotate away from this perpendicular axis.

5.2. Two-Layer Model

A simple two-layer model of sandstone over dolomite was chosen to represent the geomorphologic structure about the SMU interface (see Figure 5.1). Velocity, density, and depth values of the model were estimated from VSP and well log data within the area of the project. To follow is a description of the construction of the two-layer model.

Recall that spatial resolution of reflection seismology only depends on the average velocity down to a reflector at depth [*A.J. Berkhout*, 1984]. Therefore it was acceptable to depict the geology above the SMU as single layer of constant velocity. This layer was simply given the average P-wave velocity from surface to SMU as measured from the results of a VSP survey in the area [*Schacter*, 1985], see well location W-01 on the project area map back in Figure 3.1(b). The average seismic velocity from the surface through the Cenozoic and Mesozoic sediments

down to SMU measured about 2000 m/s. The 1st layer the geological model was thus fitted with this average P-wave velocity.

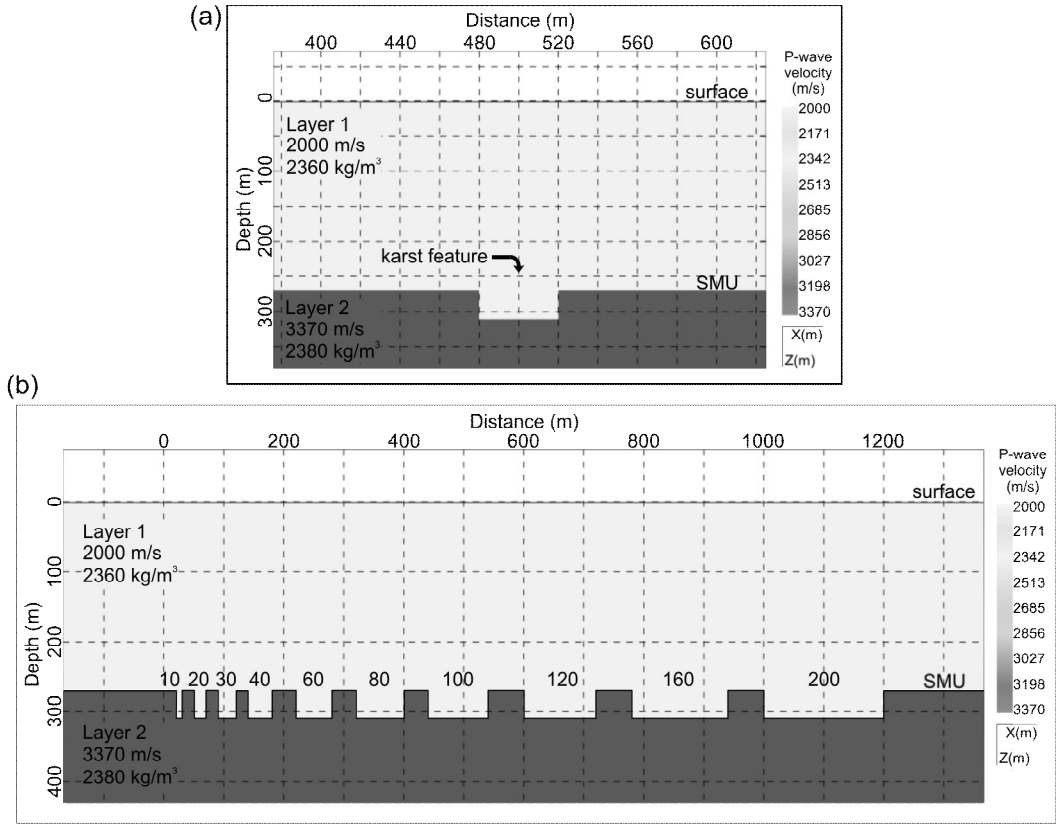

Figure 5.1: Two layer geological model about the SMU with (a) a single karst feature and (b) multiple karst features varying in width at the SMU.

The layer below the SMU shall resemble Grosmont D member, the upper most member of the Grosmont formation. P-wave velocity of the Grosmont D member was measured from the same VSP survey [*Schacter*, 1985], which reported it at 3370 m/s. This value assigned as p-wave velocity for the 2nd layer of the geological model

Densities of the layers 1 and 2 were measured from the density log at well location W-01. The average density within the Wabiskaw formation, the formation overlying the SMU at the well location, was measured at 2360 kg/m^3 and assigned layer 1. The average density within Grosmont D member was measured at 2380 kg/m^3 and assigned to layer 2.

Since no direct measurements of S-wave velocity were available in the area, estimates were made from Barton's [1986] relationship of seismic P-wave and S-wave velocities for continental rocks. From the P-wave velocities, the estimated S-wave velocities for layer 1 and layer 2 were calculated to be 1150 m/s and 1945 m/s respectively.

Depth of the SMU interface was estimated from well log data collected in the immediate area of high-resolution seismic surveys. The SMU surface was found to reside at an approximate depth of 270 m. Therefore, the thickness of layer 1 in the geological model was set to this value.

To simulate the effects of karsting on the SMU surface a rectangular block was cut into layer 2 at the SMU surface (see Figure 5.1). This is a good approximate of real karst features such as collapsed dolines, and karst valleys that have distinctive vertical walls [i.e. *Colpaert et al.*, 2007]. Without having any constraint on the bottom shape of our karst features, a flat bottom was employed. Furthermore, layer 1's properties were assigned into the rectangle block of the simulated karst feature that was cut into layer 2. This was validated from core evaluations from Hopkins and Jones [2009] where they suggest that the infill of the karsted terrain appears to be genetically related to the Wabiskaw formation residing immediately above the SMU.

To study the resolution power of the seismic data on the simulated karst feature, many models were developed by modifying the rectangular block over a range of widths 10 - 200 meters and depths 20 - 40 meters. The models were investigated by two different methods: independently as a single simulated karst feature and as a collective group of multiple simulated karst features as illustrates in Figure 5.1 (a) and (b) respectively.

5.3. Forward Seismic Modelling

To accomplish the task of full wavefield simulation through our constructed two-layer geological model, software of *Tesseral 2D*™ supplied by Tesseral Technologies Inc was utilized. The software models the elastic response of the earth through the finite differences of various partial differential equations

of wave propagation [see *Cao and Greenhalgh*, 1998; *Dai et al.*, 1995; *Graves*, 1996; *Saenger and Bohlen*, 2004; *Virieux*, 1986]. By suitable choices of the thickness, density, and elastic properties (P and S velocities) of each layer in our model, the real conditions of the earth can be approximated.

Next, we introduce the acquisition parameters assigned to the software to design our own CMP shooting technique across the profile of our model.

The bandwidth of the source was at best to replicate the recorded seismic wavelet of survey series E produced by a dynamite explosion. From the amplitude spectrum analysis of survey E, it was observed that the record wavelet was minimum phase and had a dominant frequency near 40 Hz. Therefore, it was advisable to use a minimum phase Ricker wavelet of same dominant frequency [*Hosken*, 1988]. The mode of the source was set as a compressional, omnidirectional impulse. Figure 5.2 illustrates the source wavelet that was implemented into the forward modeling software in time and its amplitude spectrum.

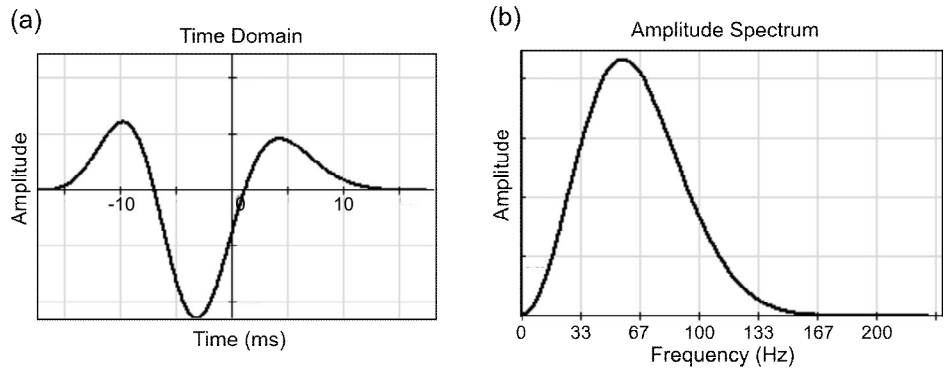

Figure 5.2: Source signature of a minimum phase Ricker wavelet with dominant frequency 40 Hz displayed in (a) time and (b) frequency domain.

Acquisition parameters of source, receiver and recording were also set to replicate that of survey series E (see Table 4.1). The source interval was set at 20 m, geophone group interval at 10 m, and number of channels at 48. The model had the similar split spread configuration and fold coverage of 1200%. The source depth was set to 5 m and the recording parameters set at 1 ms sampling rate with recording length only of 600 ms to save on computational time. However, unlike survey series E, a single source was employed instead of an array of three.

Shot gathers were then computed by propagating the seismic disturbance through the two-layer model and recording the response at the receiver locations on the surface. A snap shot of this simulation with the propagating seismic wave is shown below in Figure 5.3.

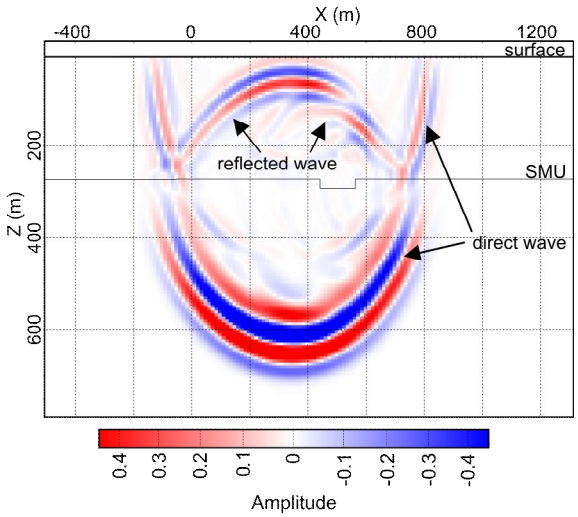

Figure 5.3: Snap shot at 210 ms after source impulse of simulate, propagating seismic wave through the two-layer model.

The synthetic traces created here were then processed to generate the final stacked and migrated images. The traces were corrected for amplitude loss, direct wave was muted, and a NMO correction was applied. The traces were then sorted into CMP gathers and stacked. The synthetic data here did not require any frequency filters or time corrections such as elevation and residual statics. Furthermore, the synthetic traces were also migrated by method of Kirchhoff pre-stacked time migration (PSTM).

5.4. Results

The results from modelling a single karst feature are shown in Figure 5.4 with the CMP stacked sections on the left and PSTM sections on the right. The results from modelling multiple karst features varying in width and depth are shown in Figure 5.5. Parts (a) and (c) are the CMP stacked images for karst of 20 meters in depth and parts (b) and (d) are the PSTM images for karst of 40 meters in depth.

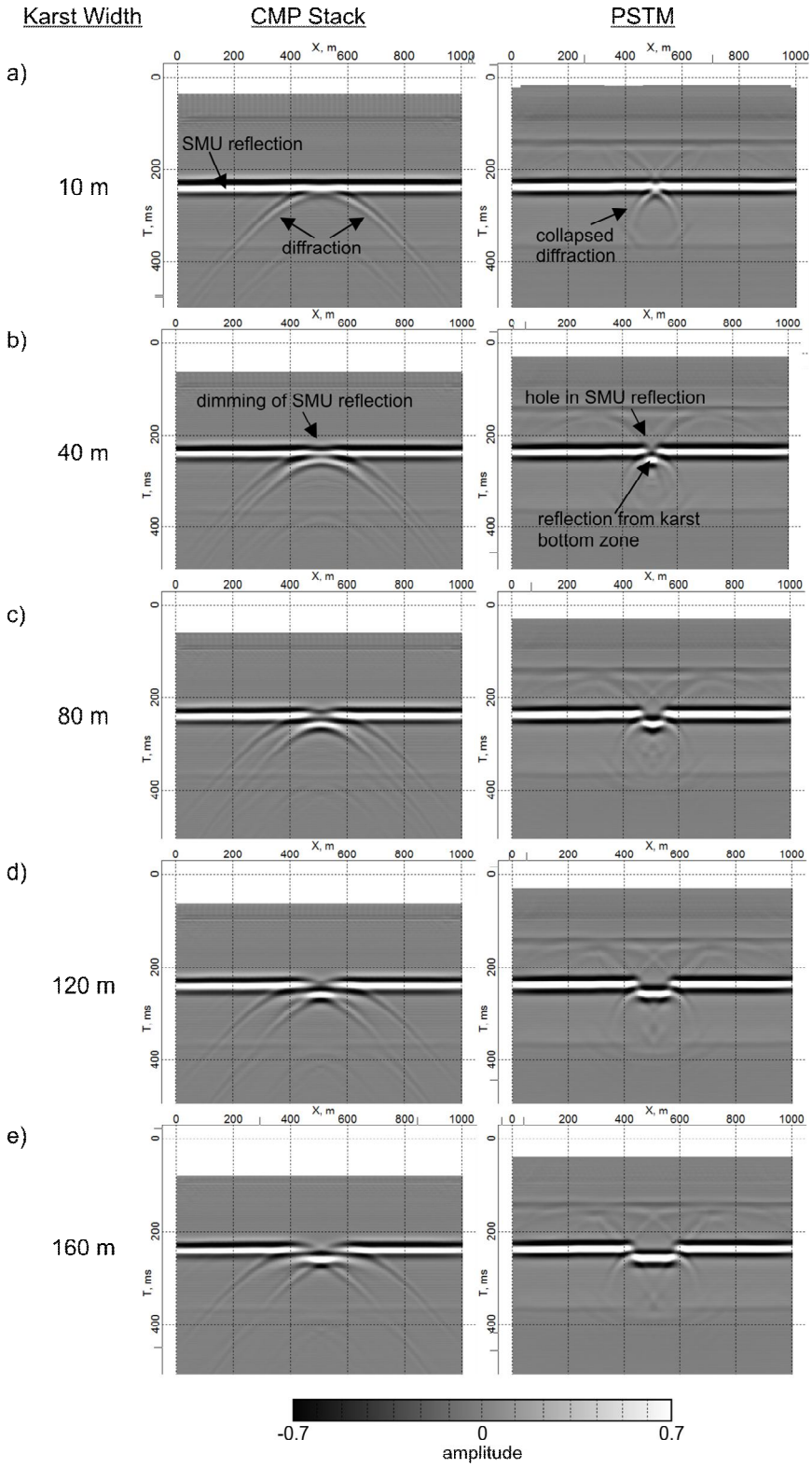

Figure 5.4: Synthetic CMP stacked sections and PSTM sections for the two layer geological of a single simulated karst feature placed along the SMU. The depth of the karst feature was held at 20 m while the width were varied at (a) 10m, (b) 40 m, (c) 80 m, (d) 120 m, and (e) 160m.

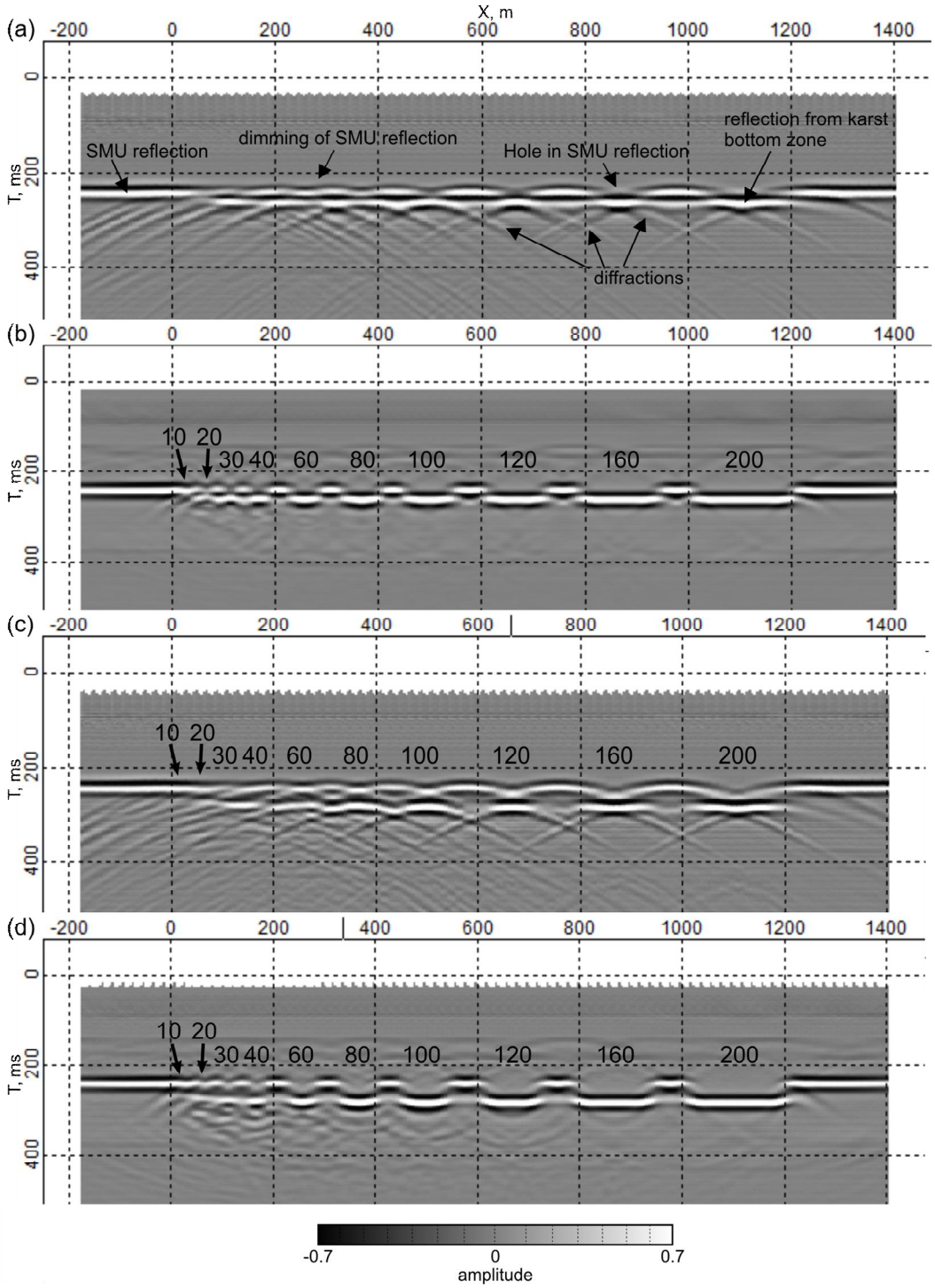

Figure 5.5: Synthetic CMP stacked sections and PSTM sections for the two layer geological of multiple karst features place along the SMU. (a) CMP stacked and (b) PSTM sections of multiple karst features at a common depth of 20 m with widths (denote on the sections) varying from 10 to 200 m. (c) CMP stacked and (d) PSTM sections of multiple karst features at a common depth of 40 m with widths (denote on the sections) varying from 10 to 200 m.

For the CMP stacked images, diffractions were observed form all simulated karst widths and depths. The SMU horizon dimmed over karst for widths of 25 to 160 meters. Widths greater than 160 meters produced a clear break and time sag in the SMU horizon. Features with width smaller than 25 meters were undetectable due to the minimal amplitude variation across the simulated karst region.

Now look at the PSTM images, migration collapsed the diffractions and produced a higher, lateral resolution image. Breaks and subsequent time sags in the SMU horizon were recognized down to a karst width of 25 meters. Dimming of the SMU horizon was not apparent below 25 meters. Moreover, karst features with depths greater than 20 meters were easily seen in the CMP and PSTM images.

5.5. Fresnel Zone and Implication of Migration

Spatial resolution is defined as the minimum horizontal distance needed between two subsurface events at the same reflection level to be independently distinguishable. A reflection that we think of as coming back to the surface from a point is actually being reflected (or more appropriately scattered) from an area or patch of the subsurface. The area of reflection for a zero incident ray could be thought of as a disk. The area outlined by this disk is called the Fresnel zone.

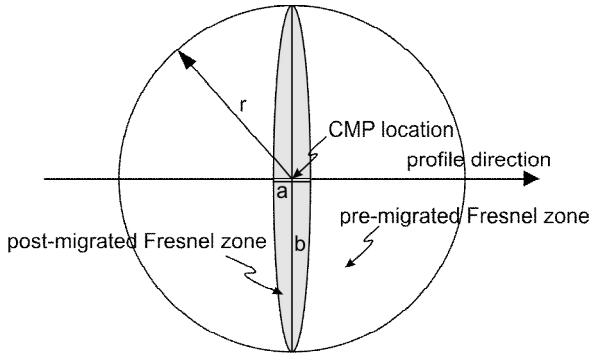

Figure 5.6: Illustrated map view of the pre-migrated Fresnel zone with radius *r* and post-migrated Fresnel zone with minor and major axis *a* and *b* with respects to profile direction.

When migration is performed on 2D seismic data, the Fresnel zone is only minimized in the direction of the seismic profile. Migration transforms the once

circular pre-migrated Fresnel zone to a highly elliptical post-migrated Fresnel zone that has its major axis normal to profile [*A.J. Berkhout*, 1984; *Lindsey*, 1989]. This is illustrated in Figure 5.6.

The radius of Fresnel zone before migration can be described by the equation of

$$r = \sqrt{\frac{z\lambda}{2}} = \sqrt{\frac{z\bar{v}}{2f}} \tag{5-1}$$

where z is the depth to reflector, $\bar{v}$ is the average traversed velocity, λ is the dominant wavelength and thus f is the domain frequency. Take the case of our two layer model, we have a depth of 270 m to the SMU, average velocity of 2000 m/s and signal with dominant frequency 40 Hz. From Equation (5-1) we can calculate the radius of pre-migrated Fresnel zone to be 82 m or a diameter of 164 m.

The post-migrated Fresnel zone is minimized in the direction of the seismic profile. The theoretical limit of the minor axis of the post-migrated Fresnel zone is described by

$$a = \bar{v} / 2f\,, \tag{5-2}$$

and the major axis

$$b = \sqrt{\frac{z\bar{v}}{f}}\,. \tag{5-3}$$

Similarly from our previously proposed (z = 270 m, $\bar{v}$ = 2000 m/s, and f = 40 Hz) the migration collapses the minor axis of post-migrated Fresnel zone a = 25 m and the major axis stays simply at $b = 2r$ = 164 m.

The reflectivity response (i.e. amplitude) record for a CMP location is the response 'average' of the Fresnel Zone area. To follow is a discussion of the roll the Fresnel zone plays on the recorded response of karst valleys and dolines in 2D seismic data.

5.6. Discussion

In the case of a narrow karst valley positioned at the SMU interface as in Figure 5.7, hypothetical seismic lines A, B, and C profile across the valley at

different angles. At the intersection of the lines, all there lines share a common unmigrated Fresnel zone that is circular. At this CMP point, the response in reflection amplitude is the same for the three seismic lines. However, on a seismic section only a slight dimming of the SMU horizon, as seen in the CMP stack of Figure 5.4(b), will be apparent instead of a void. Figure 5.7 shows that there is significant subsurface area of the SMU reflecting the seismic wave even though the CMP location is centered on the narrow valley.

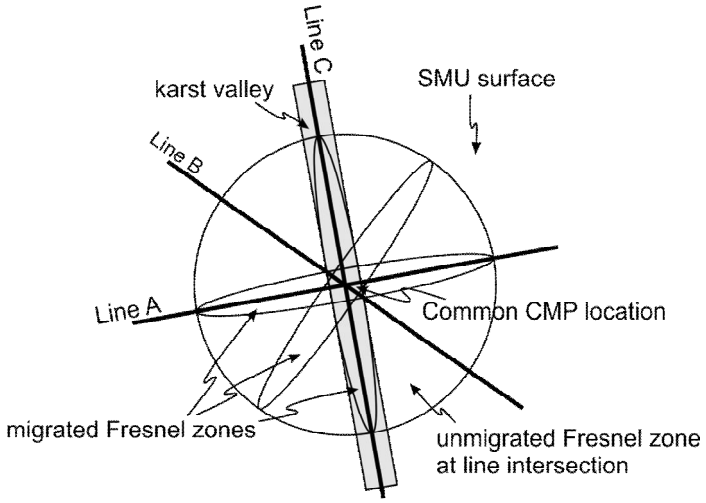

Figure 5.7: Illustrated map view of three seismic lines profiling a narrow karst valley present at the SMU surface.

After migration, each line's Fresnel zone takes on a slender elliptical shape. Profiles B and C will continue to show no clear distinction of the narrow valley as parts of their Fresnel zones still stretch over the background SMU surface. Profile A, however, will show an amplitude 'hole' or break in the SMU (i.e. PSTM image of Figure 5.4(b)) since its migrated Fresnel zone is essentially placed in the void of the valley. Thus, 2D seismic lines that are not perpendicular to the direction of slender subsurface features may not be resolved in seismic data due to the averaging effects of Fresnel zone.

Theory of migrated Fresnel zones and results from the synthetic PSTM images of Figure 5.4 and 5.5 suggest that a hole in the SMU reflector should be visible down to a width of about 25 meters. This is true for seismic lines oriented

perpendicular to karst valleys, and thus as a seismic line is rotated a way from this axis, only a dimming response in the SMU horizon is expected.

The imaging of dolines with diameters less than the size of the unmigrated Fresnel zone in 2D seismic data is problematic, regardless of migration. Figure 5.8 shows an illustration of circular doline smaller than the unmigrated Fresnel zone. Even with migration parts of the migrated Fresnel zone stretch over the SMU surface thus, no break shall be observed in the SMU horizon on a seismic image and only a dimming shall indicate its presence. However, the presence of these small dolines should be more apparent after migration due a great ratio of the Fresnel zone sensing the void caused by the doline.

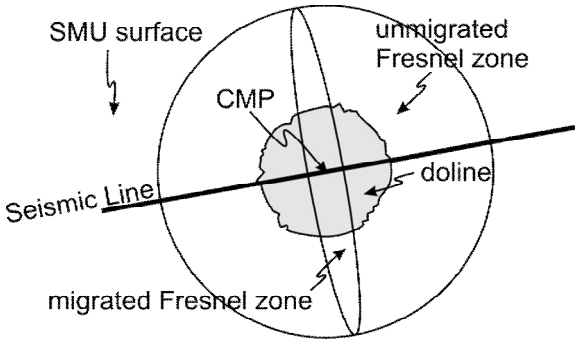

Figure 5.8: Illustrated map view of a seismic line profiling a small doline present at the SMU surface.

In theory, dolines greater than the unmigrated Fresnel zone of 160 meters should be seen as visible break and time sag in the SMU horizon in a migrated image. Those less than 160 meters shall only show a dimming effect; dolines ultimate smaller than 25 meters, the minor axis of the unmigrated Fresnel zone, were considered not to be detectable. A recent abstract by Gray et al. [2011] stated that amplitude dimming due to the presence of dolines was seen over a diameter range of 30-150 meters for the Grosmont formation. This resolution observation of dolines from field data does validate the theoretical range presented here.

5.7. Summary

In summary, small three-dimensional structures such as dolines are poorly imaged in 2D seismic data. It was shown that dolines produce a dimming response in the SMU horizon over a diameter range of 25-160 meters and present a visible break and time sag in the SMU horizon for those of greater diameter. Karst valleys were better imaged than dolines, inherently due to their two dimensional structure. Narrow karst valleys oriented nearly perpendicular to a seismic profile shall be clearly imaged as break and time sag in the SMU horizon down to about a width of 25 meters.

Chapter 6 Rock-physics Modelling of the Grosmont Reservoir

6.1. Overview

The Grosmont reservoir is highly saturated with bitumen. This chapter presents a modern method for modeling a porous rock saturated with highly viscous liquid. Using a combination of a De Ghetto and Cole-Cole Maxwell (CCM) models, and a coherent potential approximation (CPA) effective medium theory, the P-wave velocity of carbonate rocks saturated with bitumen was predicted to vary ~200 m/s at porosity of 22% and across a frequency range of 50 Hz to 1 MHz at temperature of 20ºC. For a porosity of 40% under the same conditions will vary ~700m/s. These results are due to velocity dispersion of the bitumen and would not be apparent when using Gassmann-Biot effective medium theories. The work presented here has implications for future studies to consider a more sophisticated modeling approach when dealing with extra-heavy oil as pore fluid in rock. This work may help solve the problem of unexplained phenomena observed differences in seismic records, sonic logs, and ultrasonic core measurements of velocity.

6.2. Previous Work

Despite rapidly increasing exploration and production of extra-heavy oils worldwide, an understanding of the basic rock physics of this oil in carbonate formation has lagged. There are few studies in the literature that examine seismic wave propagation through heavy oil saturated rocks [i.e. *Batzle et al.*, 2006; *Gurevich et al.*, 2008; *Leurer and Dvorkin*, 2006; *Makarynska et al.*, 2010] of which most investigate clastic environments [except for *Makarynska et al.*, 2010].

Gassmann's [1951] formula describing the static (i.e. zero-frequency) elastic behaviour, due to its simplicity, is popular and extensively used to combine the properties of minerals, rock frame and pore fluid into a single, competent effective medium. Biot's equations [see *Bouzidi and Schmitt*, 2009] attempt to

predict this elastic behaviour with frequency, but due to the additional parameters implementation can be problematic to apply. Although true experimental validation remains elusive [*Batzle et al.*, 2006] Gassmann's formula has been assumed to work well in describing the effects of geological fluids such as brines, gases, medium oils, light oils and condensates on seismic wave propagation. However problems arise in the comparison between high (e.g. laboratory, sonic logging) and low (seismic) frequencies when more viscous fluids, particularly heavy and extra-heavy oils (bitumen), are the pore 'fluid' [*Douglas R. Schmitt*, 1999b]. Gassmann's formula assumes that the fluid has a shear modulus of zero. The shear modulus of extra-heavy oil is not zero and varies with both temperature and frequency [*Batzle et al.*, 2006]. This can have a significant impact on the observed effective moduli and acoustic wave speeds of a saturated rock. In an attempt to better incorporate this effect, the CPA effective medium theory [*Berryman*, 1980; *Mavko et al.*, 1998] is explored by modelling (Figure 6.1). This approach may provide a means to correlate velocity measurements at different frequencies from ultrasonic down to seismic.

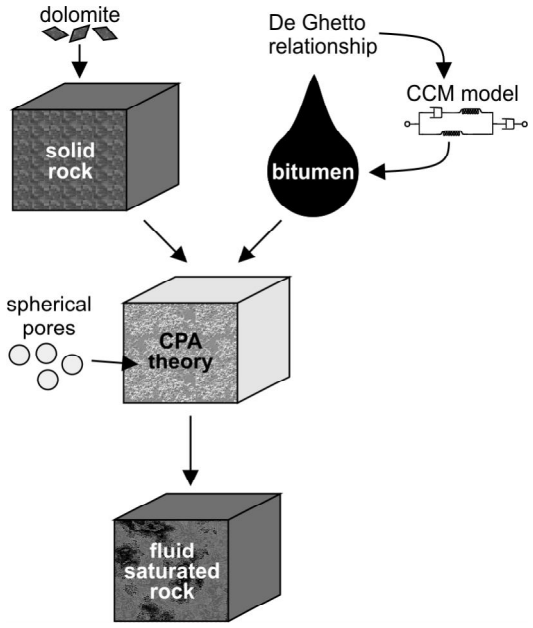

Figure 6.1: Schematic diagram of the rock-physics model used for this study.

6.3. Method

To calculate the viscosity for dead extra-heavy oil, an empirically derived model by De Ghetto et al. [1995] was used to representative bitumen. They described the viscosity model for dead, extra-heavy oil as

$$\log\cdot\log(\eta+1) = 1.90296 - 0.012619\cdot API - 0.61748\cdot\log(\tfrac{9}{5}\cdot T + 32). \quad (6\text{-}1)$$

where η is viscosity of the oil, degrees *API* gravity is characteristic of oil density and *T* temperature is in degrees Celsius. Grosmont bitumen was measured by Zhao [2009] to have a very low API gravity of 5º to 9º. A viscosity-temperature profile was developed the De Ghetto model for API gravity 6º. This estimate viscosity-temperature profile does agree with measurements made by Zaho and Machel [2009] reported the viscosity of Grosmont bitumen at 10^7-10^8 cP at 20 ºC as shown in Figure 6.2. It is possible that compositional effects, such as those produced by biodegradation of Grosmont bitumen [*Zhao*, 2009], will move the predicted viscosity away from the De Ghetto relationship presented here.

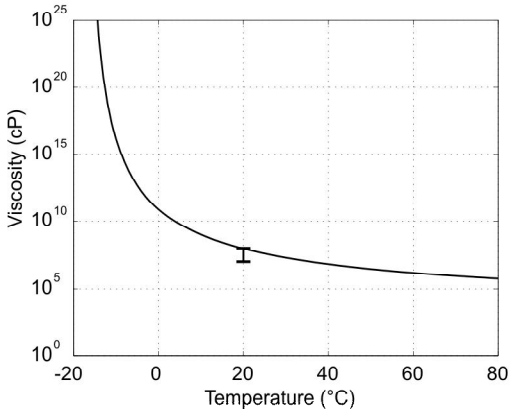

Figure 6.2: Modeled viscosity-temperature profile of Grosmont Bitumen. The error bar reflects the viscosity measurements at 20ºC by Zhao and Machel [2009].

To approximate the rheology of extra-heavy oil, this study used a visco-elastic CCM model developed by Gurevich et al. [2008]. The CCM model denotes the frequency dependent, complex shear modulus μ_f as

$$\mu_f = \frac{\mu_\infty}{\frac{1}{(-i\omega\tau)} + \frac{1}{(-i\omega\tau_1)^\beta} + 1} \qquad (6\text{-}2)$$
$$\tau = \eta / \mu_\infty$$

where ω is the angular frequency of an acoustic signal, τ and τ_1 are relaxation times of two characteristic points on the continuous relaxation spectra, β is an adjustable parameter and μ_∞ is the storage modulus, real part of the complex shear modulus, of a material at high frequency. The CCM model was employed with parameters of μ_∞ = 1.02 GPa, β =0.2 and tau ratio τ/τ_1 = 10. The viscosity determined at different temperatures from the De Ghetto model was fed into the CCM model. The complex shear modulus was calculated over a temperature range of 0 - 240 ºC and frequency range 0.1 - 10^6 Hz. The results are shown for the storage modulus (i.e. the real part of the complex shear modulus) in Figure 6.3.

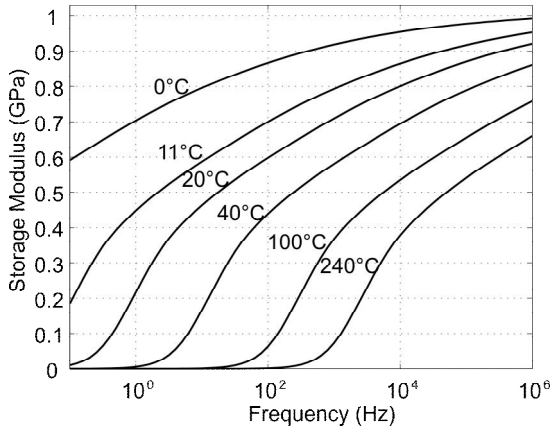

Figure 6.3: Storage modulus temperature-frequency dispersion of the modeled Grosmont bitumen.

Next, CPA theory was used to calculate the effective bulk and shear moduli of our saturated rock by combing the elastic properties of dolomite and the modeled Grosmont bitumen. The CPA theory [*Berryman*, 1980] for spherical pores was expressed by a system of two equations for solving effective K^* and shear μ^* moduli of a saturated rock

$$\varphi(K_f - K_*)P^{*f} + (1-\varphi)(K_m - K_*)P^{*m} = 0$$
$$\varphi(\mu_f - \mu_*)Q^{*f} + (1-\varphi)(\mu_m - \mu_*)Q^{*m} = 0 \qquad (6\text{-}3)$$

where φ is porosity, K_f and μ_f are the bulk and shear moduli of the pore fluid, K_m and μ_m are bulk and shear moduli of the matrix material, and P and Q are invariants of the so-called Wu tensor . For the simplified case of spherical pores, the Wu tensor can be solved explicitly as

$$P^{*i} = \frac{K_* + 4\mu_*/3}{K_i + 4\mu_*/3}$$
$$Q^{*i} = \frac{\mu_* + F}{\mu_i + F} \qquad (6\text{-}4)$$
$$F = \frac{(\mu_*/6)\cdot(9K_* + 8\mu_*)}{K_* + 2\mu}$$

where i is interchangeable for f and m. Solving the coupled equations from Equation (6-3) was performed by an iterative approach.

Recall that the Grosmont reservoir, members C and D, comprised of primarily of dolomite material with very little quartz or clays. Therefore the solid rock portion of our rock-physics model was assigned as dolomite mineral grains with properties of K_m = 94.9 GPa, μ_m = 45.7 GPa, and ρ_m = 2795 kg/m^3 (see Table 2.2). The bulk modulus of the bitumen used was K_f = 3.02 GPa. If there was a need to represent other minerals or particles in the rock, a Reuss-Voigt-Hill average would have been utilized [see *Xu and Payne*, 2009].

6.4. Results

If the Grosmont reservoir resides at a temperature of 11 ºC [reported by *Zhao*, 2009], then Figure 6.4 is an example of the modelled response of acoustic velocity varies against porosity at seismic frequencies (50 Hz). The reported reservoir porosity of the Grosmont formation is, on average, 22% [see Table 1 from *Jiang et al.*, 2009] and can be as high as 40% [*K Barrett and Hopkins*, 2008]. Thus, the temperature-frequency dispersion of acoustic velocity at constant porosity of 22% and 40% are shown in Figures 6.5 and 6.6, respectively. From

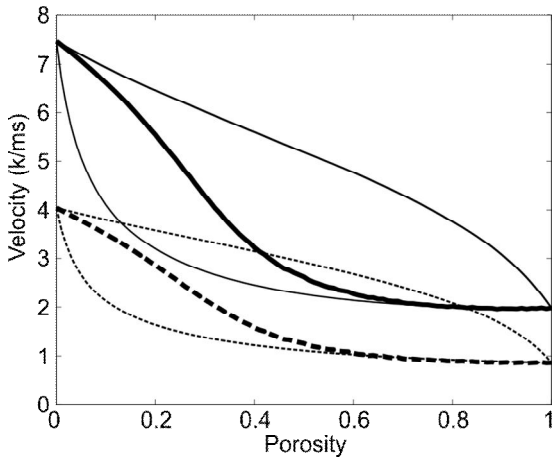

Figure 6.4: Acoustic velocity of P-wave (solid lines) and S-wave (dashed lines) against porosity for the modelled Grosmont reservoir at 11 ºC with a 50 Hz signal. CPA modelled results are the thick lines and the rigours upper and lower Hahin-Strikman bounds are the thin lines.

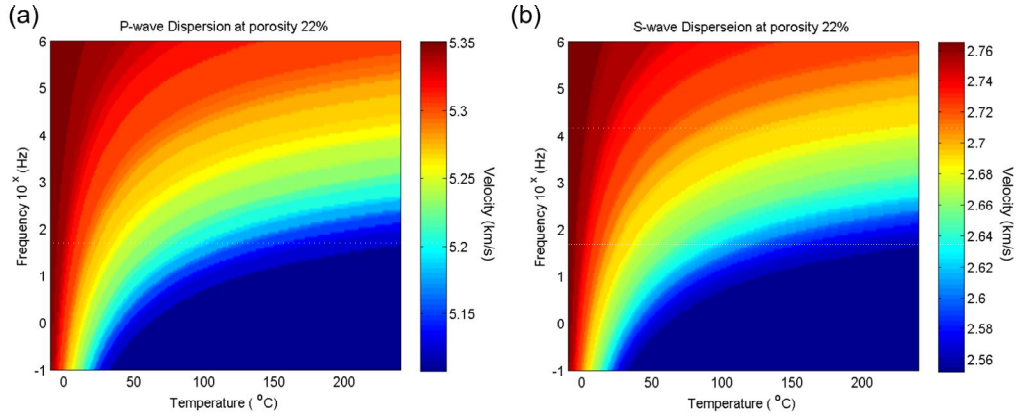

Figure 6.5: Modelled temperature-frequency dispersion of P and S wave velocity at 22% porosity.

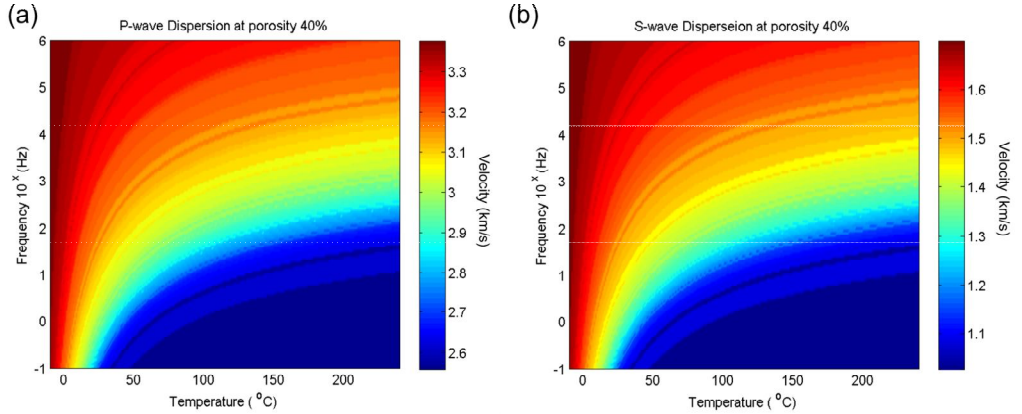

Figure 6.6: Modelled temperature-frequency dispersion of P and S wave velocity at 40% porosity.

Figures 6.4, 6.5 and 6.6, we see that porosity has the strongest influence on wave speed in our model. The dispersion relations from these figures are as follows:

- An increase in porosity results in a decrease of wave velocity.
- An increase in temperature results in a decrease of wave velocity.
- An increase in frequency results in an increase of wave velocity.

6.5. Discussion

There were two general trends seen in the data, a temperature increase or a frequency decrease resulted in a velocity decreases in both P and S waves. This dispersive effect of temperature and frequency on velocity is significant, varying over 200 m/s for both P-wave and S-wave velocity at a porosity of 22%, and over 700 m/s at 40% porosity. For high porosity, the Grosmont reservoir should yield more to the viscoelastic effects of the bitumen, which ultimately transmit seismic energy slower. As such, care should be taken in applying the Gassmann theories, because it will tend to under predict wave velocity for Grosmont reservoir conditions. The model developed here will be applicable to tie acoustic measurements made on Grosmont core to sonic logs to seismic sections.

On a final note, it is known that a network of large vugs, intercrystalline pores, and fractures dominates the pore structure of the Grosmont reservoir [*K Barrett and Hopkins*, 2008; *Ping and Machel*, 1995; *F. Theriault*, 1988]. It would be interesting to modify CPA scheme to account for the effects of binary pore or multiple pore structures to represent the reservoir more accurately. Such an idea was applied in the recent study by Makarynska [2010] on Uvalde heavy-oil carbonate rock from Texas, U.S.A.. Further work is needed to fine tune CPA theory to include pores with aspect ratio.

Grosmont bitumen at reservoir temperature of 11 ºC is immobile due to its high viscosity of ~6.7×10^{8} cP (predicted by the model), thus heating of the reservoir is required for the insitu production. Because of the strong temperature dispersion seen in the elastic properties of our rock-physics model, there is potential application for time lapse monitoring of heat distribution associated with

reservoir production. It is suggested that the higher the reservoir temperature, the softer the rock is elastically and the lower the reflective amplitude. If seismic data is collected before and after the heating (i.e. steam injection) of the Grosmont reservoir, a decrease in reflection amplitude should be noticed in the latter dataset.

6.6. Summary

The use of Gassmann-Biot effective medium theories to model the Grosmont reservoir may rectify to highly inaccurate results due to the significant dispersive effects of bitumen at reservoir conditions. The more advanced theory of CPA showed that P and S waves varied over 200 m/s at 20% porosity and 700 m/s at 40% porosity across a frequency range of 0.1 - 10^6 Hz. Furthermore, the temperature dispersion seen within the model suggests that time-lapse monitoring of recovery efforts with seismic surveys is achievable. The results of this study are said to be preliminary as there is no direct comparison to core measurements.

Chapter 7 Interpretation

7.1. Overview

During the 1980's a succession of seismic surveys were collected as part of the AOSTRA project in the Grosmont area. To our knowledge, no integrated interpretation of the data was ever carried out. This section first presents interpretation of the geology at a regional scale of survey series A and then further investigates the local scale geology of survey series B, C, D and E. Interpretation of the seismic and well data was performed with the seismic interpretation software of Petrel™.

From the interpretation of the high-resolution seismic data, the SMU was defined as a mature karsted surface with dolines, karst valleys and large ridge-valley complex. This large ridge-valley theme present at the SMU was controlled by folding of Devonian aged formations before erosion. Moreover, it was noticed that most of the doline features seen in the seismic data were contained within the extent of the valley. It is suggestive that that the valley may have been a karst structure called a Poljie. In other areas, the karst plain, the SMU surface is relatively flat and continuous with minimal presence of karts structure.

7.2. Regional Interpretation

Regional scale interpretation consisted of interpreting the long regional 2D seismic lines of survey series A. Before jumping into the interpretation, a quick discussion data quality of the regional data is important.

Data quality of the regional seismic lines was poor. The acquisition details for the two profiles were given in Table 2.1. Generally, the relatively large spacing of the source (80 m) and receiver (16 m) points as well as the overlapping receiver group length (36 m) made imaging of the shallow SMU and the overlying Mesozoic and Quaternary structures problematic. It was not apparent what the purposes of these surveys were as the charge sizes were relatively small and higher frequency geophones (30 Hz) were employed. These earlier workers

may have been attempting to reduce surface wave (ground roll) noise contamination, but as consequences of their actions, they also significantly attenuated reflective signal. Figure 8.1 shows the attenuation response of the receiver array used during acquisition of this seismic data. By rule of thumb [*Andrew Pap*, 1983] a horizon of interest should not be attenuate more than -6 db. This means that the seismic response of a shallow Mesozoic horizon (magenta line), and SMU horizon (green line) should be left of the black line indicate on Figure 8.1. The record reflection from the SMU was attenuate approximately by -9 db. On a further note, the data quality varied between the two lines also, with the south line generally having better responses. This may be related to near surface conditions as the quality of both source strength and signal receptions is degraded in 'muskeg' marsh zones. These seismic lines may not be useful for the extraction of seismic attributes, such as amplitude, at the SMU and shallower zone because of poor signal to noise ratio. However, stratigraphic mapping of these shallow events was possible.

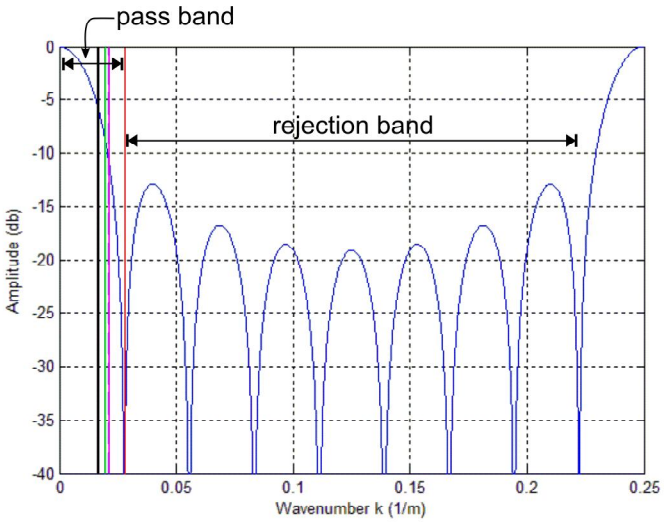

Figure 7.1: Attenuation response of the receiver array implemented by survey series A (blue line). The calculated attenuation response for a reflected wave from a shallow Mesozoic horizon and the SMU horizon are shown by the magenta and green line, respectively. The red line indicates the attenuation response for ground roll.

The data quality varied laterally too across both lines; particularly disappointing is the poor quality at the east side of the North Line. Locations

where shot points were lost due to surface conditions (probably lakes) were apparent as triangular zones from the surface in the final seismic images where the data beneath could not be collected. That said, however, the data quality allows for generally good interpretation towards the west.

The final North (A-01) and South (A-02) processed profiles with the stratigraphic interpretation superimposed is shown in Figure 7.2 and 7.3 respectively, but this small reproduction is unsatisfactory for these 40 km long profiles. The seismic sections display only the upper 1 second of two-way-travel time. The full images can be accessed as part of the digital accessory data.

As noted above, few wells penetrate below the SMU of which only a handful reached deeper into the Devonian section. Of these, few reached into the PCU. Commercial logs for some of these deeper wells (Canadian Stratigraphic Service Ltd.) were obtained and these were able to assist in relating the seismic responses to the expected geology. Only one well had deep sonic and density logs to allow for the calculation of a synthetic seismogram using the seismic wavelet extracted from the data. These constraints allowed for identification of the major reflectors in the sequence and the subsequent interpretations of Figures 7.2 and 7.3. The interpretation presented here remains somewhat preliminary as minor local adjustments and further reconciliation between the North and South line is necessary.

Broadly, both profiles display the gross structure of the region, the PCU up through the Paleozoic sediments, gently dipping to the west. The SMU surface was nearly flat over both lines lying at just below 200 ms. The Paleozoic (primarily Devonian) section thickened from east to west as expected. The subcropping of Devonian units at the SMU was apparent with the Nisku Formation subcropping to the east and the Grosmont to the west.

The trend of Devonian Leduc reefs was also apparent in the east section of the profiles. Evidence for these comes from time pullup of underlying horizons due to the higher velocity within the reefs relative to the surrounding sediments and the occasional multiple generated by the strong contrasts in material properties. One interesting observation concerning these is a possible rapid

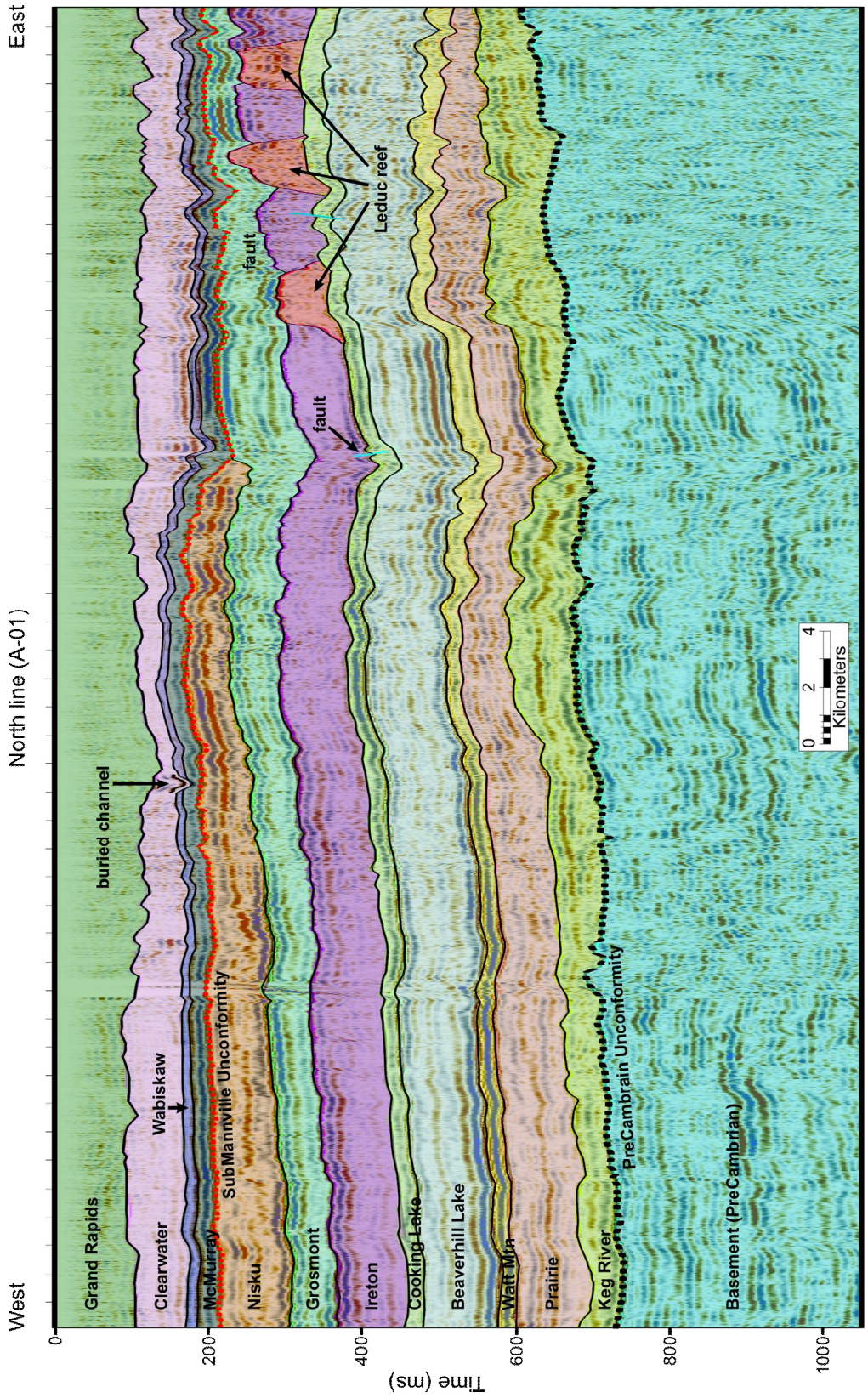

Figure 7.2: Final processed section of the North regional line (A-01) with interpreted lithologies superimposed.

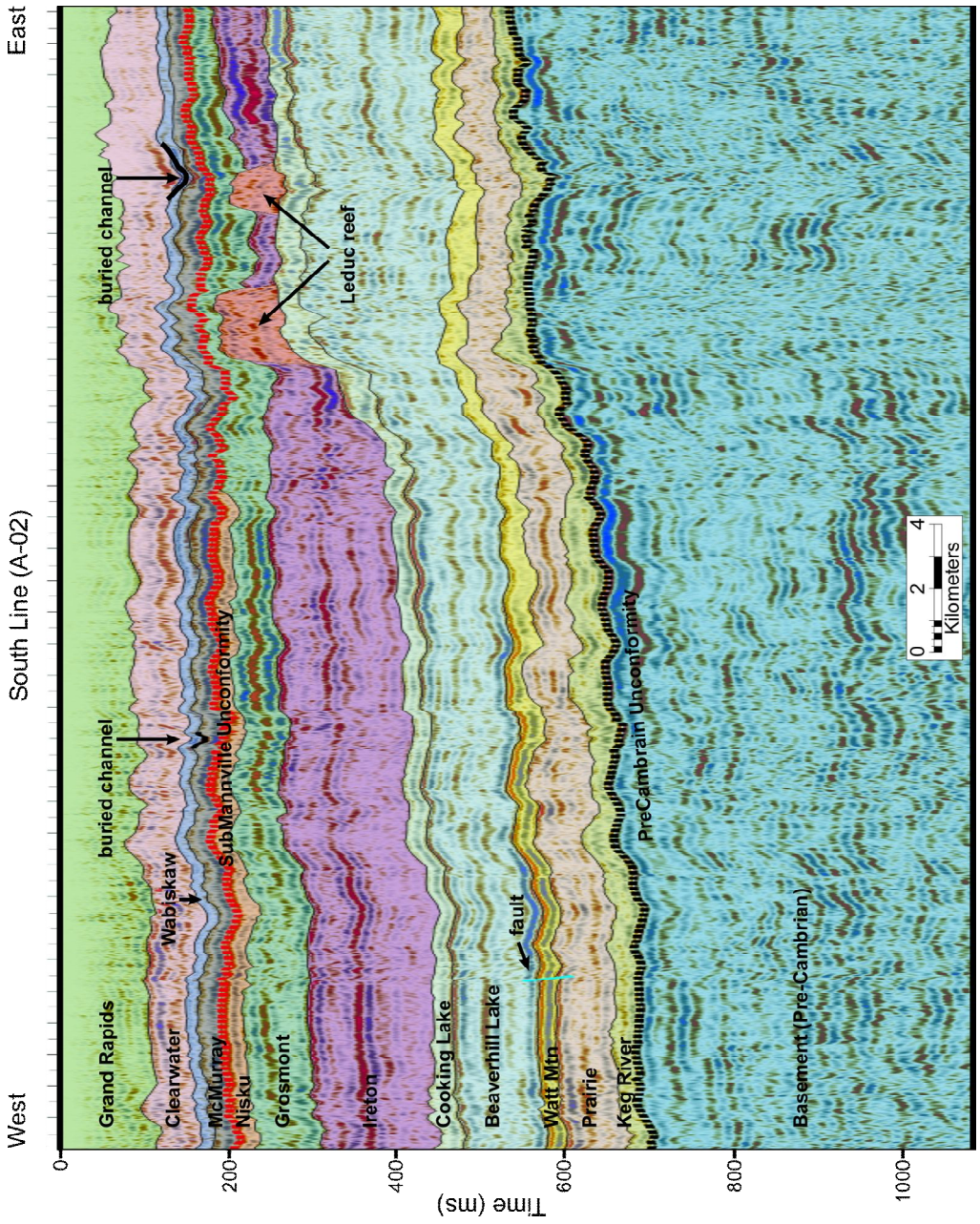

Figure 7.3: Final processed section of the South regional line (A-02) with the interpreted lithologies superimposed.

change in the elevation of the PCU and the overlying formations up to the level of the Cooking Lake Platform upon which the reefs are supported. This might argue for some fault control on the location of these reefs. The general structure appears to agree with the interpretation of well logs and other geological studies [*Ing*, 1985].

There were no clear and obvious faults seen within these images. However, there does appear to be evidence for at least surface lineations that strike both SE-NW and SW-NE [*Pana and Waters*, 2001]. In the region immediately to the NE of this study, high resolution magnetic survey features indicative of faulting both in the sediments and within the metamorphic basement [*Airo and Wennerström*, 2010; *Best et al.*, 1998]. That said, the basement reflector may suggest a smoothly undulating surface that could be consistent with minor faulting below seismic resolution limits [i.e. *Hope et al.*, 1999]. Continuing interpretations of these data may consider larger structural forcing, such as the development of topographic forebulges that may have influenced stress regimes and subsequent breaking of the rocks during initial formation of the Western Canada foreland basin [i.e. *DeCelles and Giles*, 1996].

Buried valleys were also apparent in both seismic sections despite the poor imaging conditions imposed on such shallow features by the data acquisition. Two of the more prominent valleys, labelled in Figure 7.3, appeared to breach the SMU in the South regional line. Such features are of concern to oil production as their expected high permeabilities and porosities could provide preferred pathways for fluid flow away from their Nisku of Grosmont formations.

7.3. Local Interpretation

The local area was defined as the square boundary (dash-dot line) denoted in Figure 7.4 that encompassed the high-resolution seismic surveys of B, C, D and E. In this section will cover well tying to the seismic data and the integrated interpretation of the seismic data.

The tying of geological structure to the seismic data occurred at well location W-01 where well logs of sonic and density were available. The VSP at this location was used to assist in the interpretation and well tie. Unfortunately the original VSP data was unaccounted for and, hence, not available direct reanalysis. However, on the left side of Figure 7.5(a) shows a portion of the raw VSP data as extracted from the images Schacter [1985]. This imaged VSP data provided constraints on seismic travel times that were important both in assisting with the

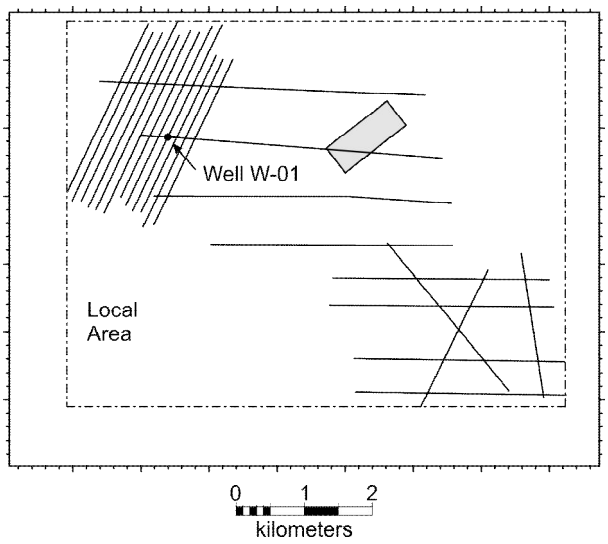

Figure 7.4: Map of local area defined by dash-doted box for the interpretation at local scale.

processing of the seismic data and particularly for the interpretation of the profiles. The one-way travel time of the VSP (blue dots) was plotted with gamma log (green line) of the well in Figure 7.4(a) for the interpretation of the individualGrosmont members. According to this data, the SMU resides at a depth of 260 m that corresponds to a two-way seismic travel time of about 250 ms. In addition to this data at well W-01, sonic and density logs was ran over a very limited depth range of 180-400 m. These logs were used to generate a synthetic trace that denoted the SMU as the strong negative peak at 260 m (Figure 7.4(b)). This synthetic trace was tied to seismic line C-09 and was the only available well tie in the area. Despite the limitations of the VSP and well log data, the four different seismic surveys of B, C, D and E were tied together at the SMU horizon[3].

The VSP data was also instrumental in developing an appropriate time-to-depth velocity model that allowed for conversion of the observed travel times for the various horizons into true elevations. The model is summarized in Table 8.1 with Figure 7.5 showing how the model varies in space over the local area of the high-resolution seismic lines.

[3] It is important to note that the ties between the data sets were complicated by a polarity reversal of the survey series C data series relative to the other data sets. Once this discrepancy from the data acquisition was noted, the different data sets tied well.

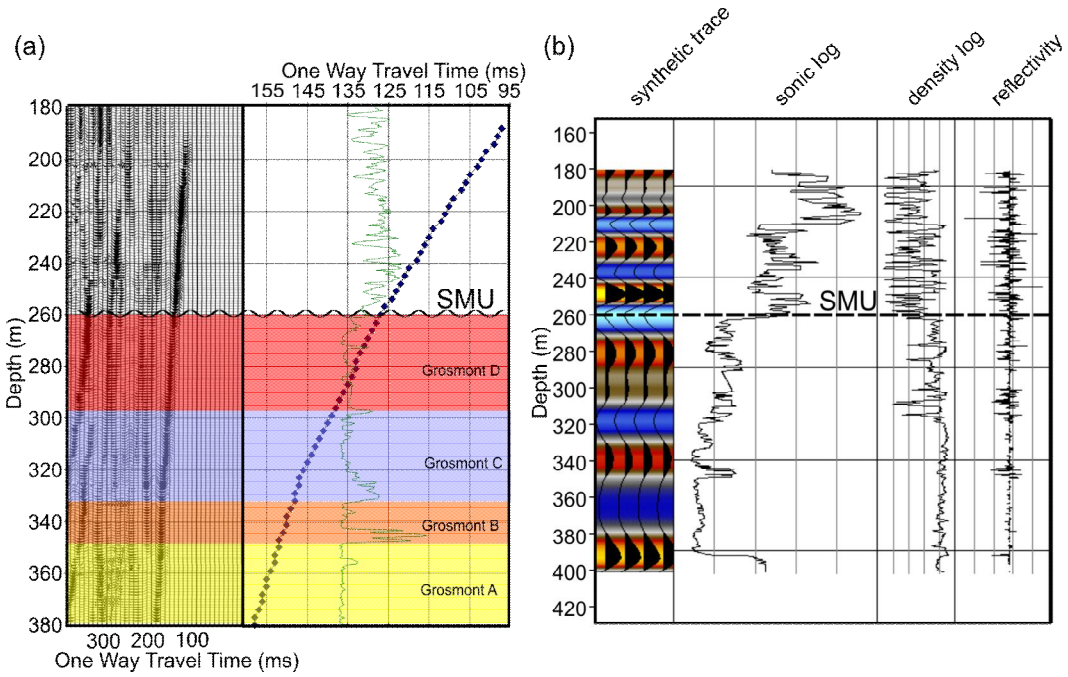

Figure 7.5: (a) Left panel shows the image of VSP from Schacter [1985] for well location W-01. The right side shows the one way travel time of the VSP data (blue dots) superimposed on the gamma log. (b) Synthetic trace generated from the sonic and density log.

Table 7.1: Summary of the velocity model used to convert two-way times to elevations.

Top Surface	Bottom Surface	Velocity Model	Comments
Seismic Reference Datum: 518 m.a.s.l.	Horizon 1	Constant interval velocity: 1720 m/s	Replacement velocity
Horizon 1	Horizon 2	Constant interval velocity: 2220 m/s	Determeind from well W-01 VSP
Horizon 2	Wabiskaw	Well checkshot - Time to depth relation	Velocity surface made from checkshots
Wabiskaw	Grosmont D (SMU)	Well checkshot - Time to depth relation	Velocity surface made from checkshots
Grosmont D (SMU)	Lower Ireton	Constant interval velocity: 3020 m/s	Determeind from well W-01 VSP
Lower Ireton	Horizon 6	Constant interval velocity: 4900 m/s	Determeind from well W-01 VSP
Horizon 6	Horizon 7	Constant interval velocity: 5400 m/s	No data - reasonable estimate
Horizon 7	Horizon 8 (Basement)	Constant interval velocity: 6000 m/s	No data - reasonable estimate

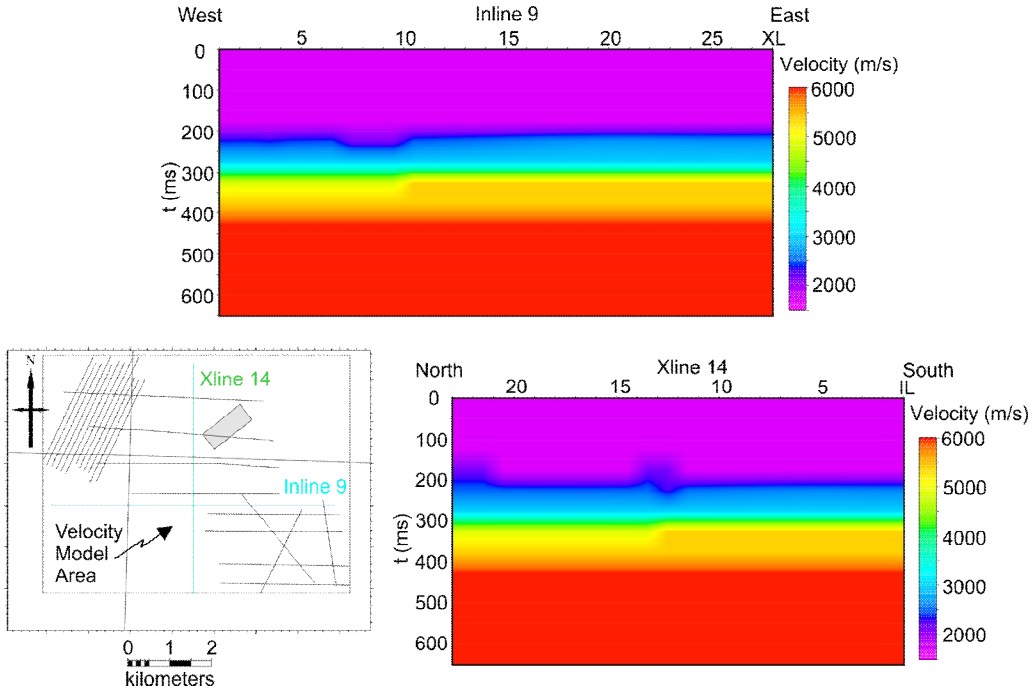

Figure 7.6: Displaying inline and crossline profiles of the generated velocity model.

We selected a few prominent events in the seismic data for interpretation, however, the general lack of appropriate logs as well as the paucity of boreholes that are deeper than the Grosmont complicates the assignment of seismic horizons to various geological tops. The VSP data of Figure 7.5(a) was critical to obtaining approximate lithological ties above the SMU horizon while lithologies deeper in the seismic section were determined by comparison to the interpreted regional lines of section 7.2. Six events within the seismic sections (Figure 7.7) were selected for mapping and further analysis, they are Horizon 1 (likely representative of the behaviour of the Grand Rapids Formation), the Wabiskaw event, the SMU (Grosmont D), the Lower Ireton event, Seismic Horizon 5 (probably associated with the top of the Prairie evaporate), and finally, the PCU (Basement).

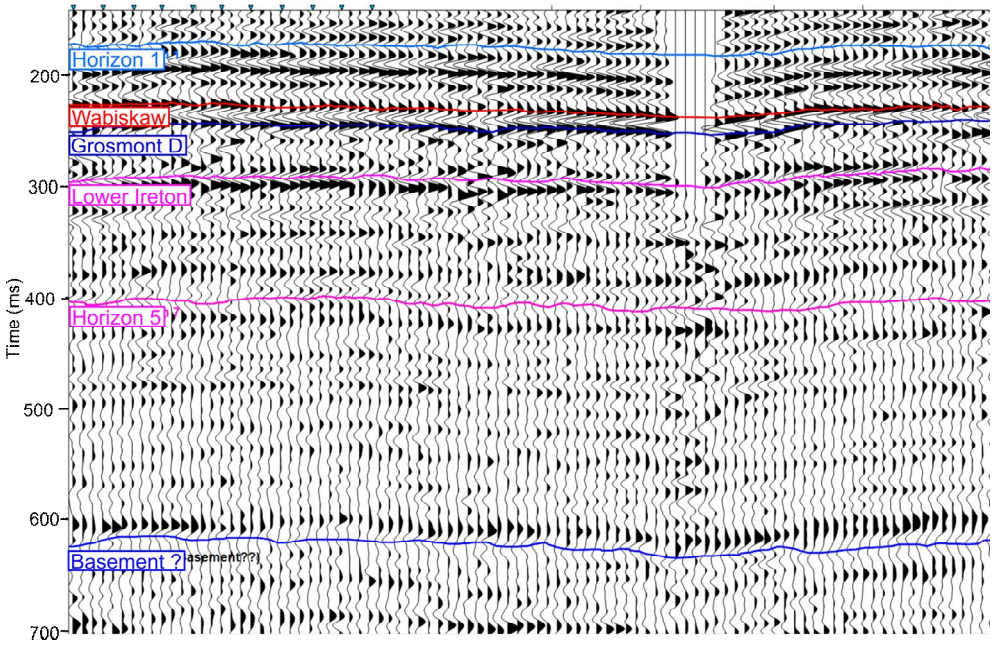

Figure 7.7: Portion of seismic line E-01 showing the six chosen horizons for mapping and further analysis.

Once the times of these various horizons were picked within the interpretation software, they were interpolated and the results smoothed to create structure maps in time domain. They were then turned into of elevation from mean sea level by using the velocity model of Figure 7.6 to implement a time-to-depth conversion. Figure 7.8 (a) and (b) shows the interpreted SMU surface in time and elevation from the integrated seismic profiles. Figure 7.8(c) shows the SMU surface as determined solely from the well tops. The well top map was cut from the larger geological model presented in back section 3.4. The differences between the SMU surface as predicted from the seismic data and those from well tops appear to be quite different. These maps show that the well log information does not properly represent the topography of the SMU surface.

The well elevation map did have a ~30 wells sampling the SMU surface but their positions were highly biased to the actual pilot sites. In comparison, the seismic data does show substantially more detail. Chiefly, the SMU varies on a smaller scale than the overall spatial sampling of well data, thus the well elevation map fails to capture the topography of the SMU in a sufficient manner.

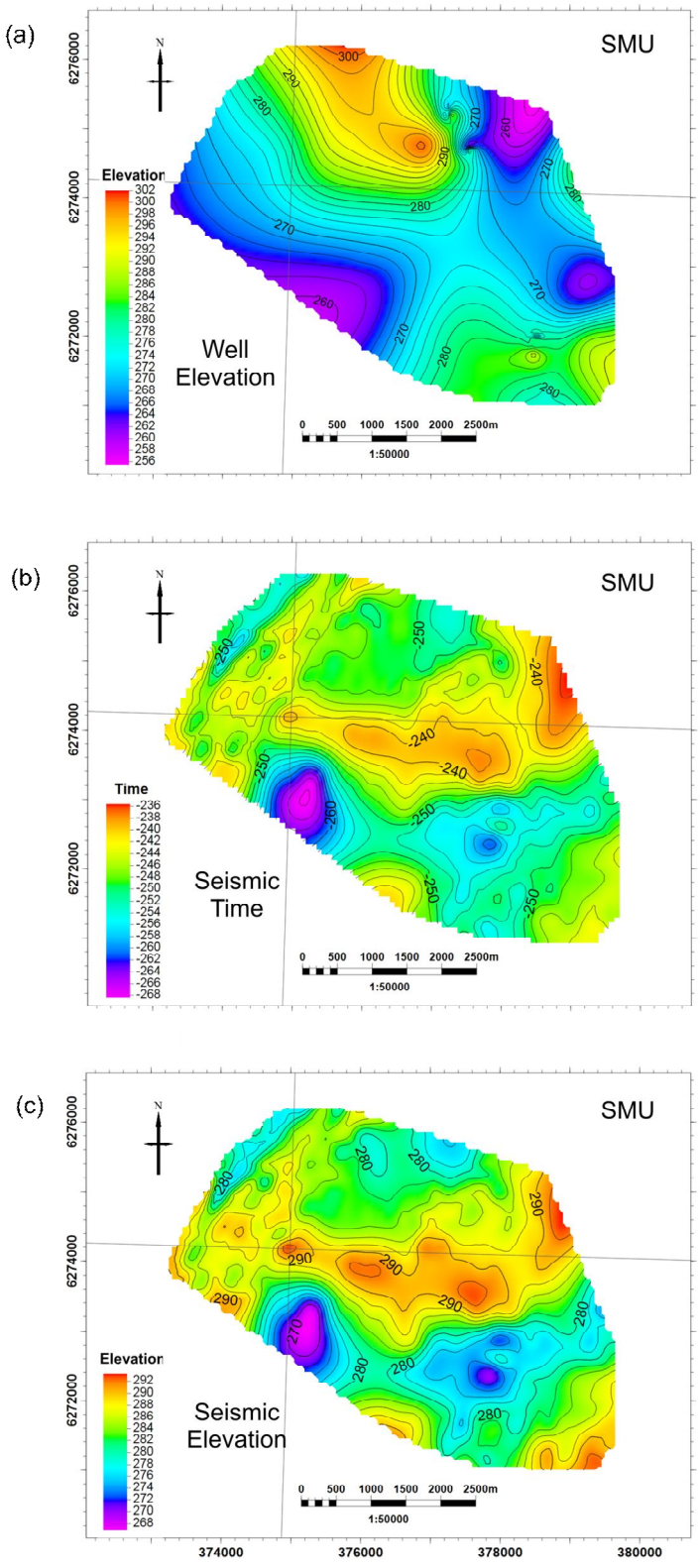

Figure 7.8: Comparision of surface maps for the SMU of generated from (a) well elevation data, (b) seismic data in time and (c) seismic data in elevation.

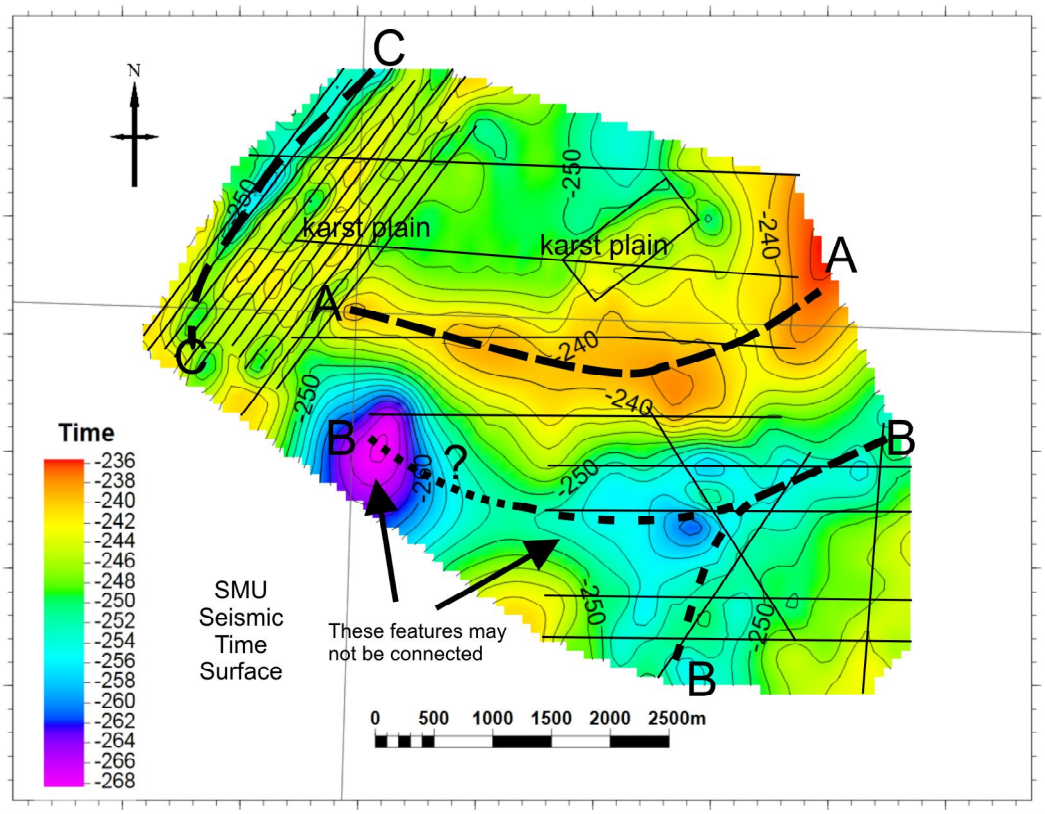

Figure 7.9: Seismic time surface of the SMU with interpreted structures of A, B, and C. Black lines indicate the high-resolution seismic surveys.

Given the importance of the SMU, the first priority is to examine its structure. This is followed by examinations of the deeper and shallower seismic events in order to see if there are any correlations. Deeper correlations could indicate geological structures such as faults or folding of the Devonian aged formations have influenced the topography of the SMU. Shallower correlations may be indicative of control of the karsted surface on the overlying Mesozoic sedimentation.

The time surface of Figure 7.8(b) is reproduced at a larger scale in Figure 7.9. There were two primariy E-W trends observed in this image, ridge ‘A’ and a valley ‘B’. Both the valley and ridge were measured up to a kilometre width. Time difference from the highest point of the ridge to the lowest point of the valley was about 30 ms of two way time. This suggested that topographic variations are on the order of 35 m.

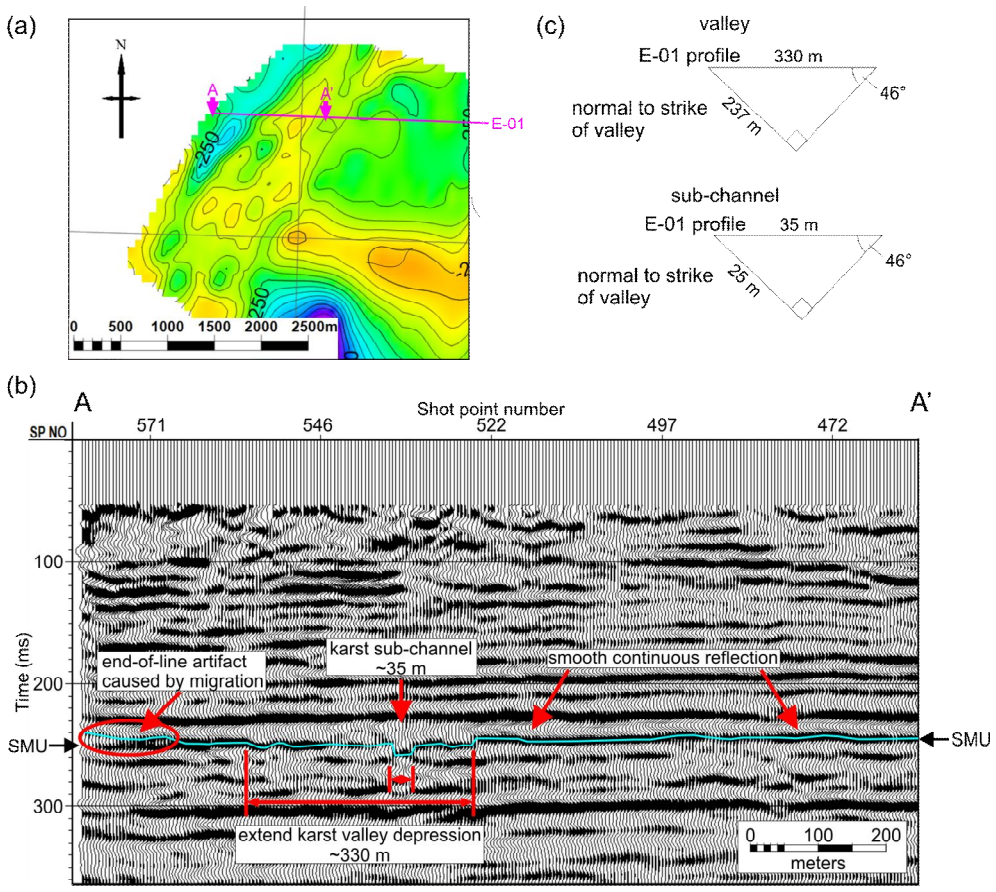

Figure 7.10: Feature C, an imaged karst valley in the seismic data of (a) time map of the SMU, (b) portion of sesimic line E-01 profiling A-A' and (c) geometry of apparent width and true width of karst valley and sub-channel.

Feature 'C' appears to be a small linear valley running in a NE-SW alignment. Strong evidence of this narrow valley was observed in line E-01 that profiled somewhat perpendicular to this structure. The response of this narrow karst valley is clearly seen on the seismic section displayed Figure 7.10 by a shift later in two-way travel time of the SMU. The valley was estimated to be about 237 meters wide. Further analyzing the valley, one can observe a secondary feature of what appears to be a 25 m wide channel (Figure 7.10) possibly cut into the bottom of the valley. Unfortunately, this small channel would not be observable in any of the C series data because of the orientation of their profiles. Moreover, this NE-SW orientation of feature 'C' may be subparallel to the expected joint trends in the Grosmont formation [*Jones*, 2010]. Evidence for this feature was support on the ties between the series C and series E data sets.

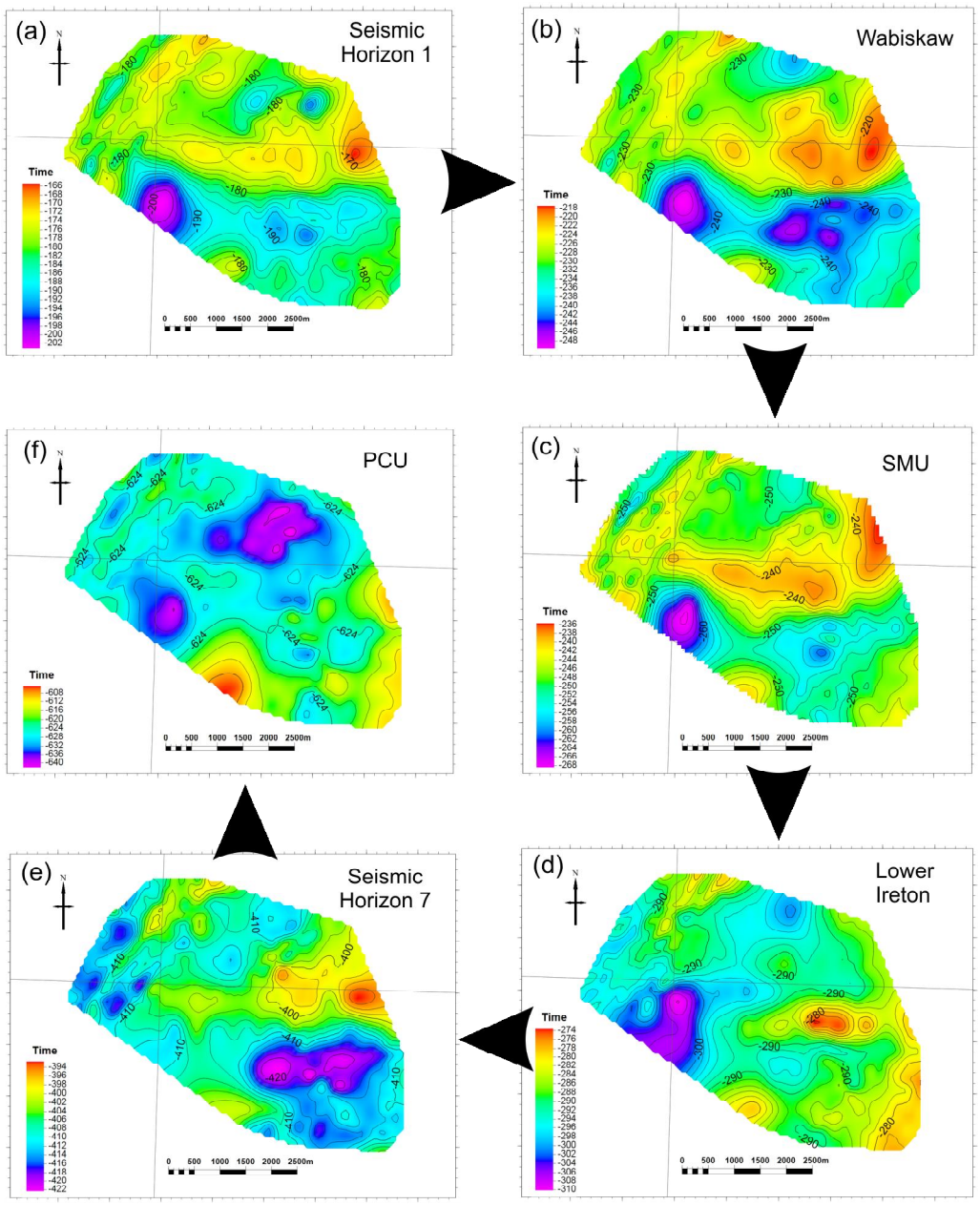

Figure 7.11: Comparision of the surface maps in time domain for the (a) Mesozoic seismic horizon 1, (b) Mesozoic Wabiskaw, (c) SMU, (d) Paleozoic Lower Ireton, (e) Paleozoic seismic horizon 7 and (f) PCU. Arrows denote the progression of the panels with subsecently increasing depth.

A comparison of surface structure of SMU against the other five interpreted horizon is shown in Figure 7.11 of which are compared in sequential order from shallow to deep in the earth. One interesting observation is that the E-W ridge-valley trend of feature 'A' and 'B' appears in the lower Paleozoic lithologies of the Lower Ireton surface and seismic horizon 7 surface (near the

Prairie Evaportie). This correlation indicates that structures 'A' and 'B' seen at the SMU were geologically controlled by tectonic activity imposed the Devonian aged formations. However, this trend does not appear at the top of the metamorphic basement. This would suggest that the Devonian aged formations might also have displaced by faulting along the PCU. Furthermore, the main ridge-valley theme continues into the shallower Mesozoic horizons of Wabiskaw and Seismic Horizon 1 and the topographic relief from ridge high to valley low dissipates as one moves towards shallower horizons. This is likely due compaction effects within the Mesozoic sediments. Due to the variation in thickness and the compatibility of more shale rich sediments in the valley of sequence, loading by later deposits will give rise to spatially varying amounts of compaction. Both the thickness and structure of the sequences later sequences (i.e. Wabiskaw formation) will be controlled by the underlying geological structure of the SMU. In addition, recall that the McMurray formation, the formation residing directly above the SMU, was absent in parts geologic model built from well data. This is supporting evidence for topographic highs (i.e. the ridge feature 'A') of which no deposition of the McMurray formation occurred.

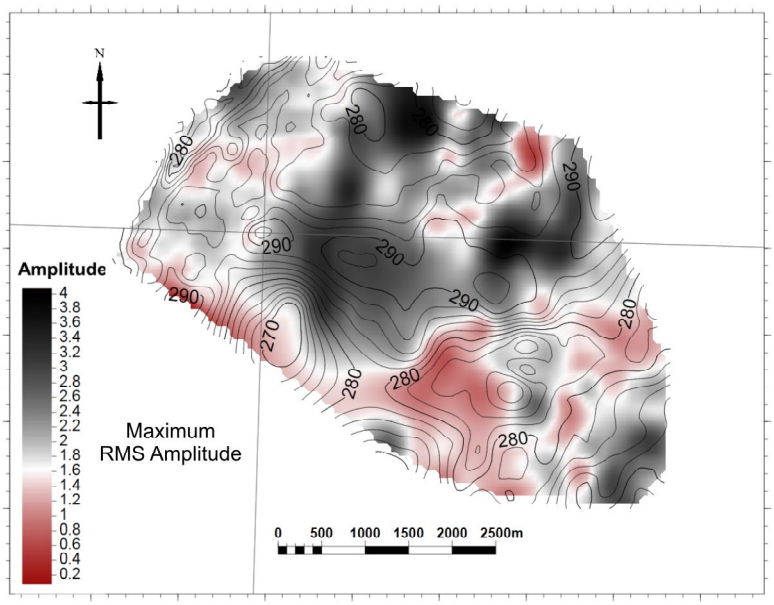

Figure 7.12: Maximum RMS amplitude map of the SMU horizon.

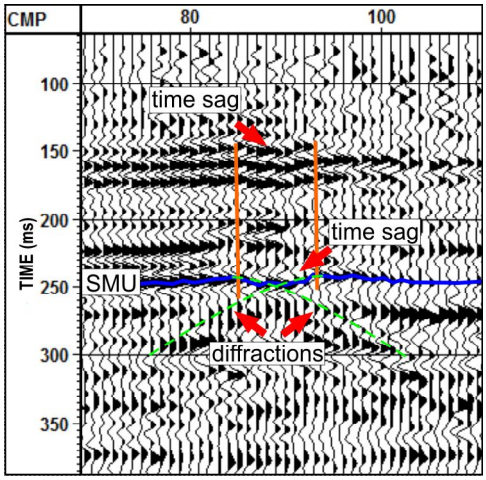

Figure 7.13: Interpretation of a collapsed doline in seismic line B-04. Orange lines indicate possible faulting.

Seismic attributes [*Chopra and Marfurt*, 2007] are often used with modern data sets to distil information into a more readily interpretable form. Concerning the SMU one might expect that amplitudes from strongly karsted zones, such as extensive epikarst, dolines, large fissures and even caves, would reduce the relativity due to scattering effects of the seismic wave. With this in mind, Figure 7.12 shows a low amplitude response that correlates well with the valley tend 'B' highlighted earlier. When analyzing the seismic sections of this area, numerous diffractions were noticed and often associated with minor undulations in the SMU surface. For example at CMP location 87 of seismic line B-04 (Figure 7.13), a small sag in the SMU surface and subsequent diffractions were observed in the unmigrated data. This is similar to what was seen in the chapter 5 for the forward modelling of a karst features < 160 meters. In addition, horizons above this feature showed a similar time sags as well. Thus, this structure was interpreted as a collapsed doline measured ~100 meters in diameter. Features like this were mostly associated to the lower valley with few elsewhere. Doline features seen in the data ranged from 40 to 120 meters in diameter. Dolines below 40 meters may be present but were not resolvable in the seismic data.

As far as porosity is concernd, from chapter 6 we concluded that an increase in porosity should also signify a decrease in amplitude. It may be possible to correlate an amplitude porosity relation in areas outside of heavily

karst areas of features 'B' and 'C'. It is speculated that areas of relatively low amplitude seen in features 'A' and the apparent karst plain could indicate higher porosity. This could be not confirmed due to the lack of data control required for an appropriate proof.

7.4. Discussion of Grosmont

The subcropping Grosmont was interpreted as a mature karst surface containing dolines, a karst valley, a Poljie, a ridge and karst plain. Each these features were observed in the high-resolution seismic data. The valley of feature 'B' trended E-W in the southern section of the local area and was notice to encompass the majority of smaller dissolution features such as dolines. It is possible that this valley was once a Poljie. Water appeared to have collected and percolated through Grosmont within the extent of this stucture that gave rise to dissolution features. It is reasonable that this area also developed cavities and small conduits for the drainage of water at the time of erosion. Feature 'A' denoted a ridge, a topographic high in the SMU. Feature 'C' was a distinct karst valley that was mapped trending NE-SW near the western edge of the local area. Everywhere else was considered Karst plain and showed minimal evidence of dissolution features. The final map depicting the approximate location for these karst features is shown in Figure 7.14.

Karst features of ridge and Poljie at the SMU surface were geologically controlled by previous tectonic active of faulting and folding of Devonian aged formations. However, the metamorphic basement (i.e. PCU surface) did not exhibit the same structure. This implies that Devonian package of rock could have faulted and displaced along the PCU surface.

As more data becomes available in the future, it would be interesting to combine information from seismic attributes (such as amplitude) with log data, core results. The rock-physics model developed back in chapter 6 suggest that it may be possible to characterize porosity and reservoir thickness of the Grosmont from seismic measurements of amplitude. In addition, the heating of bitumen

should also be detectable. There is potential for mapping heat distribution within the reservoir from steam injection by implementing time-lapse seismic surveys.

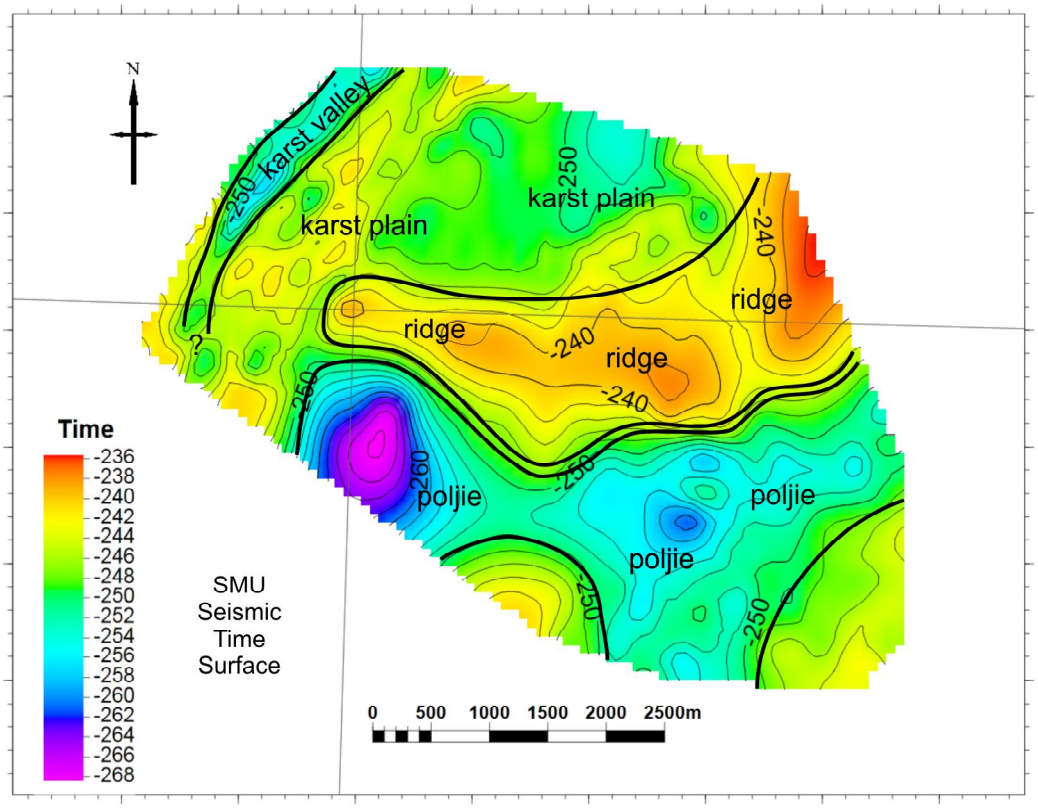

Figure 7.14: Seismic time map of the SMU with interpreted karst features.

One a final note, wells in the area that were drilled into dissolution features such as dolines reported missing stratigraphic units of Grosmont members D and even C [*Hopkins and Jones*, 2009]. Since these units house the bitumen, hydrocarbon prospectors should stay clear of the Poljie and karst valley as depicted in Figure 7.14. Areas of the ridge and karst plain are more likely to have these reservoir units intact.

7.5. Summary

This chapter described the integrated interpretation of the legacy seismic data sets of survey series A, B, C, D and E. Seismic and well observations of the SMU were consistent with mature karst surface model. The large structures of topographic highs and lows of the SMU were shown to be geological controlled

from beneath. As such, dissolution features were prominent in the topographic low and therefore was interpreted as a Poljie. This strongly karsted zone may include rough topograph, extensive epikarst, and even caves. Other such features mapped on the SMU were a karst valley, ridge, and karst plain.

Dolines in the seismic data were characteristic of subtle time sags and amplitude dimming of SMU reflector, and the diffraction of seismic energy. Larger collapsed dolines of ~100 meters in diameter also introduced time sags in the above Mesozoic formations. Doline diameters in the local area ranged from 40 - 120 meters.

The thickness and structure of overlying Mesozoic formations are, due to compaction, geologically controlled by the main topographic highs and lows in the SMU.

Chapter 8 Conclusion

8.1. Conclusion

This thesis was able to define the stratigraphic structure of the Grosmont formation and the spactial distribution of other geological facies and their possible implications on heavy oil recovery. As a result of the analyses of 25 2D seismic lines, 1 small 3D seismic survey, and 117 wells, the following conclusion were drawn.

1) At the location of subcropping Grosmont, the seismic data was able to image a mature karst surface that showed evident dolines, karst valley, ridge, poljie, and karst plain structures. In contrary, the interpolation of well log data to predict these geological structures, let alone reservoir properties, proved problematic.

2) 2-D seismic lines were rather inadequate at imaging small scale, 3D structures such as dolines. It was estimated that dolines could be detected by diffractions and localized dimming and subtle time sags in the SMU reflector for diameters 30 - 160 meters. Observations from the seismic data measured doline diameters to range from 40 - 120 meters. These dolines were largely associated with, but not confined to, the mapped poljie in the local area.

3) A karst valley in the local area was well imaged by the seismic data and measured 237 meters wide. Estimates suggest that karst valleys at the SMU should be resolvable down to about 25 meters.

4) The bitumen saturated Grosmont was shown to have a significant frequency and temperature dispersion on a propagating seismic wave. The use of standard rock mixing architectures of Gassmann and Boit theories cannot accurately

predict the seismic response of the Grosmont reservoir. It is important for future pactioners to consider using more advanced rock-physics modeling methods, such as coherent potential approximation theory, when characterizing the seismic response of the Grosmont formation with log and core information. The strong temperature dispersion, in itself, suggests that heating of the Grosmont reserviour can be mapped by time-lapse seismic surveys.

5) Horizons above and below conform to the large scale (> 1 km) subsurface topography of the SMU. This interesting finding was not expected. Such conformances could indicate that deeper horizons may influence both structure of the SMU and overlying geology. Furthermore, there was no indication of structure control by Precambrian basement such as major faulting events or other such tectonic activity.

6) It appears that there was an overall differentiation of low seismic amplitude response corresponding to poljie. The lower amplitude response of is presumably due to the more highly karsted zones scattering the energy out of the 2D plane defined by the seismic line.

7) The current re-examination and integration of the legacy seismic data sets demonstrated the necessity for geophysical studies to produce this resource. It was noted that dissolution features have the potential to erode the Grosmont reservoir. Bitumen prospectors should be mindful of karst features such as dolines, poljies and karst valleys that could remove the resource entirely. The karst plain is suggested to have these reservoir units intact.

8.2. Future Work

There remains a great deal to learn about the seismic characterization of the Grosmont reservoir and its environs. Future studies could focus on:

1) Modern 3D seismic surveys would greatly improve the mapping of dolines. The 2D seismic surveys of this thesis are limited by no spatial coverage in-between the seismic lines. In addition, higher resolution of dolines is achieved through migration of 3D data than 2D data.

2) Measuring of anisotropy in the seismic data can provide indication of the existing fracture/joint alignment. Recoding a downhole VSP while obtaining a 3D surface seismic set would provide for numerous azimuths and offsets for the detection of anisotropy.

3) The original researchers were already beginning to think about time-lapse seismic as a way to monitor the production of such reservoirs. For this to be properly carried out some knowledge about the behaviour of the saturated rocks under conditions of pressure and temperature is required; laboratory measurements on core would be an asset.

References Cited

Airo, M.-L., and M. Wennerström (2010), Application of regional aeromagnetic data in targeting detailed fracture zones, *Journal of Applied Geophysics*, *71*(2-3), 62-70.

Alkhalifah, T. (2006), Kirchhoff time migration for transversely isotropic media: An application to Trinidad data, *Geophysics*, *71*(1), S29-35.

Barrett, K., and J. Hopkins (2008), Reservoir units within a multi-layered dolostone formation: Grosmont formation, Saleski Area: abstract, in *2008 CSPG Annual Core Conference*, edited, pp. 966-967, Calgary, Alberta, Canada.

Barrett, K. R., and J. Hopkins (2010), Stratiform Carbonate Breccias of the Grosmont Formation, Alberta, paper presented, in *2010 AAPG International Convention and Exhibition*, edited, American Association of Petroleum Geologists, Calgary, Alberta, Canada, September 12-15, 2010.

Barton, P. J. (1986), The relationship between seismic velocity and density in the continental-crust - a useful constraint, *Geophysical Journal of the Royal Astronomical Society*, *87*(1), 195-208.

Bass, J. D. (1995), Elasticity of Minerals, Glasses, and Melts, in *Mineral physics & crystallography: a handbook of physical constants* edited by T. J. Ahrens, pp. 45-63, American Geophysical Union, Washington, D.C.

Batzle, M., R. Hofmann, and D.-H. Han (2006), Heavy oils--seismic properties, *The Leading Edge*, *25*(6), 750-756.

Belyea, H. R. (1956), Grosmont Formation in the Loon Lake Area, *Bulletin of Canadian Petroleum Geology*, *4*(3), 66-69.

Berkhout, A. J. (1979), Steep dip finite-difference migration, *Geophysical Prospecting*, *27*(1), 196-213.

Berkhout, A. J. (1984), *Resolving power of acoustical echo techniques*, 288 pp., Geophysical Press, London.

Berryman, J. G. (1980), Long wavelength propagation in composite elastic media II. Ellipsoidal inclusions, *Journal of the Acoustical Society of America*, *68*(6), 1820-1831.

Best, M., H. Abercrombie, and J. Peirce (1998), Interpreted faulting patterns in northeast Alberta using high resolution aeromagnetic data, *Canadain Journal of Exploration Geophysicists*, *34*(1-2), 49-57.

Blakey, R. (2011), North American Paleogeographic Maps: Late Devonian (360Ma), edited, Colorado Plateau Geosystems, Inc., Flagstaff, Arizona.

Borrero-Gomez, M. (2010), Hondo evaporites within the Grosmont heavy oil carbonate platform, Alberta, Canada, 236 pp, University of Alberta, Edmonton, Alberta, Canada.

Bouzidi, Y., and D. R. Schmitt (2009), Measurement of the speed and attenuation of the Biot slow wave using a large ultrasonic transmitter, *J. Geophys. Res.*, *114*(B8), B08201.

Brook, G. A., and D. C. Ford (1978), The origin of labyrinth and tower karst and the climatic conditions necessary for their development, *Nature*, *275*(12), 493-496.

Buschkuehle, B., F. Hein, and M. Grobe (2007), An Overview of the Geology of the Upper Devonian Grosmont Carbonate Bitumen Deposit, Northern Alberta, Canada, *Natural Resources Research*, *16*(1), 3-15.

Canales, L. L. (1984), Random noise reduction, *SEG Extended Abstracts*, 525-537.

Cao, S., and S. Greenhalgh (1998), 2.5-D modeling of seismic wave propagation; boundary condition, stability criterion, and efficiency, *Geophysics*, *63*(6), 2082-2090.

Carrington, G. (1986a), Geophysical activity in the Buffalo Creek heavy oil area, UNOCAL 817*Rep.*, 1-35 pp, Alberta Oil Sands Technology and Research Authority, Edmonton, Alberta.

Carrington, G. (1986b), Records of seismic surveys conducted at the Buffalo Creek site over a period March 1980 to February 1986, UNOCAL 1051*Rep.*, Alberta Oil Sands Technology and Research Authority, Edmonton, Alberta.

Carrington, G. (1986), Geophysical activity in the Buffalo Creek heavy oil area, UNOCAL 817*Rep.*, Alberta Oil Sands Technology and Research Authority, Edmonton, Alberta.

Cary, P. W., and G. A. Lorentz (1993), 4-component surface-consistent deconvolution, *Geophysics*, *58*(3), 383-392.

CGG (1983), 3-D Seismic Survey - Grosmont, UNOCAL 1052*Rep.*, Alberta Oil Sands Technology and Research Authority, Edmonton, Alberta.

Chopra, S., and K. J. Marfurt (2007), *Seismic Attributes for Prospect Identification and Reservoir Characterization*, 464 pp., Society of Exploration Geophysicists, Tusla, Oklahoma.

Claerbout, J. F. (1985), *Imaging the earth's interior*, Blackwell Scientific Publishing.

Colpaert, A., N. Pickard, J. Mienert, L. B. Henriksen, B. Rafaelsen, and K. Andreassen (2007), 3D seismic analysis of an upper palaeozoic carbonate succession of the Eastern Finnmark Platform area, Norwegian Barents Sea, *Sediment. Geol.*, *197*(1-2), 79-98.

Cotterill, D. K., and W. M. Hamilton (1995), Geology of Devonian limestones in Northeast Alberta*Rep.*, Alberta Geological Survey, Edmonton, Alberta.

Cox, M. (1999), *Static Corrections for Seismic Reflection Surveys*, 531 pp., Society of Exploration Geophysicists, Tusla, Oklahoma.

Cutler, W. G. (1982), Stratigraphy and sedimentology of the Upper Devonian Grosmont Formation, Alberta, Canada, 191 pp, University of Alberta, Edmonton, Alberta, Canada.

Cutler, W. G. (1983), Stratigraphy and sedimentology of the Upper Devonian Grosmont Formation, Northern Alberta, *Bulletin of Canadian Petroleum Geology*, *31*(4), 285-325.

Dai, N., A. Vafidis, and E. R. Kanasewich (1995), Wave propagation in heterogeneous, porous media; a velocity-stress, finite-difference method, *Geophysics*, *60*(2), 327-340.

De Ghetto, G., F. Paone, and M. Villa (1995), Pressure-Volume-Temperature Correlations for Heavy and Extra Heavy Oils: 30316-MS, in *SPE International Heavy Oil Symposium*, edited, p. 16, Society of Petroleum Engineers, Calgary, Alberta, Canada.

DeCelles, P. G., and K. A. Giles (1996), Foreland basin systems, *Basin Research*, *8*(2), 105-123.

Dembicki, E. A. (1994), The Upper Devonian Grosmont Formation: Well log evaluation and regional mapping of a heavy oil carbonate reservoir in northeastern Alberta, 237 pp, University of Alberta, Edmonton, Alberta, Canada.

Docherty, P. (1991), A brief comparison of some Kirchhoff integral formulas for migration and inversion, *Geophysics*, *56*(8), 1164-1169.

Dou, Q., Y. Sun, and C. Sullivan (2009), Seismic detection of paleocave system and its influence on carbonate reservoir compartmentalization, *SEG Technical Program Expanded Abstracts*, *28*(1), 1731-1735.

Duan, Y., J. Tao, L. Zeng, M. Bi, and B. Feng (2010), Using curvature attributes to identify a carbonate paleokarst system in the Ordos Basin, in *72nd EAGE Conference & Exhibition EAGE*, edited, Barcelona, Spain.

Eberli, G. P., G. T. Baechle, F. S. Anselmetti, and M. L. Incze (2003), Factors controlling elastic properties in carbonate sediments and rocks, *The Leading Edge*, *22*(7), 654-660.

Ellis, D., J. Howard, C. Flaum, D. McKeon, J. Scott, O. Serra, and G. Simmons (1988), Mineral logging parameters: nuclear and acoustic, *The Technical Review*, *36*(1), 38-52.

ERCB (2009a), ST98-2009: Alberta's energy reserves 2008 and supply/demand outlook 2009-2018*Rep.*, Energy Resource Conservation Board, Calgary, Alberta.

ERCB (2009b), Table of Formations, Alberta, edited, Energy Resource Conservation Board, Edmonton, Alberta.

ERCB (2010), ST98-2010: Alberta's energy reserves 2009 and supply/demand outlook 2010-2019*Rep.*, Energy Resource Conservation Board, Calgary, Alberta.

Evans, M. W., S. W. Snyder, and A. C. Hine (1994), High-resolution seismic expression of karst evolution within the Upper Floridian aquifer system - Crooked Lake, Polk County, Florida, *Journal of Sedimentary Research Section B-Stratigraphy and Global Studies*, *64*(2), 232-244.

Farzadi, P., and J. Hestharnmer (2007), Diagnosis of the Upper Cretaceous palaeokarst and turbidite systems from the Iranian Persian Gulf using volume-based multiple seismic attribute analysis and pattern recognition, *Petroleum Geoscience*, *13*(3), 227-240.

Field, M. (2002), *A Lexicon of Cave and Karst Terminology with Special Reference to Environmental Karst Hydrology (2002 Edition)*, 221 pp., U.S. Environmental Protection Agency, Office of Research and Development, National Center for Environmental Assessment, Washington Office, Washington, DC.

Ford, D. C., and P. Williams (2007), *Karst Hydrology and Geomorphology*, 578 pp., Wiley, Hoboken, New Jersey.

Gassmann, F. (1951), Elastic waves through a packing of spheres, *Geophysics*, *16*(4), 673-685.

GEDCO (2009), *Vista 9.0: 2D/3D seismic data processing manual*, GEDCO, Calgary, Alberta.

Graves, R. W. (1996), Simulating seismic wave propagation in 3D elastic media using staggered-grid finite differences, *BULLETIN OF THE SEISMOLOGICAL SOCIETY OF AMERICA*, *86*(4), 1091-1106.

Gray, K., J. Russel-Houston, C. Wright, C. Li, and W. Nowry (2011), Seismic characterization of collapse dolines in the Grosmont Formation, Alberta Canada: abstract, in *2011 CSPG CSEG CWLS Joint Convention*, edited, Calgary, Alberta, Canada.

Gray, S. H., J. Etgen, J. Dellinger, and D. Whitmore (2001), Seismic migration problems and solutions, *Geophysics*, *66*(5), 1622-1640.

Gurevich, B., K. Osypov, R. Ciz, and D. Makarynska (2008), Modeling elastic wave velocities and attenuation in rocks saturated with heavy oil, *Geophysics*, *73*(4), E115-122.

Hale, D. (1991), Stable explicit depth extrapolation of seismic wavefields, *Geophysics*, *56*(11), 1770-1777.

Hamilton, W. M., M. Price, and Langenberg (1999), Geological map of Alberta No. 236, edited, Alberta Geological Survey, Alberta Energy and Utilities Board, Edmonton, Alberta.

Hardage, B. (2000), *Vertical seismic profiling principles*, 552 pp., Pergamon, New York, New York.

Hardage, B. A., D. L. Carr, J. L. J. Simmons, R. A. Jons, D. E. Lancaster, R. Y. Elphick, and V. M. Pendleton (1996), 3-D seismic evidence of the effects of

carbonate karst collapse on overlying clastic stratigraphy and reservoir compartmentalization, *Geophysics, 61*(5), 1336-1350.

Harrison, H. D., and D. R. Hiltunen (2003), Characterization of karst terrane via SASW seismic wave method, in *Sinkholes and the Engineering and Environmental Impacts of Karst*, edited by B. F. Beck and P. E. LaMoreaux, pp. 519-528.

Harrison, R. S. (1984), The Bitumen-Bearing Paleozoic Carbonate Trend of Northern Alberta: Section III. Geological Environments and Migration, in *Exploration for Heavy Crude Oil and Natural Bitumen: AAPG Special Volumes 25*, edited, pp. 319-326, American Association of Petroleum Geologists.

Harrison, R. S. (1986), Regional geology and resource characterization of the Upper Devonian Grosmont formation, Northern Alberta, UNOCAL 820*Rep.*, Alberta Oil Sands Technology and Research Authority / Alberta Geological Survey, Edmonton, Alberta.

Haryono, E., and M. Day (2004), Landform differentiation within the Gunung Kidul Kegelkarst, Java, Indonesia, *Journal of Cave and Karst Studies, 66*(2), 62-69.

Helmore, S. (2009), Dealing with the noise --- Improving seismic whitening and seismic inversion workflows using frequency split structurally oriented filters, *SEG Technical Program Expanded Abstracts, 28*(1), 3367-3371.

Hiltunen, D. R., and B. J. Cramer (2008), Application of seismic refraction tomography in karst terrane, *J. Geotech. Geoenviron. Eng., 134*(7), 938-948.

Hiltunen, D. R., N. Hudyma, T. P. Quigley, and C. Samakur (2007), Ground proving three seismic refraction tomography programs, *Transportation Research Record*(2016), 110-120.

Holland, W. G., and H. Zimmerman (2000), The dolomite problem revisted, *International Geology Review, 42*(6), 148-490.

Hope, J., D. W. Eaton, and G. M. Ross (1999), Lithoprobe seismic transect of the Alberta Basin; compilation and overview, *Bulletin of Canadian Petroleum Geology, 47*(4), 331-345.

Hopkins, J., and B. Jones (2009), Reservoir units in the Grosmont Formation: Stratigraphy, Paleotopography and Reservoir Geology of the Grosmont Formation

Twp 80-90 Rge 12-21W4*Rep.*, Alberta Research Council, Carbonate Research Program Report # Geology 0708-1, Edmonton, Alberta.

Hosken, J. W. (1988), Ricker wavelets in their varous guises, *First Break*, *6*(1), 24-33.

Howell, S. (1987), Grosmont Karsting, UNOCAL 647 and 819*Rep.*, Alberta Oil Sands Technology and Research Authority, Edmonton, Alberta.

Hubral, P. (1977), Time migration - some ray theoretical aspects, *Geophysical Prospecting*, *25*(4), 738-745.

Huebscher, H. (1996), Regional controls on the stratigraphic and diagenetic evolution of Woodbend Group carbonates, north-central Alberta, Canada, 248 pp, University of Alberta, Edmonton, Alberta, Canada.

Hunt, D., G. Elvebakk, B. Rafaelsen, J. Pajchel, K. Hogstad, H. Robak, and T. Randen (2003), Palaeokarst Recognition & 3D Distribution – New Insights from the Upper Palaeozoic, Loppa High, Barents Sea, in *65th EAGE Conference & Exhibition*, edited, EAGE, Stavanger, Norway.

Ing, A. (1985), Delineation of the northern extension of the Rimbey-Meadowbrook reef tract, Upper Devonian, Report 1985-02*Rep.*, Alberta Geological Survey, Alberta Research Council, Edmonton, Alberta.

Jacobson, R. S. (1987), An investigation into the fundamental relationships between attenuation, phase dispersion, and frequency using seismic refraction profiles over sedimentary structures, *Geophysics*, *52*(1), 72-87.

Jennings, J. N. (1985), *Karst Geomorphology*, 293 pp., Basil Blackwell Inc., New York, New York.

Jiang, Q., J. Yuan, J. Russel-Houston, B. Thornton, and A. Squires (2009), Evaluation of recovery technologies for the Grosmont carbonate reservoirs: 2009-067, paper presented at Proceedings of the Canadian International Petroleum Conference, Petroleum Society, Calgary, Alberta, Canada, June 16-18, 2009.

Jones, B. (2010), Fracture systems in the Grosmont Formation*Rep.*, Alberta Innovates - Technology Futures, Carbonate Research Program Report # Geology 0910-8a, Edmonton, Alberta.

Leurer, K. C., and J. Dvorkin (2006), Viscoelasticity of precompacted unconsolidated sand with viscous cement, *Geophysics*, *71*(2), T31-40.

Lindsey, J. P. (1989), The Fresnel zone and its interpretive significance, *The Leading Edge*, *8*(10), 33-39.

Machel, H. G. (2005), Investigations of burial diagenesis in carbonate hydrocarbon reservoir rocks, *Geoscience Canada*, *32*(3), 103-128.

Machel, H. G. (2010), The Devonian petroleum system of the Western Canada Sedimentary Basin - with implications for heavy oil reservoir geology, in *Heavy Oils: Reservoir Characterization and Production Monitoring*, edited by M. Batzle, pp. 129-192, Society of Exploration Geophysicists, Tulsa, Oklahoma.

Makarynska, D., B. Gurevich, J. Behura, and M. Batzle (2010), Fluid substitution in rocks saturated with viscoelastic fluids, *Geophysics*, *75*(2), E115-122.

March, D. W., and A. D. Bailey (1983), A review of the two dimensional transform and its use in seismic processing, *First Break*, *1*(1), 9-21.

Marsden, D. (1993), Static corrections---a review, Part II, *The Leading Edge*, *12*(2), 115-120.

Mavko, G., T. Mukerji, and J. Dvorkin (1998), *The rock physics handbook: Tools for seismic analysis in porous media*, 339 pp., Cambridge University Press, London, UK.

Mayne, W. H. (1962), Common reflection point horizontal data stacking techniques, *Geophysics*, *27*(6), 927-938.

McGillivray, J., J. E. Palfreyman, and R. S. Harrison (1987), Carbonate Review Project: Geology/Geophysics Report, UNOCAL 312*Rep.*, Alberta Oil Sands Technology and Research Authority / Alberta Research Council, Edmonton, Alberta.

McNamara, M. E. (2009), *Geology of the Burren region, Co. Clare, Ireland*, 69 pp., Northern Environmental Education Development, The Burren Connect Project, Clare County Council, Ennistymon, Ireland.

Milton, G. W., and J. G. Berryman (1997), On the Effective Viscoelastic Moduli of Two-Phase Media. II. Rigorous Bounds on the Complex Shear Modulus in Three Dimensions, *Proceedings: Mathematical, Physical and Engineering Sciences*, *453*(1964), 1849-1880.

Mossop, G. D., and I. Shetsen (1994), Geological Atlas of the Western Canada Sedimentary Basin, Special Report 4, edited, Canadian Society of Petroleum Geologists and Alberta Research Council, Edmonton, Edmonton, Alberta.

Naghizadeh, M., and M. D. Sacchi (2011), Ground-roll elimination by scale and direction guided curvelet transform, in *73rd EAGE Conference & Exhibition incorporating SPE EUROPEC 2011*, edited, Vienna, Austria.

Nedimovi, M. R., and G. F. West (2003), Crooked-line 2D seismic reflection imaging in crystalline terrains: Part 1, data processing, *Geophysics*, *68*(1), 274-285.

Neep, J. P., M. S. Sams, and M. H. Worthington (1996), Measurement of seismic attenuation from high-resolution crosshole data, *Geophysics*, *61*(4), 1175-1188.

Norris, A. W. (1963), *Devonian stratigraphy of northeastern Alberta and northwestern Saskatchewan, Memoir 313*, 168 pp., Geological Survey of Canada, Ottawa, Ontario.

Omnes, G., and P. Robert (1982), The P-Shooter - a fast seismic source for shallow exploration, *Geophysics*, *47*, 1246-1246.

Pana, D. I., and E. J. Waters (2001), GIS Compilation of Structural Elements in Northern Alberta, Release 1.0, Report 2001-01*Rep.*, Alberta Geological Survey, Edmonton, Alberta.

Pap, A. (1983), Seismic field acquisition on land with buried explosive sources*Rep.*, Amoco Canada Petroleum Company Ltd.

Pap, A. (1983), Source and receiver arrays, *written for* Amoco Canada, edited, FreeUSP.

Ping, L., and H. G. Machel (1995), Pore size and pore throat types in a heterogeneous dolostone reservoir, Devonian Grosmont formation, Western Canada Sedimentary Basin, *AAPG Bulletin*, *79*(11), 1698-1719.

Rafaelsen, B., G. Elvebakk, K. Andreassen, L. Stemmerik, A. Colpaert, and T. J. Samuelsberg (2008), From detached to attached carbonate buildup complexes - 3D seismic data from the upper Palaeozoic, Finnmark Platform, southwestern Barents Sea, *Sediment. Geol.*, *206*(1-4), 17-32.

Rietsch, E. (1980), Estimation of the signal-to-noise ratio of seismic data with an application to stacking, *Geophysical Prospecting*, *28*(4), 531-550.

Ristow, D., and T. Ruehl (1994), Fourier finite-difference migration, *Geophysics*, *59*(12), 1882-1893.

Ronen, J., and J. F. Claerbout (1985), Surface-consistent residual statics estimation by stack-power maximization, *Geophysics*, *50*(12), 2759-2767.

Saenger, E. H., and T. Bohlen (2004), Finite-difference modeling of viscoelastic and anisotropic wave propagation using the rotated staggered grid, *Geophysics*, *69*(2), 583-591.

Sams, M. S., J. P. Neep, M. H. Worthington, and M. S. King (1997), The measurement of velocity dispersion and frequency-dependent intrinsic attenuation in sedimentary rocks, *Geophysics*, *62*(5), 1456-1464.

Schacter, P. (1985), Verical seismic profile union et al Orchid 8-1-88-20W4M processing report, UNOCAL 1053*Rep.*, Alberta Oil Sands Technology and Research Authority, Edmonton, Alberta.

Schmitt, D. R. (1999a), Seismic attributes for monitoring of a shallow heated heavy oil reservoir: A case study, *Geophysics*, *64*(2), 368-377.

Schmitt, D. R. (1999b), Seismic attributes for monitoring of a shallow heated heavy oil reservoir; a case study, *Geophysics*, *64*(2), 368-377.

Schmitt, D. R. (2010), Review of existing gravity, magnetic, and seismic data related to the Grosmont Formation, Alberta*Rep.*, Alberta Innovates - Technology Futures, Carbonate Research Program Report # Geology 0809-7a, Edmonton, Alberta.

Schneider, W. A. (1978), Integral formulation for migration in two and three dimensions, *Geophysics*, *43*(1), 49-76.

Shanks, J. L. (1967), Recursion filters for digital processing, *Geophysics*, *32*(1), 33-&.

Soudet, H. J., P. Sorriaux, and J. P. Rolando (1994), Relationship between fractures and karstification - the oil-bearing paleokarst of Rospo Mare (Italy), *Bull. Cent. Rech. Explor.-Prod. Elf Aquitaine*, *18*(1), 257-297.

Steeples, D. W., R. W. Knapp, and R. D. Miller (1984), Examination of sinkholes by seismic reflection, in *Sinkholes their geology, engineering and environmental impact: First Multidisciplinary Conference on Sinkholes*, edited by B. F. Beck, pp. 217-233, Orlando, Florida.

Steeples, D. W., R. W. Knapp, and C. D. McElwee (1986), Seismic reflection investigations of sinkholes beneath Interstate Highway 70 in Kansas, *Geophysics*, *51*(2), 295-301.

Switzer, S. B., W. G. Holland, D. S. Christie, G. C. Graf, A. S. Hedinger, R. J. McAuley, R. A. Wierzbicki, and J. J. Packard (1994), Chapter 12: Devonian Woodbend - Winterburn Stata of the Western Canada Sedimentary Basin, in *Geological Atlas of the Western Canadian Sedimentary Basin, Special Report 4*, edited by G. D. Mossop and I. Shetsen, Canadian Society of Petroleum Geologists and Alberta Research Council, Edmonton, Alberta.

Taner, M. T. (1997), Seismic data processing flow in areas of shallow carbonates, in *Carbonate Seismology*, edited by I. Palaz and K. J. Marfurt, pp. 223-279, Society of Exploration Geophysicists, Tusla.

Taner, M. T., and K. W. Coburn (1981), Surface consistent estimation of source-and-receiver response functions, *Geophysics*, *46*(4), 412-413.

Tesanovic, P. (1984), Geophysical evaluation of Orchid and McLean heavy oil extraction pilot sites Twp. 87, Rge. 19W4M, UNOCAL 818 - Volume 1*Rep.*, Alberta Oil Sands Technology and Research Authority, Edmonton, Alberta.

Tesanovic, P. (1985), Optimal well location selection from geophysical data, Orchid area, Alberta, UNOCAL 1049,*Rep.*, Alberta Oil Sands Technology and Research Authority, Edmonton, Alberta.

Theriault, F. (1984), Lithofacies, diagenesis and related reservoir properties of the Upper Devonian Grosmont Formation, northern Alberta, 207 pp, University of Calgary, Calgary, Alberta, Canada.

Theriault, F. (1988), Lithofacies, diagenesis and related reservoirproperties of the Upper Devonian Grosmont Formation, Northern Alberta, *Bulletin of Canadian Petroleum Geology*, *36*(1), 52-69.

Theriault, F., and I. Hutcheon (1987), Dolomitization and calcitization of the Devonian Grosmont Formation, northern Alberta, *Journal of Sedimentary Research*, *57*(6), 955-966.

Virieux, J. (1986), P-SV wave propagation in heterogeneous media: Velocity-stress finite-difference method, *Geophysics*, *51*(4), 889-901.

Wagner, P., et al. (2010), Fracture characterization of a giant unconventional carbonate reservoir, paper presented, in *2010 AAPG International Convention and*

Exhibition, edited, American Association of Petroleum Geologists, Calgary, Alberta, Canada, September 12-15, 2010.

Waltham, A. C., and P. G. Fookes (2003), Engineering classification of karst ground conditions, *Quarterly Journal of Engineering Geology and Hydrogeology*, *36*(2), 101-118.

Wang, Z. J., H. Wang, and M. E. Cates (2001), Effective elastic properties of solid clays, *Geophysics*, *66*(2), 428-440.

Wo, E., l. Song, T. Hurst, and N. Sitek (2010), Geological review and bitumen resource appraisal of the Grosmont formation within the Athabasca oil sands area, paper presented, in *2010 AAPG International Convention and Exhibition*, edited, American Association of Petroleum Geologists, Calgary, Alberta, Canada, September 12-15, 2010.

Xu, S., and M. A. Payne (2009), Modeling elastic properties in carbonate rocks, *The Leading Edge*, *28*(1), 66-74.

Yilmaz, O. (2001), *Seismic data analysis: processing, inversion, and interpretation of seismic data*, 1000 pp., Society of Exploration Geophysics, Tusla.

Zhao, Y. (2009), Petrophysical properties of bitumen from the Upper Devonian Grosmont reservoir, Alberta, Canada, 199 pp, University of Alberta, Edmonton, Alberta, Canada.

Zhao, Y., and H. Machel (2009), Determination of the viscosity of Grosmont reservoir bitumen, Alberta, Canada: abstract, in *2009 CSPG CSEG SWLS Joint Convention*, edited, pp. 153-156, Calgary, Alberta, Canada.